



**TIMING OF INCREASING ELECTRON COUNTS FROM  
GEOSYNCHRONOUS ORBIT TO LOW EARTH ORBIT**

THESIS

Kirk M. Olson, Captain, USAF

AFIT/GAP/ENP/05-06

**DEPARTMENT OF THE AIR FORCE  
AIR UNIVERSITY**

**AIR FORCE INSTITUTE OF TECHNOLOGY**

---

**Wright-Patterson Air Force Base, Ohio**

The views expressed in this thesis are those of the author and do not reflect the official policy or position of the United States Air Force, Department of Defense, or the United States Government.

**TIMING OF INCREASING ELECTRON COUNTS FROM  
GEOSYNCHRONOUS ORBIT TO LOW EARTH ORBIT**

**THESIS**

Presented to the Faculty  
Department of Engineering Physics  
Graduate School of Engineering and Management  
Air Force Institute of Technology  
Air University  
Air Education and Training Command  
In Partial Fulfillment of the Requirements for the  
Degree of Master of Science (Applied Physics)

Kirk M. Olson, B.S.

Captain, USAF

January 2005

APPROVED FOR PUBLIC RELEASE; DISTRIBUTION UNLIMITED.

**TIMING OF INCREASING ELECTRON COUNTS FROM  
GEOSYNCHRONOUS ORBIT TO LOW EARTH ORBIT**

Kirk M. Olson, B.S.  
Captain, USAF

Approved:

---

Devin Della-Rose (Chairman) \_\_\_\_\_ date \_\_\_\_\_

---

Donald Brautigam (Member) \_\_\_\_\_ date \_\_\_\_\_

---

Glen P. Perram (Member) \_\_\_\_\_ date \_\_\_\_\_

## Abstract

Under certain conditions, high energy electron fluxes can increase over short periods of time in the outer radiation belt and diffuse to low altitudes. Sudden increases of high energy electron densities at low altitudes can drastically damage unsuspecting low-earth-orbit satellites. The progression of electron flux increases from a geosynchronous orbit to low-earth orbit during an electron event is somewhat unknown. If the beginning of electron flux increases at low-earth-orbits could be anticipated, warnings could be issued to space system operators allowing time to take proper measures to protect and minimize satellite damage extending satellite lifetimes and space mission operations.

The Compact Environment Anomaly Sensors (CEASE) onboard the DSP-21 and TSX-5 satellites collected dosimeter data of electrons  $> 1.2$  MeV and protons  $> 25$  MeV. The orbits of the satellites and the particle detection of CEASE provided an opportunity to sample the high energy electron population fluxes at GEO and LEO during electron events. The high energy electron CEASE data was extracted from DSP-21 and TSX-5 when each satellite crossed an approximate geosynchronous L-Shell range ( $L=6.5-6.7$ ). Onsets of electron events at each orbit were determined from the data. Onset comparison showed the progression of elevated electron fluxes from GEO to LEO to be between one and four days. Further comparison of the electron events to solar wind data suggests that high speed streams are necessary, not sufficient, for an electron event to occur.

## **Acknowledgements**

I would like to thank my thesis advisor, Major Devin Della-Rose, for his efforts and expertise through the effort of this thesis. His endless energy and pursuit for knowledge is a true inspiration to all, especially his students; he has truly taken my learning and education to a higher level. Major Della-Rose is a fine example of what a military professional should be.

I would also like to thank the sponsor for this effort, Donald Brautigam from AFRL/VSXBR, Hanscom AFB, MA. Dr. Brautigam found time during his many busy days to ceaselessly steer this effort. Time was never a consideration for him if help was needed. He is a professional that stands out in the space environment field.

I would like to extend special thanks to Lt Courtney Ofner who read many drafts of my work. Her grammar and English skills have brought me back in touch with writing. She is a can-do officer with a great attitude.

Kirk M. Olson

## Table of Contents

	Page
Abstract .....	iv
Acknowledgements .....	v
List of Figures .....	viii
List of Tables .....	x
<b>I. Introduction .....</b>	<b>1</b>
Chapter Overview .....	1
Introduction.....	1
Impact on Air Force Mission.....	2
Problems and Assumptions.....	3
Research Scope and General Approach.....	3
Expected Results.....	5
 <b>II. Background .....</b>	 <b>6</b>
Chapter Overview .....	6
The Solar Wind.....	6
The Magnetosphere.....	11
L-Shells.....	14
Van Allen Belts.....	16
Particles in a Magnetic Field.....	17
Particle Movement in a Magnetic Field.....	19
Adiabatic Invariants .....	21
DSP-21 Overview/Orbital Characteristics .....	24
TSX-5 Overview/Orbital Characteristics.....	25
CEASE Instrumentation.....	26
 <b>III. Methodology .....</b>	 <b>30</b>
Chapter Overview .....	30
Database Description .....	30
Event Isolation/Determination .....	31
Hemisphere Separation .....	33
Standard Error of the Mean.....	35
Onset Determination .....	37

	Page
Electron Event Progression.....	38
IV. Results and Analysis.....	40
Chapter Overview .....	40
Event Isolation/Selection .....	40
Hemisphere Separation .....	46
GEO Onset Determination.....	47
LEO Onset Determination .....	48
Electron Event Progression.....	48
Electron Events and Solar-Geophysical Parameters Correlation.....	49
V. Summary, Conclusions, and Recommendations.....	51
Summary .....	51
Conclusions.....	51
Recommendations for Future Work.....	53
Appendix A. DSP-21 and TSX-5 CEASE Electron Event Plots Comparison with GOES-10 Proton Plots.....	55
Appendix B. TSX-5 CEASE Data Hemisphere Separation and GEP and LEO Onsets.....	68
Appendix C. Electron Event Progression.....	73
Appendix D. Space Environment Center Weekly Reports.....	74
Appendix E. Two-Month Quiet Period Comparison With SEC Weekly Reports .....	78
Appendix F. Electron Event Comparison to Solar Wind Data .....	81
Bibliography .....	86

## List of Figures

Figure	Page
1. Coronal Holes .....	7
2. High Speed Streams.....	8
3. High Speed Stream Plot.....	9
4. Spiral Angle of IMF.....	10
5. Simple Dipole Magnetic Field.....	12
6. The Magnetosphere.....	14
7. L-Shells .....	15
8. Inner and Outer Van Allen Belts .....	17
9. Lorentz Force .....	19
10. Particle Drift: External Force.....	20
11. DSP-21 Orbit .....	25
12. TSX-5 Orbit .....	26
13. CEASE Instrument.....	27
14. CEASE Dosimeter Location.....	29
15. Basic Concept Event.....	32
16. Irregular Event .....	33
17. TSX-5 Apogee/Perigee Location.....	34
18. LEO Onset Determination Example .....	38
19. Solar Cycle 23.....	41
20. Particle Activity Span .....	41

	Page
21. Electron Event #1.....	43
22. GOES-10 Proton Data for Electron Event #1 .....	44
23. Electron Event #6.....	44
24. GOES-10 Proton Data for Event #6.....	44
25. Basic Criteria of Electron Event .....	45
26. Irregular Electron Event #6.....	45
27. Event #1 Hemisphere Separation.....	47
28. DSP-21 Threshold for Event #1.....	47
29. LEO Onset of Event #1 .....	48
30. Electron Event Progression Timing from GEO to LEO .....	49
31. Electron Event and Solar Wind Comparison .....	50

## **List of Tables**

Table	Page
1. Particle Drifts .....	21
2. Electron Events .....	42

# **TIMING OF INCREASING ELECTRON COUNTS FROM GEOSYNCHRONOUS ORBIT TO LOW EARTH ORBIT**

## **I. Introduction**

### **Chapter Overview**

This chapter outlines the thesis effort by introducing the problem at hand and how it impacts the Air Force mission. It also covers any problems and assumptions expected and applied to this effort. Finally, this chapter explains the method of approach used to reach a final analysis resolution.

### **Introduction**

Until Sputnik launched the world into the Space Age in 1957, the only object orbiting the Earth was the Moon. Since then, numerous objects were sent beyond the reaches of the immediate atmosphere to explore and report. Of those to explore, Explorer I, launched in 1958, carried a Geiger counter to report that the Earth is surrounded by charged particles [Green, 2004]. Later research led to conclude that two regions encompass the Earth, one consisting of electrons and one of protons. These regions, or belts, were named the Van Allen belts after the discoverer [Green, 2004]. The Van Allen belts have been interesting regions since their discovery. Numerous experiments and efforts have occurred to report the behavior of particles in these regions.

Of particular interest is the outer Van Allen belt. It consists mostly of electrons at geosynchronous orbit altitudes [Tascione, 1994]. Many experiments have occurred regarding the modeling of particles in the Van Allen belts and the movement of electrons along given magnetic field lines during non-event periods is fairly understood. Electrons can mirror, or “bounce,” along specific magnetic field lines allowing them to reach

geosynchronous orbits (GEO) and low-earth-orbit (LEO) altitudes. A typical bounce timescale is on the order of seconds. However, dramatic increases of high energy electron fluxes, or electron events, observed at geosynchronous L-shells are not observed at low-earth-orbit altitudes at the same L-shells within the bounce timescale. It suggests that the elapsed time between an electron event onset at GEO and LEO is much greater than the typical bounce period or another mechanism is in place.

Williams et al [1968] described the use of “simultaneous observations from several locations within the magnetosphere” to obtain models of particle movement in the event of a geomagnetic storm. Applying this method to electron events may lead to the time separation of energetic electrons arriving at LEO from GEO. The progression of an electron event could be estimated by determining the elapsed time between the beginning of a dramatic electron flux increase at GEO and the onset of the same event at LEO. Such information could better inform space operators of the mechanics of the Earth’s magnetosphere and prepare them for the hazardous effects on DoD systems.

### **Impact on Air Force Mission**

These dramatic electron flux increases have adverse effects on satellites. Dielectric charge, radiation dose rate, and single event effects have been known to damage satellite systems and degrade performance [Dichter, 1998]. The effects of high energy electrons on satellites degrade their performance causing the loss of data, communication, and surveillance, all of which are crucial not only for DoD missions but for the Air Force as well [Dichter, 1998]. It is critical to protect these space assets for continued mission support in the short and long term. Therefore, modeling and

forecasting the progression of high energetic particles from GEO to LEO are necessary to protect space-borne assets and missions.

### **Problems and Assumptions**

A geosynchronous satellite may cross different L-shells from the sunward side and the anti-sunward side even though the satellite's altitude remains constant. This is mainly due to the offset of the Earth's rotation axis and magnetic axis and the asymmetry of the Earth's magnetosphere. In order to simplify the problem, it is assumed that a geosynchronous satellite will be located within the L-shell range of 6.5-6.7 throughout its geosynchronous orbit.

There are three specific uncertainties that need to be addressed: spatial, temporal and dynamical. If the uncertainty in location of the satellites is much larger than the uncertainty of the dynamical electron flux levels, it may be impossible to distinguish the difference between a rise in electron count due to location and a rise in electron count due a certain solar event. In the same respect, if the temporal uncertainty is much larger than the solar dynamical uncertainty, it may be difficult to distinguish the changes in electron counts due to changes in time and the dynamical flux level changes due to an electron event. Depending on the spatial and temporal uncertainty levels, it may be impossible to determine the overall progression time of an electron event from GEO to LEO.

### **Research Scope and General Approach**

The goal of this effort is to determine the progression time of high energetic electron fluxes from geosynchronous orbit heights to low-earth orbit altitudes. Determining the time difference between a dramatic increase of high energy electrons at

GEO and LEO may give a better understanding of particle movement in the magnetosphere at these heights during electron events.

Only a few satellites carry equipment designed to measure the particle effects of the space environment, but the Air Force Research Laboratory, Space Vehicles Directorate, Hanscom AFB, MA has developed a small particle detector able to “piggy-back” on almost any satellite. The Compact Environment Anomaly Sensor (CEASE) is a small, light-weight, low power instrument that gives any satellite the capability to assess and establish the high-energy particle environment effects on the spacecraft in question [Dichter, 1998.]. CEASE is designed to “monitor the elements of the space environment known to produce harmful effects on space systems and to provide real-time alerts to the host spacecraft” [Dichter, 1998]. By reporting real-time space environment and radiation data to the host spacecraft, causes of spacecraft performance degradation can be determined.

The CEASE equipment was placed on two satellites: DSP-21 and TSX-5. DSP-21 is located in a geosynchronous orbit. A sensor in this orbit provides “the necessary long-term continuous database for studying solar cycle variations of the outermost boundary of the outer belt” [Brautigam, 2001]. The TSX-5 satellite has a high inclination, low-earth orbit that crosses many L-shells. Location of the satellites in the magnetosphere is a very important characteristic. DSP-21 remains at a geosynchronous L-shell range of 6.5-6.7. The TSX-5 satellite crosses many L-shells including this L-shell range. A GEO to LEO connection can be established along the L-shell range common to both satellite orbits and where electron diffusion is likely: 6.5-6.7. Therefore, CEASE

electron flux data will be extracted from DSP-21 (GEO) and TSX-5 (LEO) when each satellite crosses the L-shell range of 6.5-6.7.

Observations of electron fluxes at each orbit will determine the onset of an electron event at GEO and LEO. From this, an elapsed time progression of the event from GEO to LEO will be determined. The time periods of electron events may be compared to online sources for possible event causes and common characteristics among the electron events.

### **Expected Results**

The main focus is to determine a progression time of electron events from GEO to LEO. This progression time does not follow the adiabatic invariant time of mirroring, but any time determining the progression of an electron event will bring more understanding to the instabilities and events of the electron belt [Williams et al, 1968]. While determining the time separation, it may possible to determine the cause of an electron event progression beginning at a geosynchronous orbit.

## II. Background

### Chapter Overview

This chapter starts with background information regarding the source of energetic particles. It then progresses to explain the characteristics and regions of the Earth's magnetosphere. Next, charged particle movement in a magnetic field is described followed by a description of the adiabatic invariants. The orbital characteristics of each satellite used in this effort are then characterized. Finally, the particle detection sensor carried onboard each satellite is described.

### The Solar Wind

The solar wind is comprised of constant streams of charged particles generated by the Sun. Electron and proton streams are emitted radially from the star with an average velocity of 400 kilometers per second but such velocities can significantly increase depending on the solar activity [Tascione, 1994]. Particles can also escape the Sun via several means: coronal holes, coronal mass ejections, and solar flares.

Coronal holes are low density regions in the upper atmosphere of the Sun. They develop between regions of closed magnetic field lines which have higher concentrations of particles [Tascione, 1994]. As Figure 1 shows, coronal holes originate from open magnetic field lines that extend into interplanetary space. Coronal holes can lead to faster moving solar streams of particles called high speed streams. These high speed streams move at speeds much greater than the ambient solar wind. “Typically, coronal holes occupy about 20% of the solar surface with maximum occurrence during solar minimum” [Tascione, 1994]. Also at solar minimum, coronal holes last much longer and can be present for several solar rotations.

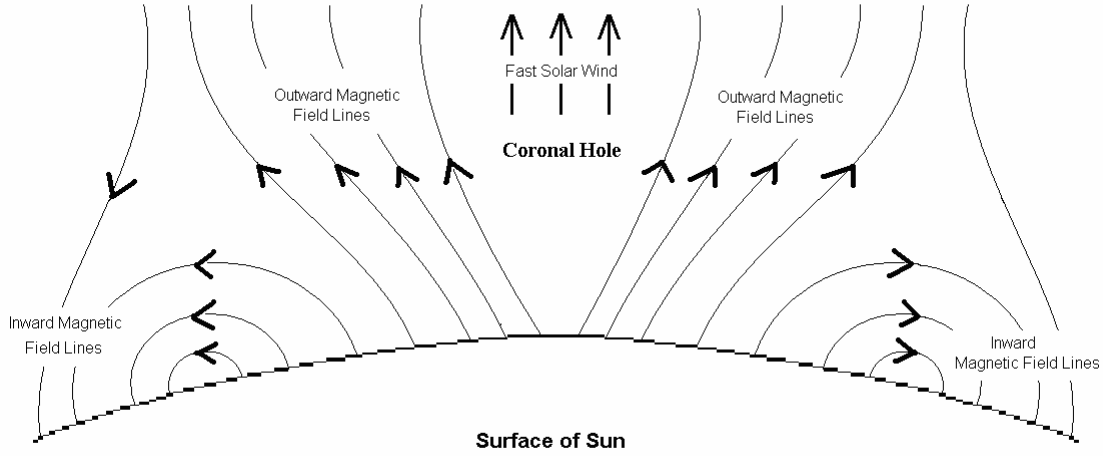


**Figure 1. Coronal holes develop from open field lines on the Sun. These regions lead to high speed solar wind streams [Tascione, 1994].**

“The ‘frozen-in’ conditions of the interplanetary plasma prevent the interpenetration of different streams, so that an interface boundary must form to separate fast streams from the ambient solar wind plasma” [Tascione, 1994]. When a high speed solar stream rams into the slower solar wind, an interaction region can form at the leading edge of the fast stream (Figure 2) [Tascione, 1994; Heber, 1999].

One of the important consequences of this restricted motion is that the density, pressure and magnetic field will build up in front of the high speed solar wind stream and a compressed region will be created in the front of the high speed solar wind stream and a compressed region will be created in the forward direction. The same argument indicates that a rarefied region will be created behind the high speed solar wind because the fast stream is running away from the slower solar wind. [Parks, 2004]

“If the structure is stable for several (solar) rotations (the) interaction region is repeatedly observed in space and therefore called a Co-rotating Interaction Region” [Heber, 1999].

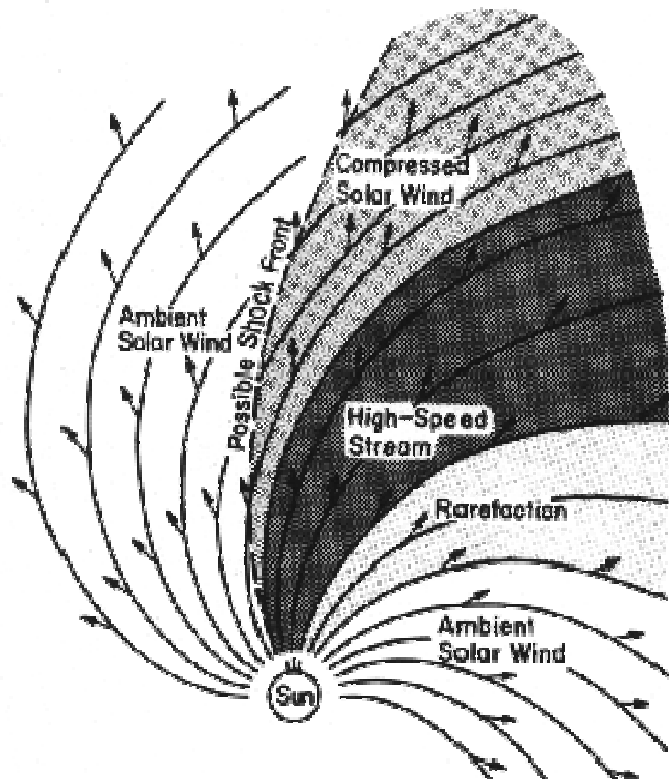


**Figure 2.** High speed solar wind streams have distinct characteristics: a compressed leading edge where the faster stream “catches-up” to the slower ambient solar wind, an increase in solar wind velocity, and a rarefaction region where particle speeds return to ambient solar wind speeds [Tascione, 1997; Cairns, 1999].

High speed streams have three characteristics (Figure 3): rise in density to unusually high values near the leading edge of the stream (A), steep rise in flow speed from pre-stream levels (B) followed by a gradual decrease in speed (C) [Tascione, 1994].

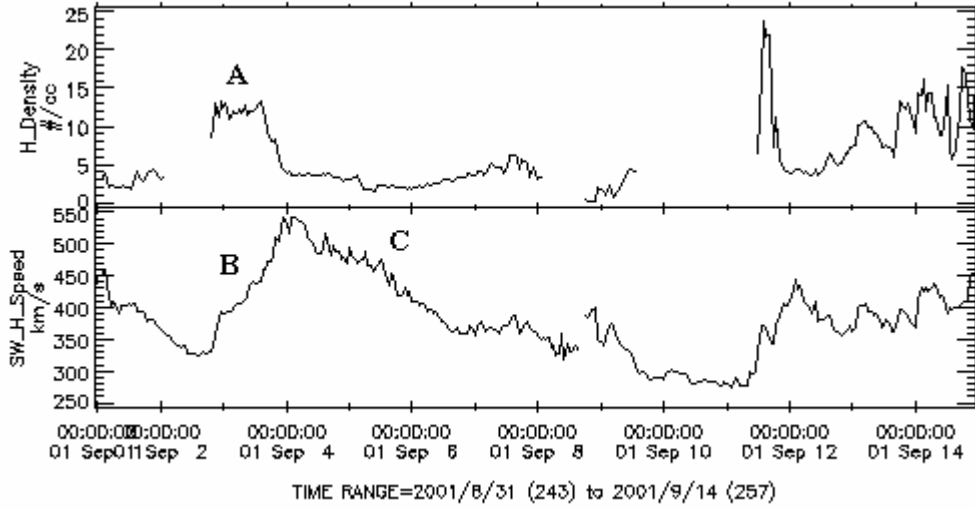


**Figure 3. Density and speed plots of a high speed stream. The leading edge is evident by the sharp increase in particle density (A) and the increase in particle speed (B) an the trailing edge is shown by the decrease in particle speed to normal solar wind speeds of approximately 350 km/sec [Tascione, 1997; McComas, 2005].**

Particles can also escape the Sun through solar flares. Flares are the result of twisted and kinked magnetic field lines in the Sun's upper atmosphere. These events are “highly concentrated explosive release(s) of energy within the solar atmosphere which appears as a sudden, short-lived brightening of a localized area in the chromosphere” [Tascione, 1994]. Solar proton flares eject highly energetic protons; these particles reach the Earth in approximately 30 to 90 minutes which corresponds to relativistic speeds between 30,000 km per second and 80,000 km per second [Tascione, 1994].

Another method for particles to escape the Sun is coronal mass ejections. This particle escape method develops from long eruptions of filaments and flares which can last approximately six hours or longer [Tascione, 1994]. Particles developing from a coronal mass ejection average a speed of 400 kilometers per second but can reach a maximum speed of nearly 1800 kilometers per second [Tascione, 1994]. The particles associated with such an event are high energetic protons.

As the Sun rotates, it releases charged particles in the methods described above. Progression of the solar wind can be observed if viewed from above the Sun; from this prospective the Sun rotates counter-clockwise (Figure 4). The first panel shows the initiation of a parcel of the solar wind (A) which moves away from the Sun at a constant velocity at an initial time ( $t = 0$ ). The next panel ( $t = \Delta t$ ) shows the initial emission (A) at a greater distance and a new emission (B) at the surface. The third panel depicts another emission (C) and the progression of (A) and (B). This continues for several more time intervals as shown. As each parcel is emitted, the Sun's magnetic field connects each parcel forming a spiral similar to the Archimedes spiral [Tascione, 1994]. As the distance from the Sun increases, the angle formed by a surface parallel to the surface of the Sun and the interplanetary magnetic field (IMF) decreases.

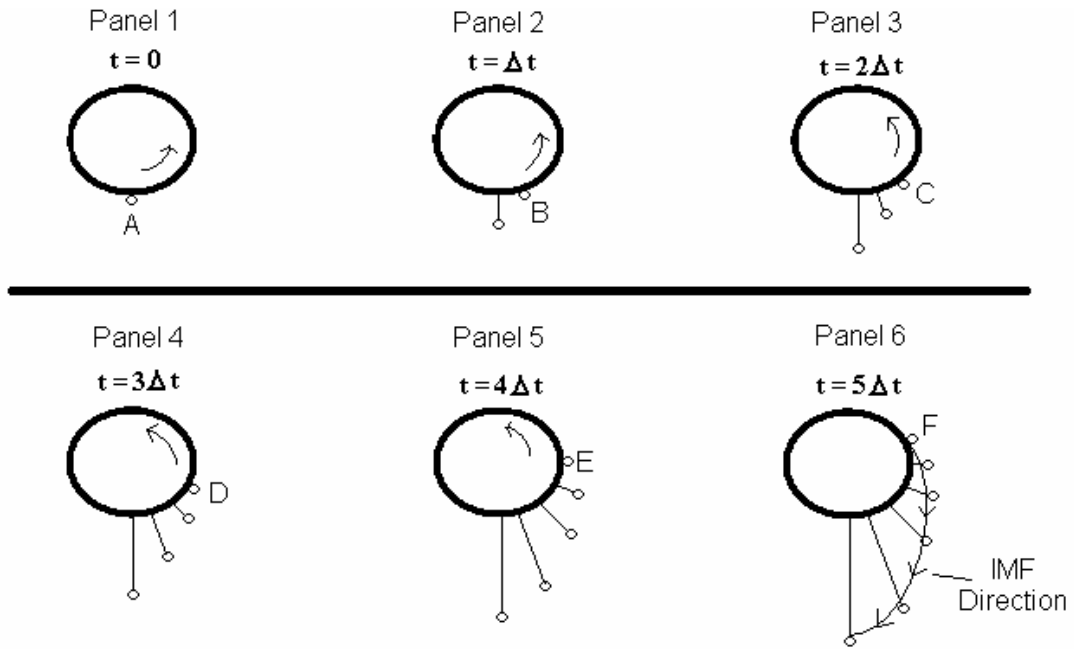


**Figure 4. The Sun radiates particles radially from the same location at a given time interval. As the Sun rotates, the magnetic field line associated with the particles develops an angle equating to the speed of the particles and distance from the Sun [Tascione, 1997].**

While disturbances, such as high speed solar streams, can perturb the spiral angle by increasing/decreasing the velocity of the solar wind, an approximation of the spiral angle can be determined via Equation 1 [Tascione, 1994]. The spiral angle ( $\psi$ ) is defined as the angle between the direct line from the Sun to the Earth and the vector where the IMF encounters the Earth's magnetosphere.

$$\tan(\psi) = r\omega \div v \quad (1)$$

$\psi$  = spiral angle

$r$  = distance from the Sun

$\omega$  = rotation rate of the Sun

$v$  = velocity of solar wind particles

## The Magnetosphere

The Earth is surrounded by a magnetic field similar to one generated from a common bar magnet only much stronger and larger. The region where the Earth's magnetic field is dominant is called the magnetosphere [Shunk, 2000]. The interaction of the solar wind and the Earth's magnetosphere creates a very complex system that includes strong currents, particle precipitation, and the Northern Lights.

The magnetosphere contains magnetic field lines that originate near the geographic South Pole and terminate near the geographic North Pole. Given a simple dipole, the magnetic field strength can be determined at a specific location; Equation 2 and Figure 5 refer to the magnetic field strength of a dipole field if given the angle from the magnetic equator and the distance from the center of the dipole to the desired location on the magnetic field line [Parks, 2004].

$$B = \frac{\mu M}{4\pi r^3} [3\sin^2(\lambda) + 1]^{\frac{1}{2}} \quad (2)$$

$$\begin{aligned}
 B &= \text{magnetic field strength} \\
 \mu &= \text{permiability of free space} \\
 M &= \text{dipole moment of Earth} \\
 r &= \text{distance from center of Earth to local point} \\
 \lambda &= \text{latitude (angle from magnetic equator)} \\
 B_0 &= B(\lambda = 0)
 \end{aligned}$$

Commonly used is the ratio of the local magnetic field strength ( $B$ ) and the equatorial field strength ( $B_0$ ) of the same magnetic field line [D. Brautigam, private conversation, 2004]. This  $B/B_0$  ratio simply highlights a location along a given magnetic field line. The higher the ratio, the closer the location is to a magnetic pole; if the ratio equals one (1), the location is on the magnetic equator.

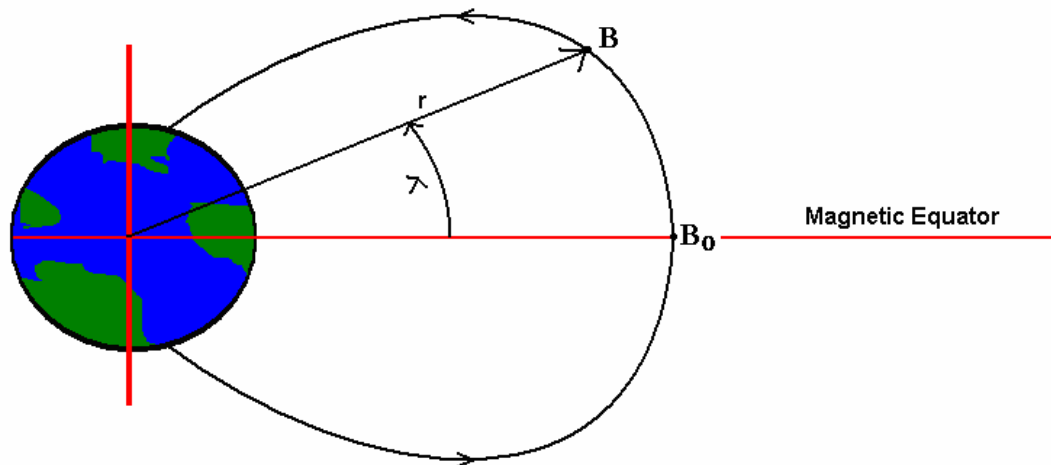


**Figure 5.** Given a simple dipole magnetic field of the Earth, the strength of the magnetic field line at a specific location ( $B$ ) can be determined depending on the distance from the center of the Earth to a point on the magnetic field line ( $r$ ) and the angle ( $\lambda$ ) between the magnetic equator and radial vector.  $B_0$  represents the strength of the magnetic field line at the magnetic field line and magnetic equator intersection [altered from Parks, 2004].

Due to the solar wind, however, the Earth's magnetic field is not a simple dipole; the sunward side and the anti-sunward side of the magnetosphere are not symmetrical. As the

solar wind travels toward the Earth, it encounters the Earth's magnetic field. Before the particles of the solar wind reach the magnetic field of the Earth, its speed decreases from supersonic to subsonic speed; the point of this decrease is called the bow shock [Stern, 2001]. The next boundary is the magnetosheath which is comprised of heated solar wind and plasma [Tascione, 1994]. This layer is followed by the magnetopause and is defined as the boundary where the outward force of the compressed geomagnetic field is balanced by the dynamic pressure of the solar wind [Tascione, 1994]. Therefore, the sunward side of the Earth's magnetosphere is compressed and the anti-sunward side (containing the magnetotail) is elongated. The magnetotail forms as a result of the magnetized solar wind interacting with the Earth's magnetic field [Parks, 2004]. As Figure 6 shows, the magnetosphere extends to about 10 Earth radii on the sunward side while the magnetotail extends beyond 200 Earth radii [Mazur, 2003]. Size of the bow shock and the magnetotail length depend on the solar wind strength and solar activity; the stronger the solar wind, the more the sun-ward side of the magnetosphere compresses and the magnetotail lengthens.

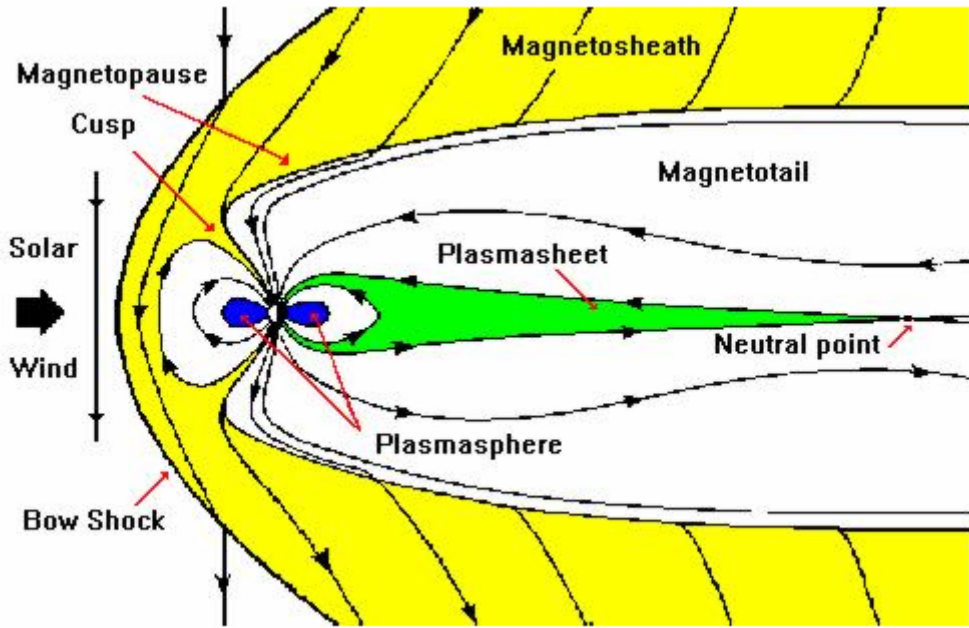


**Figure 6. The Earth's magnetic field interacts with the solar wind and IMF. The sun-ward side is compressed and the anti-sunward side contains the magnetotail which extends for many Earth radii [Cosmic and Heliospheric Learning Center, 2004].**

There exists a region between the leading edge of the bow shock and the magnetotail that allows plasma to reach the Earth's atmosphere. The polar cusps are narrow regions near the magnetic poles where magnetic field lines reach out into interplanetary space [Parks, 2004]. The sizes of the cusps can vary depending upon the strength and direction of the Sun's magnetic field. Particles can enter the Earth's atmosphere directly via the magnetic field lines near the extreme high latitudes.

### **L-Shells**

As shown above, the Earth's magnetosphere is comprised of many magnetic field lines. These magnetic field lines originate near the magnetic North Pole, extend to the equator, and terminate near the magnetic South Pole. The Earth's magnetic field lines can be grouped to represent surfaces; these surfaces are commonly referred to as "L-

shells.” A particular L-shell is numbered in accordance with the intersection of a magnetic field line and the magnetic equator at a certain distance (in Earth-radii or “Re”) from the center of the Earth. The numbered L-shell is the entire magnetic field line that crosses the magnetic equator and extends to the magnetic poles. For example, the magnetic field line that crosses the magnetic equator at a distance of 5 Re from the center of the Earth is given a designation of L-shell 5. Figure 7 shows the approximate location of L-shells and the placement of the magnetic field relative to the Earth’s rotation axis. Configuration of L-shells depends on several factors such as strength of the interplanetary magnetic field and strength of the solar wind [Parks, 2004].

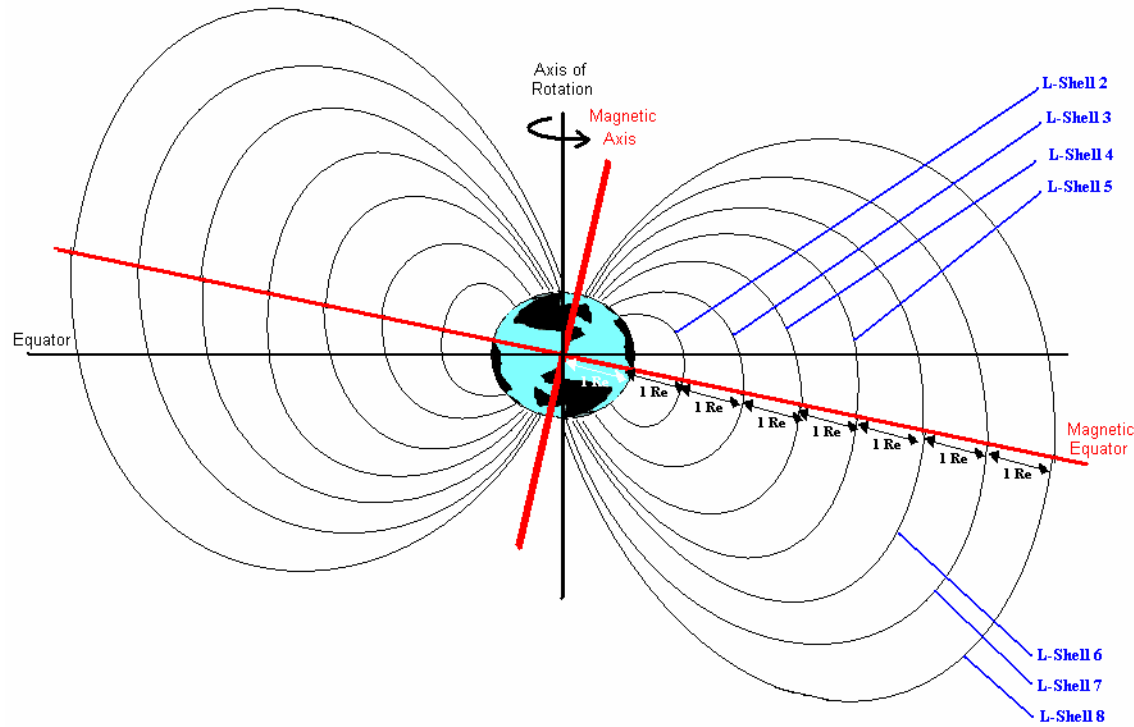


**Figure 7. L-Shells are numbered according to the distance of the magnetic field line and magnetic equator intersection from the center of the Earth in Earth radii (Re).**

While an exact location can be determined by geographical latitude and longitude, location in reference to the magnetic field can also be determined. As described above, the strength of the magnetic field along a magnetic field line can be determined as well as the L-shell. The L-shell gives one dimension while the  $B/B_o$  value gives another. With the two combined, it is possible to locate points in the Earth's inner magnetosphere. However, this "coordinate system" is best used as a 2-D reference, since the same L-shell and  $B/B_o$  combination represents many points in a 3-D reference frame if azimuthal symmetry is assumed.

### **Van Allen Belts**

In the magnetosphere, there are two important regions, or "belts," that contain charged particles: the outer Van Allen belt and the inner Van Allen belt. Each Van Allen belt is an area in the Earth's magnetosphere that has a high concentration of charged particles formed by the solar wind or planetary ionosphere [Parks, 2004]. The inner Van Allen belt consists mostly of very energetic protons (greater than 10 MeV), which originate from the Earth's upper atmosphere [Hultqvist, 1999]. This region is usually found to be at an altitude of 1 to 3 Earth radii and is more stable than the outer belt during geomagnetic storms [Fitzpatrick, 1998].

The outer Van Allen belt is comprised mostly of electrons with energies ranging from 400keV to above 15 MeV [Li, 2000]. This belt is more dependent on changes in the magnetosphere and is, therefore, less understood than the inner Van Allen belt. Electrons in the upper belt originate primarily outside the magnetosphere but ionospheric particles can be accelerated into the trapping regions of the upper belt [Hultqvist, 1999; Tascione, 1994]. The magnetotail can also inject high densities of electrons during geomagnetic

storms [Tascione, 1994]. “In quiet magnetic periods, electron diffusion is an important electron source mechanism,” and the loss of electrons can occur via collisions with neutrals in the atmosphere [Tascione, 1994]. Figure 8 shows the location of the inner and outer Van Allen belts.

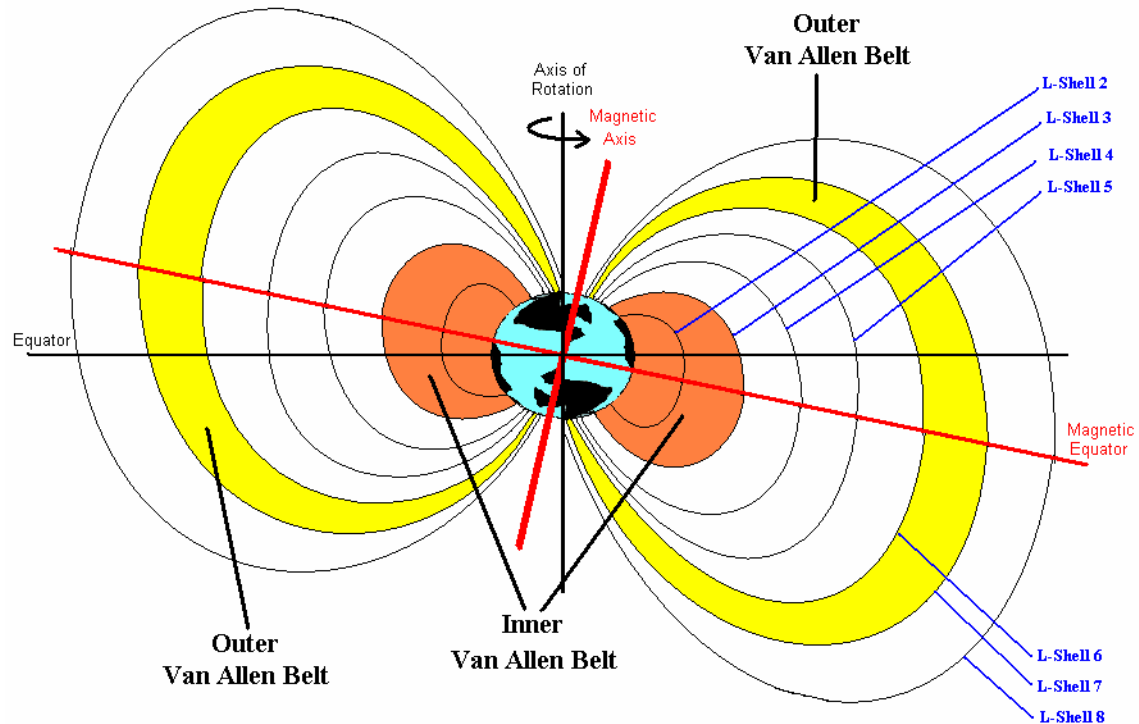


**Figure 8.** The inner Van Allen belt is mostly comprised of protons and is located between L-shells 1 and 3. The outer Van Allen belt is located between L-shells 6 and 7 and consists mostly of electrons [Amherst Astronomy Association, 2004].

### Particles in a Magnetic Field

Charged particles in the Earth's magnetosphere can undergo different motions. One of those motions is gyration which can be described via the Lorentz Force equation:

$$\vec{F}_L = q(\vec{E} + \vec{V} \times \vec{B}) \quad (3)$$

$\vec{F}_L$  = Lorentz Force

$q$  = particle charge

$\vec{E}$  = electric field

$\vec{V}$  = velocity of the particle

$\vec{B}$  = magnetic field

If it is assumed that an electric field does not exist, then the Lorentz force is simply the charge of the particle multiplied by the cross product of the velocity and magnetic field vectors [Tascione, 1994]. The resultant vector is perpendicular to both the velocity and magnetic field vectors. Figure 9 shows a proton initially moving in the z-direction when a uniform magnetic field in the y-direction is suddenly applied. The proton's travel-path will no longer be in a straight line but rather in a curved trajectory of constant radius ( $r_c$ ) due to the perpendicular Lorentz force [Tascione, 1994]. The particle will continue this circular motion at the same speed unless the magnetic field changes or is acted upon by another force. Protons will move in a clockwise motion as shown. Since electrons have a negative charge, they will move in a counter-clockwise motion. The curvature radius of the path, or gyro-radius, can be derived from the Lorentz force and centripetal force equations (Equation 4) [Tascione, 2004]. From this, the gyro frequency can be determined (Equation 5) [Tascione, 2004].

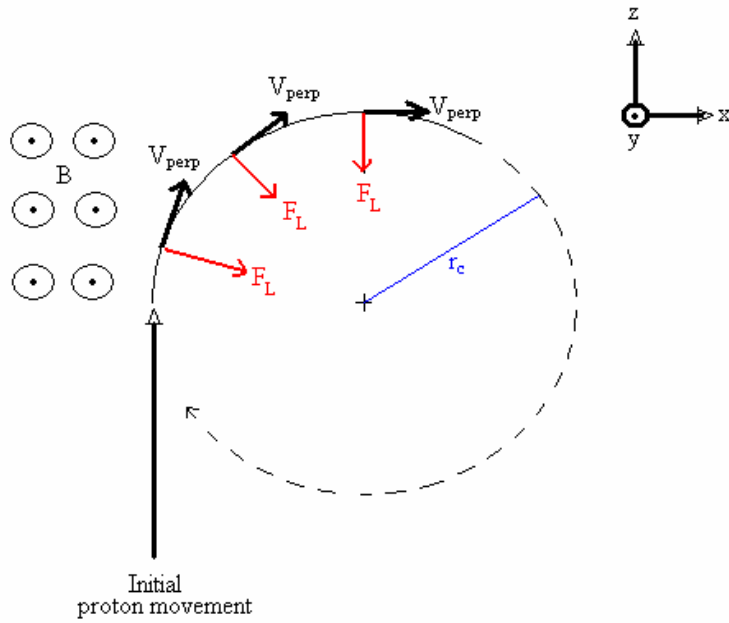


**Figure 9. Depending on the charge and velocity of the particle, the resultant motion of the particle can be determined via the Lorentz Force[Tascione, 1994].**

$$r_c = \frac{mV_{perp}}{qB} \quad (4)$$

$$v_c = \frac{V_{perp}}{2\pi r_c} = \frac{qB}{2\pi m} \quad (5)$$

$r_c$  = gyroradius

$V_{perp}$  = magnitude of particle velocity

$B$  = magnitude of magnetic field

$v_c$  = gyrofrequency

$m$  = particle mass

## Particle Movement in a Magnetic Field

When a moving particle is subjected to an external force in a uniform magnetic field, perpendicular drifts occur. Figure 10 shows the overall motion of a proton when exposed to such a situation. As the proton experiences the magnetic field, it begins its

curved path much like the example in the Lorentz Force section. However, in this case, a force is decreasing the proton's speed as it turns toward the negative z-direction. Therefore, the radius of the curved path decreases (Equation 4). As the proton moves toward the positive z-direction, its radius increases due to the speed increase from the external force. Depending on the external force applied, protons and electrons may move in the same or different drift direction. Table 1 below shows the different particle drifts and equations in a uniform magnetic field (Equations 6, 7, and 8). Equations 9 and 10 represent charged particle movements in a non-uniform or curved magnetic field.

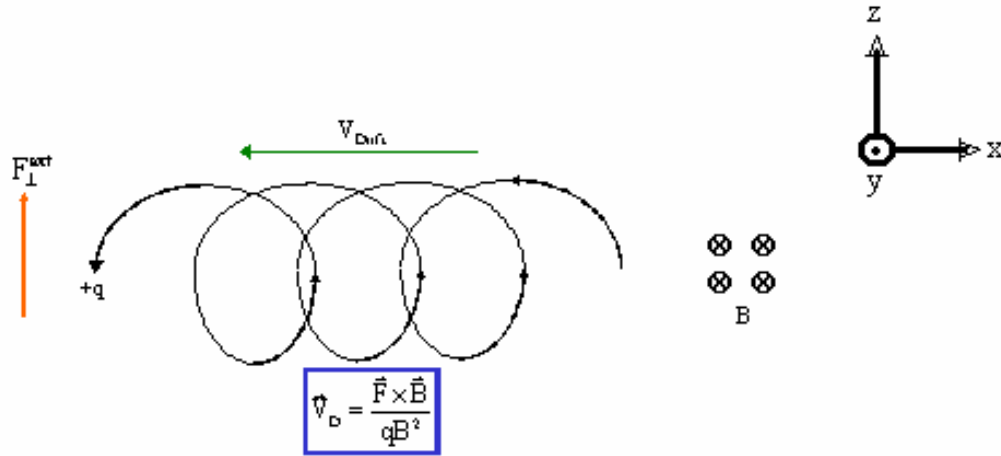


**Figure 10.** Application of an external force to a charged particle in a uniform magnetic field gives a drift motion to the particle. The direction of the drift is dependent on the particle's charge. This example shows the particle drift of a proton in the negative x-direction; under similar criteria, an electron will drift in the positive x-direction [Tascione, 1994].

**Table 1. Particle drift equations in the environment of a uniformed and non-uniformed magnetic field [Tascione, 1994].**

<b>External Force</b> <b>(Equation 6)</b>	$\vec{V}_D = \frac{\vec{F} \times \vec{B}}{qB^2}$
<b>Electric Field</b> <b>(Equation 7)</b>	$\vec{V}_e = \frac{\vec{E} \times \vec{B}}{B^2}$
<b>Gravitational Force</b> <b>(Equation 8)</b>	$\vec{V}_g = \frac{m\vec{g} \times \vec{B}}{qB^2}$
<b>Gradient B</b> <b>(Equation 9)</b>	$\vec{V}_B = \left( \frac{mV_{perp}^2}{2qB^3} \right) \cdot \vec{B} \times \vec{\nabla}B$
<b>Curvature B</b> <b>(Equation 10)</b>	$\vec{V}_c = \frac{m\vec{V}_{parallel}^2}{qR^2 B^2} \cdot \vec{R} \times \vec{B}$

### Adiabatic Invariants

Adiabatic invariants describe the movement of charged particles in a magnetic field. Three adiabatic invariants correspond to three motions: gyration, bounce, and drift [Li, 2000]. The first adiabatic invariant, also called the magnetic moment invariant, describes the gyro-motion of a charged particle in a magnetic field. Magnetic flux is defined as the number of magnetic field lines within an area and can be mathematically represented by Equation 11 [Tascione, 1994]. If the magnetic field vector is constant within the area defined by the gyro-radius, then the magnetic flux is the strength of the magnetic field multiplied by the area of the gyro-orbit [Tascione, 1994].

$$\Theta = B \cdot \pi r_c \quad (11)$$

If the magnetic flux changes on a timescale greater than the gyro-period, then Faraday's Law predicts the particle's total kinetic energy remains constant (Equations 12 and 13) [Tascione, 1994]. ( $V_{\text{perp}}$ ) can be represented by  $V \cdot \sin(\alpha)$  where  $(\alpha)$  is the angle between the velocity vector and the magnetic field vector, also called the pitch angle [Tascione, 1994].

$$\mu \equiv \frac{1}{2} m V^2 \left( \frac{\sin^2(\alpha)}{B} \right) = \text{constant} \quad (12)$$

$$\frac{m V_{\text{perp}}^2}{2} = \text{constant} \quad (13)$$

$$\left( \frac{\sin^2(\alpha)}{B} \right) = \text{constant} \quad (14)$$

If  $(\mu)$  is constant and the total kinetic energy is conserved (Equation 13) and Equation 14 is also a constant, then if  $(\alpha)$  increases, the magnetic field strength  $(B)$  must also increase. As can be seen in Equation 12, if the magnetic field strength increases,  $V_{\text{perp}}$  and  $(\alpha)$  must increase [Tascione, 1994]. The pitch angle will increase if the particle spirals toward a converging magnetic field (thus increasing  $B$ ) until a pitch angle of 90 degrees is reached. There will be a location along the magnetic field line where the particle's gyro-radius reaches a minimum, kinetic energy remains unchanged, and the velocity parallel to the magnetic field equals zero due to the Lorentz force acting in the direction of the diverging magnetic field. This point is known as the "mirror point" [Hultqvist, 1999]. This adiabatic invariant can be violated if the number of magnetic field lines changes drastically within the timescale of a gyro-period or in the length of a

gyro-radius. Typical gyro-periods are on the order of milliseconds for protons and microseconds for electron.

The second adiabatic, or longitudinal, invariant refers to the mirror, or “bounce” motion of a charged particle in the magnetosphere. Specifically, it refers particle’s velocity parallel to the magnetic field ( $v_{\parallel}$ ) (Equation 15) [Parks, 2004]. This integral is formed by the closed path of a particle between mirror points located in opposite hemispheres. The integral holds a constant value if “the magnetic field changes only on a time scale that is long compared to the bounce period;” typical bounce periods are on the order of 10 seconds [Hultqvist, 1999]. The mirror point is proportional to the momentum of the particle (Equation 16) [Hultqvist, 1999].

$$\oint \mathbf{v} \cdot d\mathbf{s} = \text{constant} \quad (15)$$

$$B_m = \frac{(mv)^2}{2\mu m} \quad (16)$$

If the pitch angle of a particle was considered to be near 90 degrees, the particle will gyrate around a given magnetic field line and bounce between mirror points near the magnetic equator with a bounce-period of approximately 10 seconds. The bounce-distance, however, will be very small. If the pitch angle decreases, the mirror point will be located at larger ( $B_m$ ) values (also corresponding to larger  $B/B_o$  values) which places the mirror points farther from the magnetic equator along the magnetic field line. Therefore, the bounce-distance increases, but the bounce-period is still approximately 10 seconds. However, particles generally do not enter the Earth’s magnetosphere at very small angles to magnetic field lines; it can be expected that more particles will be

mirrored at smaller  $B/B_o$  values than larger ones. If a particle were to enter the magnetosphere at a very small angle, there exists a high probability that it will have a very large bounce-distance that carries it into the Earth's atmosphere where it will collide with neutrals and scatter from its mirroring-track.

The third adiabatic, or flux, invariant can be described as a particle drifts around the Earth. As a particle experiences these motions, it "will follow trajectories that maintain a constant magnetic flux" [Tascione, 1994]. In this case, magnetic flux is defined as the number of magnetic field lines enclosed in a particle's orbit. The magnetic flux will remain constant if changes in the Earth's magnetic field occur on a scale greater than the time it takes for a particle to orbit the Earth [Parks, 2004]. Of the three adiabatic invariants, this is the invariant that is most easily violated. Drastic changes in the Earth's magnetosphere, especially during a geomagnetic storm, can occur well within the orbital period of a particle which is approximately 8 minutes.

### **DSP-21 Overview/Orbital Characteristics**

The Defense Support Program-21 (DSP-21) satellite was launched to support an United States missile defense and surveillance system. At an approximate altitude of 36,000 km and near-zero inclination, depicts the satellite's orbit as geosynchronous [Space and Missile Systems Center, 2000]. If the rotation and magnetic axes were co-aligned, DSP-21 would be located at an L-shell of 6.6 throughout its orbit. However, due to the Earth's magnetic axis being approximately 11.5 degrees off of the rotation axis, DSP-21 will be located at an L-shell range of 6.5-6.7. Figure 11 shows the approximate location of DSP-21 relative to the Earth and other L-shell values.

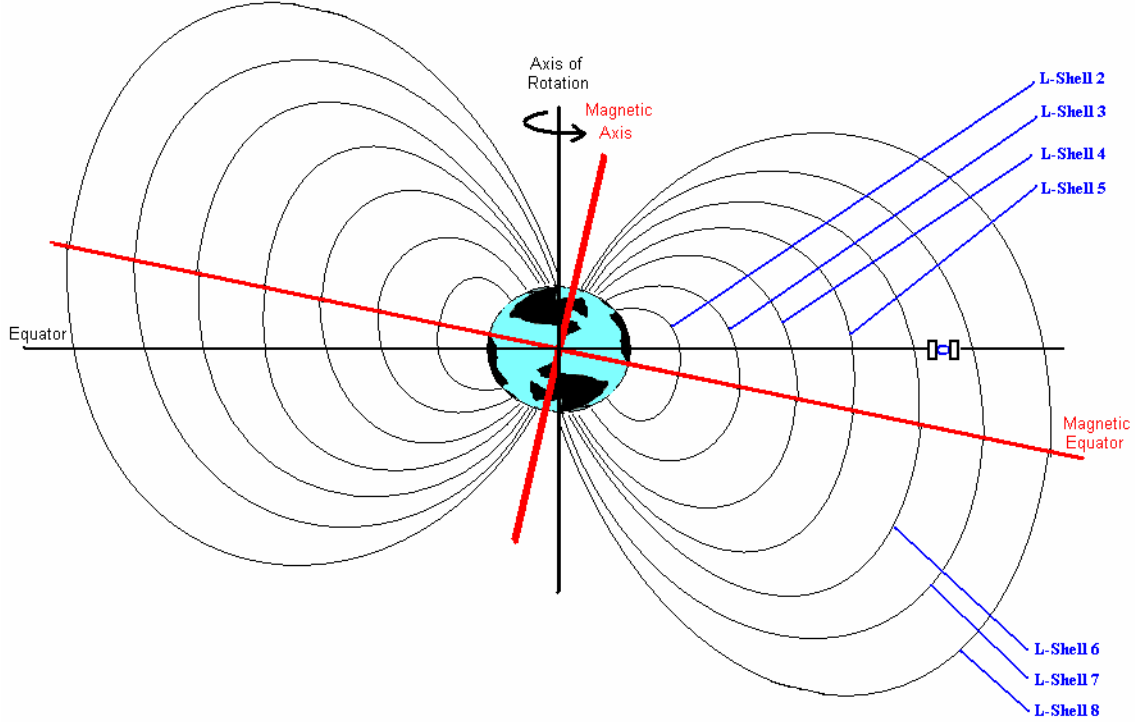


**Figure 11. DSP-21 is located near the geosynchronous orbit L-shell. The offset of the magnetic axis from the rotation axis locates DSP-21 in the range of L-shell 6.5-6.7.**

### TSX-5 Overview/Orbital Characteristics

On 7 June, 2000, the Tri-Service Experiment-5 (TSX-5) satellite was launched [Brautigam, 2001]. The TSX-5 orbit is elliptical and its altitude varies from 410 km (perigee) to 1710 km (apogee) [Brautigam, 2001]. The differences in perigee and apogee make this orbit slightly elliptical; the eccentricity is approximately 0.087. The major axis of the apogee and perigee moves approximately 1.0 degrees per day in a range from 69 degrees north latitude to 69 degrees south latitude. The low altitudes give the satellite a fairly short orbital period: 105 minutes [Brautigam 2001]. TSX-5 does not orbit the Earth near the equatorial plane; it has an inclination of 69 degrees classifying it as a polar orbit [Brautigam, 2001]. The high inclination and altitude allow the satellite to travel in a

general direction from west to east with respect to the Earth, while crossing many different L-shells along its orbital path. As Figure 12 illustrates, the TSX-5 satellite crosses low L-shell levels at low and mid-latitudes and higher L-shell values near the poles.

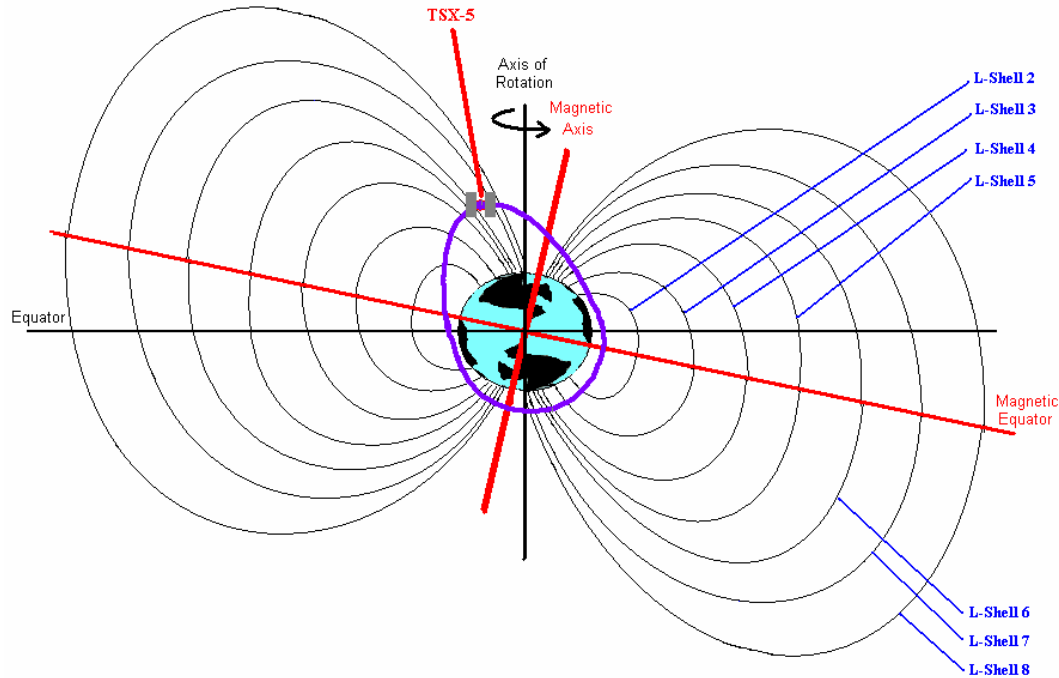


**Figure 12. TSX-5 crosses many L-shells in a single orbit including the L-shell range 6.5-6.7.**

## CEASE Instrumentation

The Compact Environmental Anomaly Sensor (CEASE) is a low-powered, light weight, and small sensor (Figure 13). This instrument has a mass of only 1 kg, a volume of  $820 \text{ cm}^3$ , and consumes nearly 1.5 Watts of power [Dichter, 1998]. The CEASE instrument contains two dosimeters: DD1 and DD2. Each dosimeter consists of a  $9 \times 9 \text{ mm}^2$  by  $500 \text{ }\mu\text{m}$  p-i-n silicon diodes plate [D. Brautigam, private communication, 2004; Dichter, 2001]. As a particle transverses one of the silicon plates, it loses “kinetic energy

by generating electron-holes in the silicon" [Dichter, 1998]. "The detectors are voltage biased to collect the electrons and holes at separate electrodes causing a small current to flow. The integral of the current is then proportional to the total energy deposited by a particle while traversing the sensor" [Dichter, 1998]. The deposition energy is then recorded.



**Figure 13. The CEASE Instrument: a small, light-weight, and low-power particle detector [Dichter, 1998].**

Each dosimeter is able to characterize electrons from protons in given circumstances. Typical electron energy deposition is approximately 100-400 keV; typical proton energy deposition is approximately 1-10 MeV [Dichter, 1998]. Based on the typical energy depositions of each type of particle, two energy ranges were developed: Low Linear Energy Transfer (LOLET) and High Linear Energy Transfer (HILET). Particles that deposit energies less than 1 MeV are designated LOLET and particles that deposit energies greater than 1 MeV are designated HILET [Dichter, 1998].

The DD1 dosimeter is covered by approximately 80 mils of aluminum shielding [Brautigam, 2001]. Electrons with energies greater than 1.2 MeV and protons with energies greater than 25 MeV can penetrate this shielding [D. Brautigam, private communication, 2005]. The particles of these energy ranges typically deposit 0.5 MeV to 0.85 MeV (LOLET) on the dosimeter after penetrating the aluminum shielding [D. Brautigam, private communication, 2005]. Due to the fact that both particles of the given energy ranges can penetrate the shielding and deposit energies, high energy protons, from a solar flare, for example, could contaminate the CEASE recorded electron flux values. Such instances can render the electron flux values useless in this effort. Therefore, proton contamination will be considered and is described in Chapter III.

Only particles in front of the sensor are to be considered. “By design, the dosimeter is primarily sensitive to radiation for the entire hemisphere above the sensor” [Dichter, 1998]. Particles traveling toward the sensor from below the dosimeter must transverse the spacecraft walls and interior as well as the sensor walls” [Dichter, 1998]. “This material will stop low energy particles and significantly reduce lower hemisphere flux reaching the dosimeter” (Figure 14) [Dichter, 1998]. Considering only the sensor’s upper hemisphere, the CEASE dosimeter has a geometric factor of  $2.54 \text{ cm}^2 \text{ sr}$  [Dichter, 1998].

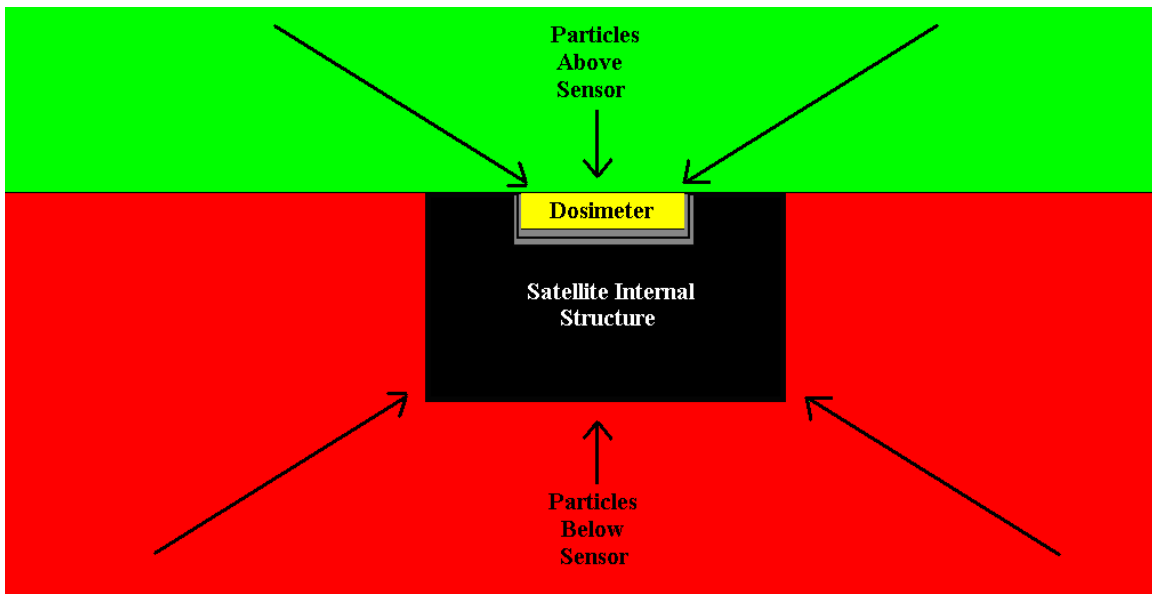


**Figure 14.** The locations of the dosimeters onboard CEASE are situated such that the hemisphere above the dosimeter will encounter particles and the bottom hemisphere will not.

### III. Methodology

#### Chapter Overview

This chapter covers the methods in which the progression of electron increases from GEO to LEO will be determined. First, a description of two databases used in this effort is given. Next, electron event isolation and selection is described followed by the determination of event onsets at GEO and LEO. Finally, the method used to determine the time progression of an electron event from GEO to LEO is expressed.

#### Database Description

Two databases are used in this effort. The first data base is the “High Time Resolution Database” and contains information from both DSP-21 and TSX-5 satellites. The CEASE data from the TSX-5 satellite consists of Universal Time (UT), geodetic altitude (km), geodetic latitude, longitude, local magnetic time, altitude (in Earth radii), magnetic latitude, L-shell, and B/B<sub>0</sub>. The TSX-5 information was collected every five seconds only when the location of TSX-5 was between an L-shell of 6.5 and 6.7. The five second intervals were then averaged over the interval when TSX-5 passed continuously through the L-shell range of 6.5-6.7 [D. Brautigam, private communication, 2004]. Although the CEASE instrument contains two dosimeters, only the LOLET data from the DD1 dosimeter is to be analyzed. The units for the dosimeter are particle counts per second. The time span for the database is from 9 Aug 01 through 8 Jun 04.

The High Time Resolution Database also contains CEASE data from the DSP-21 satellite. Five second particle data collected from the DD1 dosimeter onboard DSP-21 was averaged every five minutes. The DSP-21 five-minute interval closest to the UT of the TSX5 average time was recorded. It is assumed that DSP-21 continually crossed L-

shells in the range of 6.5-6.7 throughout the time span of the database. LOLET data from both DD1 dosimeters onboard TSX-5 and DSP-21 will be compared. Units of the dosimeters onboard the satellites is counts per second.

The second database is called the “Daily Average Database.” It contains daily CEASE data from TSX-5 and DSP-21 satellites. For each day, the TSX-5 CEASE data five second intervals were averaged together only when TSX-5 experienced an L-shell between 6.5 and 6.7. For the DSP-21 satellite information, each five second interval was averaged together over a 24-hour period. The Daily Average Database contains three pieces of information for each satellite: number of observations, the average electron flux, and one standard deviation of the particle count.

Also included in the Daily Average Database is GOES-10 particle information. The Geostationary Operational Environmental Satellite-10 (GOES-10) is a weather satellite at a geosynchronous orbit near the equatorial plane [NOAASIS, 2003]. Like the TSX-5 and DSP-21 daily average data, particle information from the GOES-10 satellite contains data for a 24-hour period. The GOES-10 information holds flux values for electrons with energies greater than 2 MeV and protons with energies greater than 10 MeV.

### **Event Isolation/Determination**

From the Daily Average Database time span, periods of particle elevated above the background values are deemed possible electron events. These possible events will be determined by observing only the DSP-21 particle count information from the Daily Average Database. Events are isolated by dramatic rises in electron counts that are preceded and followed by several days of relatively low electron counts.

Next, the basic idea of an electron event is applied for both particle counts from DSP-21 and TSX-5. The basic concept of an electron event would be one that begins with several days of consistently low flux values, also called a “quiet period”. Following this quiet period would be a dramatic increase in electron flux to a peak value. Next, a decrease in flux values trails the peak value followed by flux values returning to the approximate level as the quiet period before the initial increase. Figure 15 shows a hypothetical basic concept electron event and a hypothetical irregular electron event is shown by Figure 16. Irregular events are to be avoided due to their complexity; several increases and decreases in particle counts over a short time period may be the effect of more than one electron event. Event complexity increases the ambiguity of the event onset and peak occurrences. Therefore to simplify the event determination procedure, only basic concept events will be used for analysis.

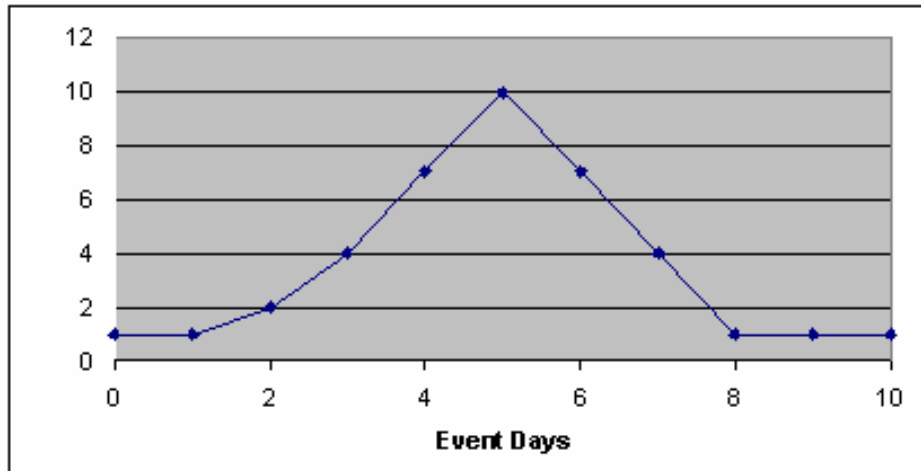


**Figure 15. Basic Concept Event.** A monotonic increase to a peak value in electron counts per second followed by a monotonic decrease to pre-events electron counts per second values.

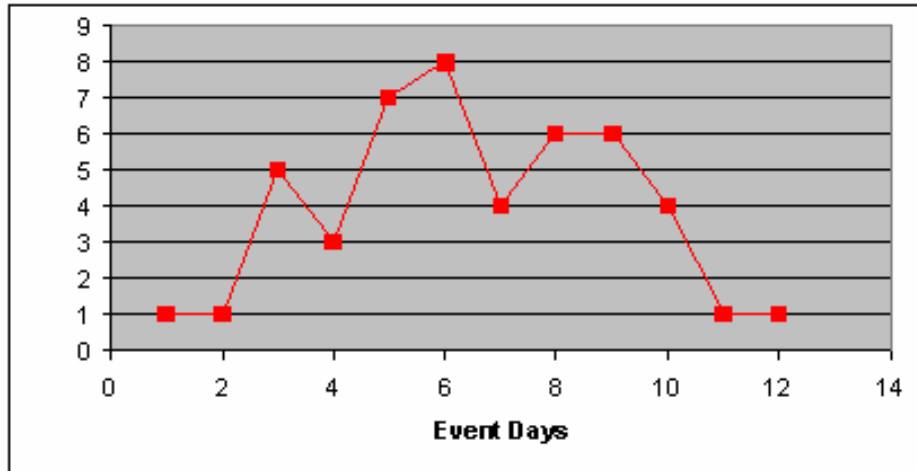


**Figure 16. Irregular Event. Several increases and decreases in electron count values within the same electron event period.**

Once electron event periods are selected, proton contamination must be considered. As described in Chapter II, high energy particles can contaminate the dosimeter making it difficult to distinguish electrons from high energy protons. Data from GOES-10 satellite will be used to determine proton contamination in the CEASE data from DSP-21 and TSX-5 by comparison. If the GOES-10 data shows significant proton flux values during the time of a selected electron event, the selected electron event will be disregarded.

### **Hemisphere Separation**

As explained in Chapter II, particles mirror along a given magnetic field line; more particles will be mirrored at lower  $B/B_o$  values than higher  $B/B_o$  values. This led to the discovery that the TSX-5 apogee, reaching higher into the magnetosphere, will encounter lower  $B/B_o$  values, and record higher electron fluxes than the perigee. The perigee, located in the opposite hemisphere of the apogee, reaching much lower altitudes, will encounter higher  $B/B_o$  levels and, therefore, the CEASE instrument will record lower

electron counts (Figure 17). As a result, averaging the electron counts from both hemispheres together will produce an inaccurate representation of the true average and a large standard deviation. In Figure 17,  $B_1$  represents the TSX-5 apogee and  $B_2$  represents the perigee. The  $B_1$  position extends higher into the magnetosphere than  $B_2$ ; thus,  $B_1$  shows TSX-5 at a lower  $B/B_0$  location. The lower the  $B/B_0$  value, the higher the electron counts the satellite will be exposed to.

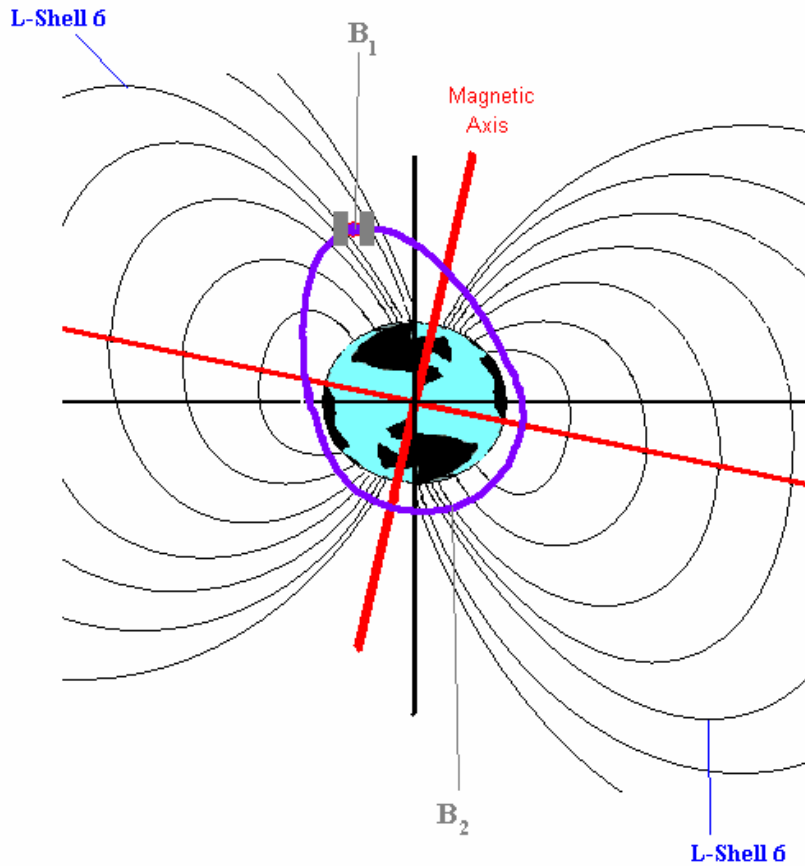


**Figure 17. TSX-5 Apogee/Perigee Location in opposite hemispheres. The apogee of TSX-5 ( $B_1$ ) shows the satellite at a higher altitude than the perigee ( $B_2$ ). ( $B_1$ ), located at a lower  $B/B_0$  value, will encounter higher electron count values than ( $B_2$ ).**

It is more applicable to use only the electron event counts from TSX-5 when the TSX-5 apogee was near latitude limits of 69 degrees. This provides a relatively low B/Bo value in the desired L-shell range and is a more desirable location to detect an electron event at LEO. Perigee location near the latitude limits may lead to little or no electron count increases at lower altitudes during an electron event at LEO. Therefore, the electron count values from the hemisphere that contains the TSX-5 apogee near latitude limits will be used for further analysis. The hemisphere containing the TSX-5 apogee at high latitudes will be referred to as the “significant hemisphere.”

### **Standard Error of the Mean**

The error for each electron count measurement recorded by CEASE is not known via the databases. Even if the electron count uncertainty was known, little, if any, information can be achieved without a relationship between the variability the electron count values and B/B<sub>o</sub>, magnetic local time, and L-shell. To account for this, a standard error of the mean will be used in each database. While the standard deviation shows how “spread out” the sampled electron count values are relative to one another, it does not accurately represent how the sampled average electron count relates to the actual electron count mean. The standard error of the mean (also called the standard error or standard deviation of the mean) represents how far off the sampled mean deviates from the actual population mean if the measurements are random and independent [Taylor, 1997]. The equation and variables for standard error are as follows:

$$\sigma_s = \frac{\sigma}{\sqrt{N}} \quad (10)$$

$\sigma_s$  = standard error

$\sigma$  = standard deviation

$N$  = number of samples

Each standard error gives a confidence as to how close the sampled mean is to the population mean much like standard deviation: one ( $\sigma_s$ ) gives a 66% confidence, two ( $\sigma_s$ ) gives a 96% confidence, and so forth. Obviously, as the number of samples increases, the standard error decreases. Therefore, the more measurements of a population are collected, the smaller the uncertainty of the population mean becomes.

As stated above, not only is the uncertainty for each CEASE measurement is not known, the relationship between the location (magnetic local time, B/Bo, and L-shells) and the electron counts values is not known either. To account for this, the standard error will be used as the electron flux uncertainty. To apply this method, changes in electron flux values on a timescale of less than one day are neglected; it is assumed that electron fluxes remain the same for a given 24-hour period. This limits the time uncertainty of each database to  $\pm 0.5$  days.

The Daily Average Database has the GEO electron flux values, number of observations, and standard deviation for a 24-hour period. Therefore, the GEO electron flux values and standard error in the desired timescale will come from this database. A 24-hour LEO electron flux values will be calculated via the High Time Resolution Database. As stated above, only CEASE information from the significant hemisphere will be used, and this data will be averaged over a 24-hour period. Uncertainty for these 24-hour values will be represented by the standard error.

## Onset Determination

To determine when the actual electron event occurred at GEO, thresholds will be calculated. Thresholds for the DSP-21 CEASE electron count data are to be determined by the average electron flux of a relatively inactive period within 6 months of the event. The daily period when the GEO electron count exceeds the electron count threshold will be the GEO onset. The exact threshold calculation is as follows:

$$DSP_{Threshold} = Q + 2 \times X \quad (11)$$

$DSP_{Threshold}$  = GEO electron count value threshold

$Q$  = Average electron counts of quiet period

$X$  = Standard error of quiet period electron count average

The onset day of an electron event at LEO will be determined as the day that shows the beginning of a monotonic increase of electron count values to the peak electron count value for the event. It is expected that each daily electron count value during an electron event at LEO will have an uncertainty determined by the standard error. Depending on the orientation of error bars, overlapping uncertainty in count values could exclude event days as electron event onsets. Figure 18 shows a basic concept electron event with uncertainty in the electron count values. The peak in electron counts occurs on event day five. Prior to the peak day, it appears that event day one is the onset of the electron event. However, the error bars of event day one and event day two overlap. With this error bar overlap, it is not certain that event day two has a larger electron count. Event day one is then determined not to be the onset day. Event day two and event day three also have overlapping error bars; it is not certain that event day two has a larger value than event day three. Therefore, event day two is not the onset. The error bars of event day three and event day four do not overlap showing there is little doubt that the

electron count increases from event day three, through event day four to the peak at event day five. Therefore, event day three is determined to be the onset of the electron event.

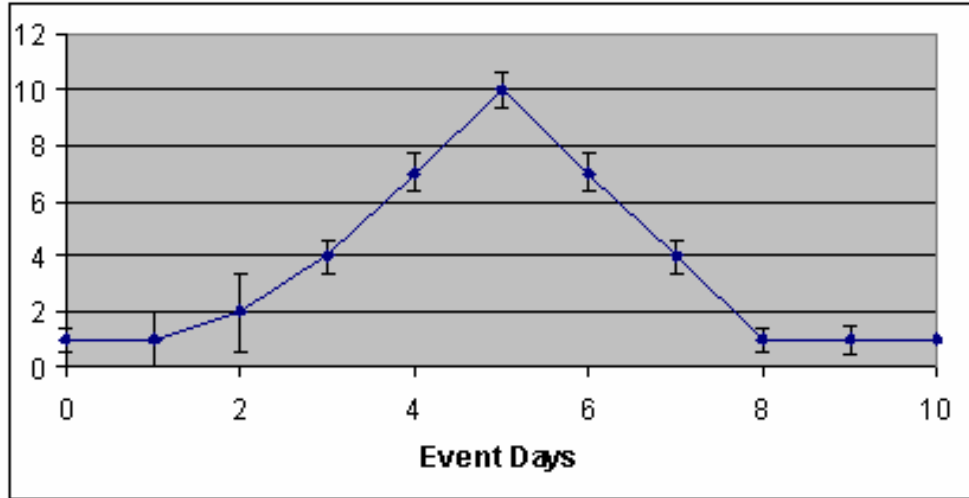


**Figure 18. LEO Onset Determination Example.** LEO onset is determined by the certainty of electron count value increase.

### Electron Event Progression

Electron event progression from GEO to LEO is the elapsed time between the two onset dates. Once the event onsets are determined, the progression time can be determined by subtracting the two onset dates. To calculate the total uncertainty in time, adding the two time errors gives the maximum error in time [Taylor 1997]. The fact that the time uncertainty is limited to  $\pm 0.5$  days and the onset at GEO or LEO is specified to one specific day would lead to an uncertainty in time of 1.0 days. However, if the CEASE measurements were assumed to be random and independent from one another, the quadratic sum formula can be used (Equation 11) [Taylor, 1997].

$$\partial q = \sqrt{(\partial x)^2 + (\partial y)^2 + \dots + (\partial z)^2} \quad (12)$$

The uncertainties ( $\partial x$ ) and ( $\partial y$ ) are the measurement errors, and ( $\partial q$ ) is the total error. In this case, the uncertainty of each measurement in time is 0.5 days. Therefore, the total time uncertainty is 0.7 days for the progression of each electron event from GEO to LEO according to Equation 11. This is less than simply adding the time uncertainties for the onset days of each orbit.

## IV. Results and Analysis

### Chapter Overview

This chapter covers the results achieved using the methods described above.

First, the results of electron event isolation and selection are described followed by the hemisphere separation findings. Next, the onsets of the electron events at GEO and LEO are shown and compared. Finally, correlation between electron events and solar geo-physical parameters are described.

### Event Isolation/Selection

As described in Chapter II, solar minimum leads to a lifetime increase of coronal holes causing the number of high speed streams reaching the Earth to increase. Therefore, it was expected to observe more electron events toward the latter half of the database time span. Figure 19 shows the time frame of the High Time Resolution and Daily Average databases in reference to Solar Cycle 23 [NOAAb, 2004 ]. As can be observed, a significant increase in particle event frequency and intensity are observed toward the later half of the database timeframe (Figure 20).

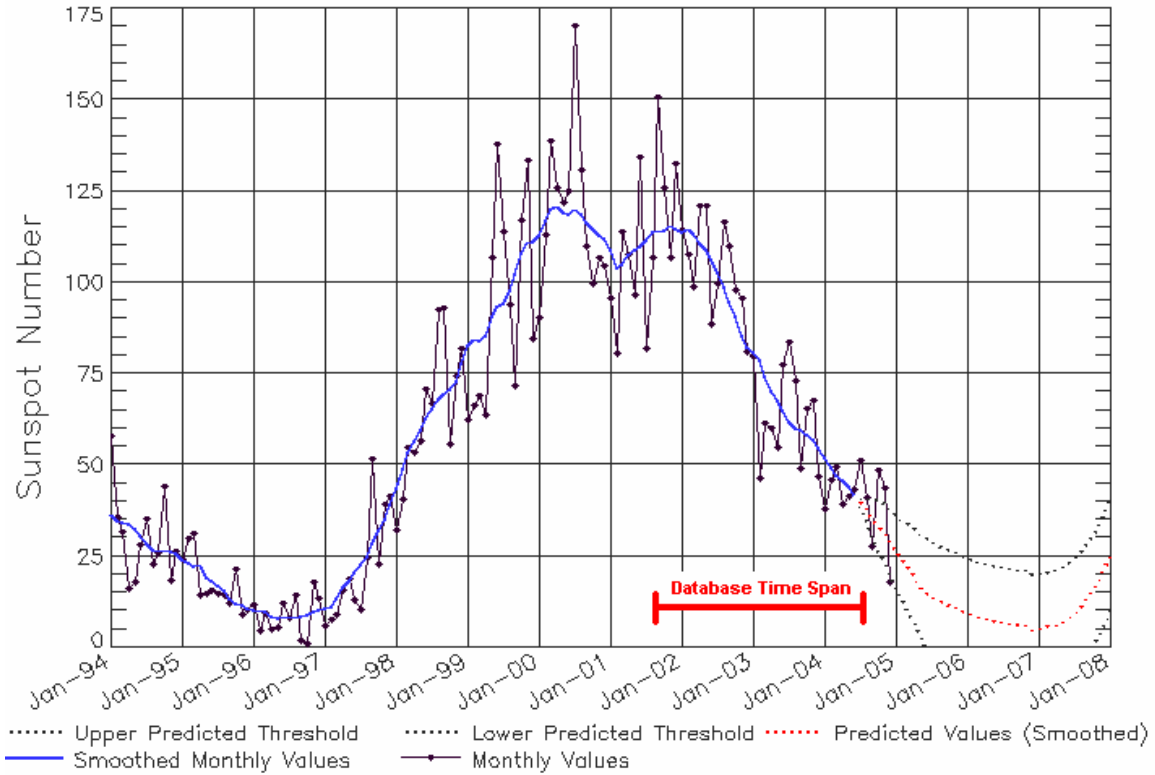


**Figure 19.** The sunspot number versus time for Solar Cycle 23. The red horizontal line refers to the time span of the Daily Average and High Time Resolution Databases. As the plot shows, the databases occur toward solar minimum of Solar Cycle 23 [NOAAb, 2004].

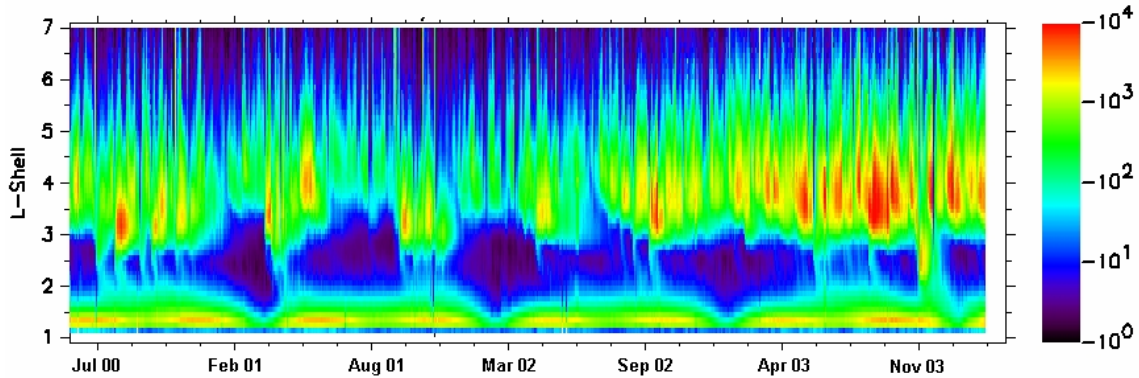


**Figure 20.** Particle activity and intensity as recorded by the CEASE instrument (dosimeter D1, LOLET deposition energy range) onboard TSX-5. As time progresses, the plot approached solar minimum but yet electron activity and intensity increase. [D. Brautigam, private communication, 2004]

CEASE data from the DSP-21 satellite taken from the Daily Average Database was used to selecte electron events using the isolation criteria in Chapter III. Table 2 lists isolated events and significant characteristics, such as peak and estimated electron count increase, for each event.

**Table 2. Isolated Electron Events from the Daily Average Database via CEASE data from DSP-21.**

Event Number	Pre Statistics		Event Statistics		Post Statistics
	Beginning Pre-Quiet	End Pre-Quiet	Event Peak	End Event	End Post-Quiet
	Day	Day	Day	Day	Day
1	31-Aug-01	3-Sep-01	7-Sep-01	8-Sep-01	14-Sep-01
2	8-Jan-02	11-Jan-02	16-Jan-02	20-Jan-02	6-Feb-02
3	2-Feb-02	7-Feb-02	9-Feb-02	18-Feb-02	26-Feb-02
4	1-Mar-02	5-Mar-02	8-Mar-02	10-Mar-02	12-Mar-02
5	30-Mar-02	31-Mar-02	5-Apr-02	11-Apr-02	18-Apr-02
6	1-Jul-02	6-Jul-02	8-Jul-02	12-Jul-02	13-Jul-02
7	12-Jul-02	19-Jul-02	23-Jul-02	27-Jul-02	2-Aug-02
8	27-Aug-02	4-Sep-02	6-Sep-02	8-Sep-02	10-Sep-02
9	27-Sep-02	2-Oct-02	6-Sep-02	8-Oct-02	17-Oct-02
10	19-Dec-02	23-Dec-02	31-Dec-02	8-Jan-03	14-Jan-03
11	28-Jan-03	30-Jan-03	1-Feb-03	2-Feb-03	3-Feb-03
12	12-Mar-03	14-Mar-03	25-Mar-03	27-Mar-03	28-Mar-03
13	27-Mar-03	30-Mar-03	2-Apr-03	6-Apr-03	10-Apr-03
14	25-Jul-03	27-Jul-03	3-Aug-03	6-Aug-03	8-Aug-03
15	18-Aug-03	21-Aug-03	27-Aug-03	28-Aug-03	3-Sep-03
16	16-Sep-03	17-Sep-03	20-Sep-03	24-Sep-03	25-Sep-03
17	24-Sep-03	25-Sep-03	28-Sep-03	2-Oct-03	14-Oct-03
18	2-Oct-03	14-Oct-03	17-Oct-03	25-Oct-03	27-Oct-03
19	25-Oct-03	31-Oct-03	2-Nov-03	5-Nov-03	8-Nov-03
20	7-Nov-03	11-Nov-03	13-Nov-03	14-Nov-03	15-Nov-03
21	14-Nov-03	15-Nov-03	19-Nov-03	21-Nov-03	23-Nov-03
22	21-Nov-03	23-Nov-03	27-Nov-03	1-Dec-03	6-Dec-03
23	6-Dec-03	8-Dec-03	18-Dec-03	21-Dec-03	28-Dec-03
24	10-Feb-04	12-Feb-04	17-Feb-04	22-Feb-04	29-Feb-04
25	18-Mar-04	27-Mar-04	30-Mar-04	4-Apr-04	6-Apr-04

Each event in Table 2 was plotted and compared against the GOES-10 proton data for signs of proton contamination. If the DSP-21 or TSX-5 plot shows signs of proton contamination, that event was stricken from further analysis. Figure 21 shows Electron Event #1 and Figure 22 shows the GOES-10 proton data for the same time period at

Event #1. The GOES-10 data does not show any significant proton counts for the event period. The increases of particle counts starting at approximately 5 Sep 01 can be contributed to by a vast majority of electrons. Therefore, Event #1 is said to be a non-contaminated event. However, Figure 23 shows a count increase from 6 Jul 02 to 8 Jul 02 for the TSX-5 CEASE data. Figure 24 shows the proton data from GOES-10 for the same period as Event #6; the GOES-10 data also shows an increase of counts for 6-8 Jul 02. Although the GOES-10 count data for these dates may be insignificant compared to the DSP-21 CEASE count data, it appears that the proton experienced by GOES10 could have an effect on the TSX-5 CEASE count recordings. The CEASE instrument onboard TSX-5 could have experienced electrons and a significant amount of protons as well. It is possible for proton contamination to have occurred at LEO for this event. Therefore, this event, as well as Event #19, was disregarded from further analysis due to possible proton contamination. Each of the electron events are compared to GOES-10 proton data in Appendix A.

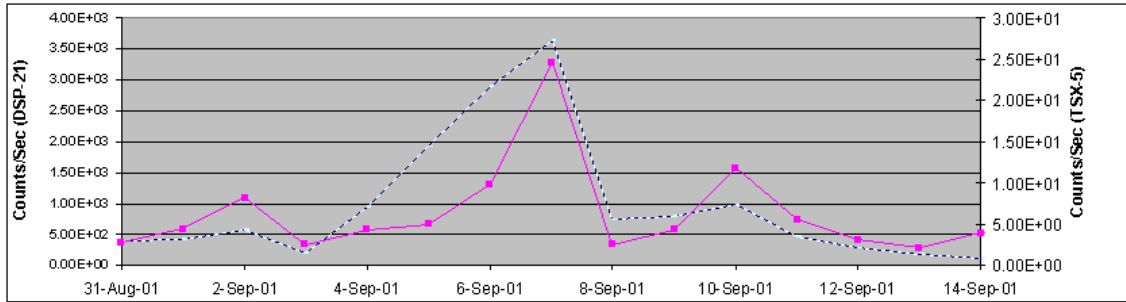


**Figure 21. Isolated Electron Event #1 from the Daily Average Database. Electron counts from GEO (blue dashed line) and LEO (pink solid line) are shown.**

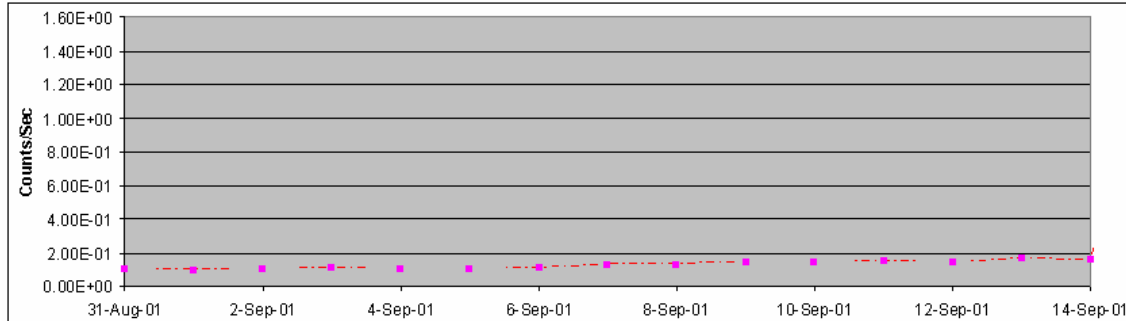


**Figure 22. GOES-10 (GEO) Proton Data for Event #1 shows little proton activity and suggests that Event #1 is not contaminated by protons.**

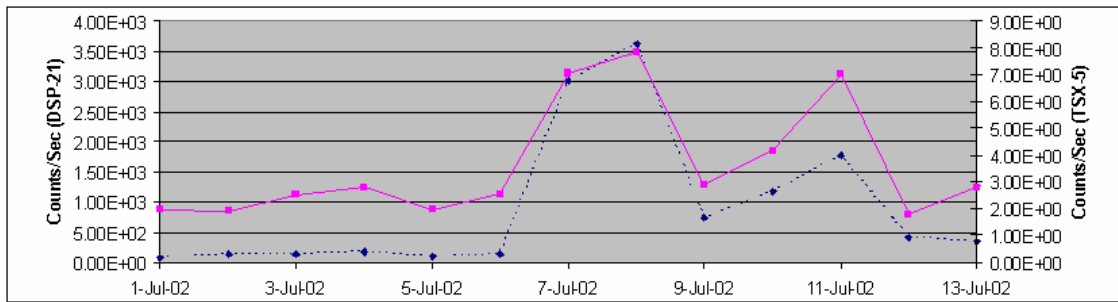


**Figure 23. Isolated Electron Event #6 from Daily Average Database. GEO (dashed blue line) and LEO (solid pink line) electron counts are shown.**

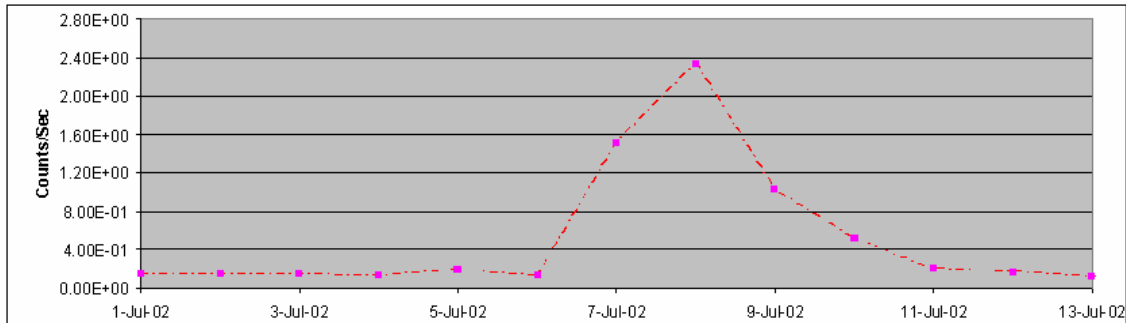


**Figure 24. GOES-10 (GEO) Proton Data for Event #6 shows a proton count increase at approximately the same time as the GEO and LEO plots suggesting the electron values are contaminated with proton recordings.**

The figures below show the difference between an electron event that meets the basic concept of an electron event (Figure 25) and one that does not (Figure 26). It is possible that two electron events may have occurred in close time proximity to produce

the results in Figure 23, but an irregular electron event complicates the onset analysis. Irregular events may be used for analysis if the relationship of  $B/Bo$ , magnetic local time, and L-shell location is determined.

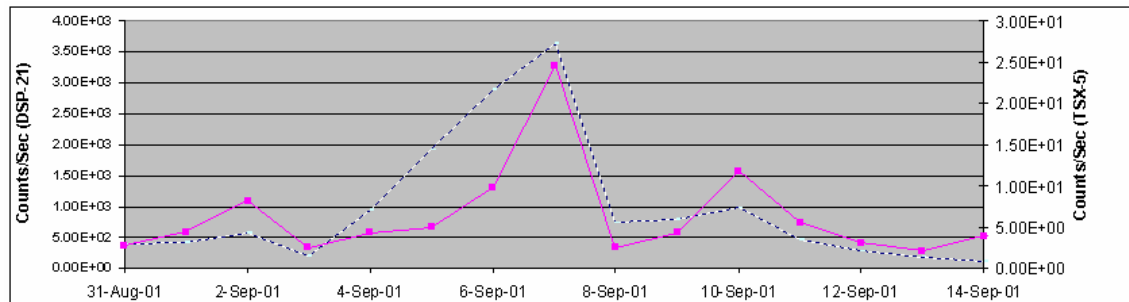


**Figure 25. Electron Event #1 shows the characteristics of a basic concept electron event; monotonic increase in electron count values to a peak value.**

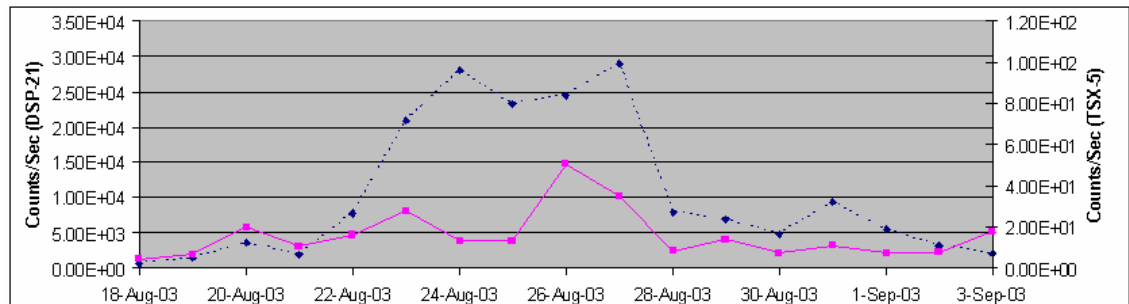


**Figure 26. Event #15 does not follow the criteria of a basic concept electron event for both GEO and LEO electron count values. Two peaks in electron counts are shown to occur in both orbits.**

If it were assumed that Figure 26 represents a single electron event, determining the onset of the electron count increase becomes difficult. While the onset of the electron event at GEO would most likely be 21 Aug 03, the onset of the electron event at LEO is not clear. First, there is not a clear pre-event electron level for the TSX-5 CEASE data. Second, if the lowest electron count level was designated as the onset (say 19 Aug 03), the electron levels increase and decrease several times before reaching a local maximum value of nearly 50 counts per second on 26 Aug 03. It is difficult to determine the peak

value and occurrence of an electron event. Finally, with multiple electron count peak points, it becomes difficult to determine the time increment of the event. The rise in electrons at GEO from 21-24 Aug 03 may have caused the increase in electron counts at LEO from 21-23 Aug 03 or the increase from 25-26 Aug 03. Also, the electron count increase at LEO from 25-26 Aug 03 could have caused the second increase from 25-27 Aug 03 at GEO. Multiple electron count peaks occurring in a single event timeframe makes any correlation determination impossible. Of the 25 original events, Events #1, #2, #4, #5, #10, #11, #14, #16, #17, #22, #23, and #24 met the criteria listed above and were subjected to further analysis.

### **Hemisphere Separation**

Figure 27 shows the daily average of the High Time Resolution data for TSX-5 for Event #1. In this figure, the error bars represent the standard error. As the plot shows, the TSX-5 experienced higher electron counts in the southern hemisphere than the northern hemisphere. In fact, the northern hemisphere shows little change in electron counts during the electron event. TSX-5 CEASE data of the significant hemisphere will be compared to the DSP-21 data. It was determined that the apogee-perigee axis for Events #2, #10, #14, #16, #17, and #23 did not approach the latitude limits of 69 degrees. Further analysis of these events requires a relation determination of the electron count values and B/Bo, magnetic local time, and L-shell values. [Onsager, et al, 2004, Miyoshi, et al, 2004]. For simplicity, these events were disregarded.

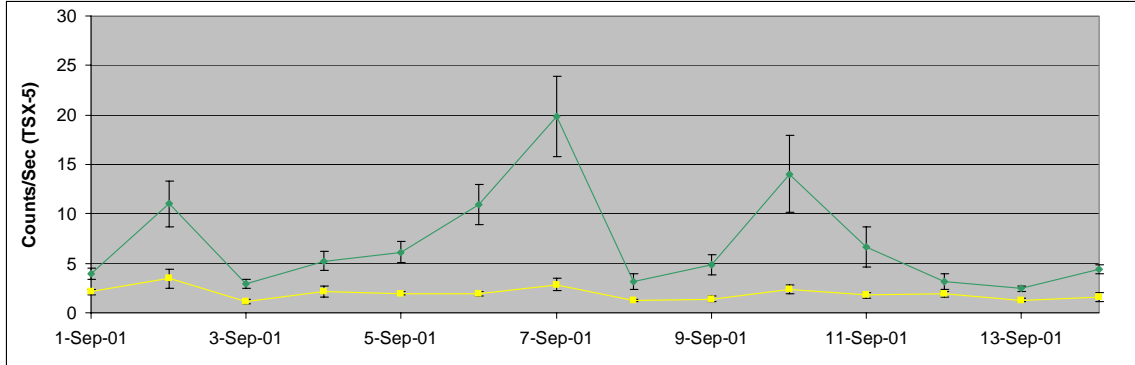


**Figure 27. Plot of Event #1.** The green plot represents the electron count values of TSX-5 apogee located in the southern hemisphere, reaching lower  $B/B_0$  values and therefore, larger electron count values. The yellow plot represents electron count values of TSX-5 in the northern hemisphere, reaching higher  $B/B_0$  values and therefore lower electron count values. The error bars represent standard error.

## GEO Onset Determination

Figure 28 shows the DSP-21 electron flux threshold level for Event #1 at 204 particles per second, the average electron count per second for the period of 19 Oct 01-29 Oct 01 (blue horizontal line). Therefore, the onset of the electron storm at GEO is determined to be 3 Sep 01.

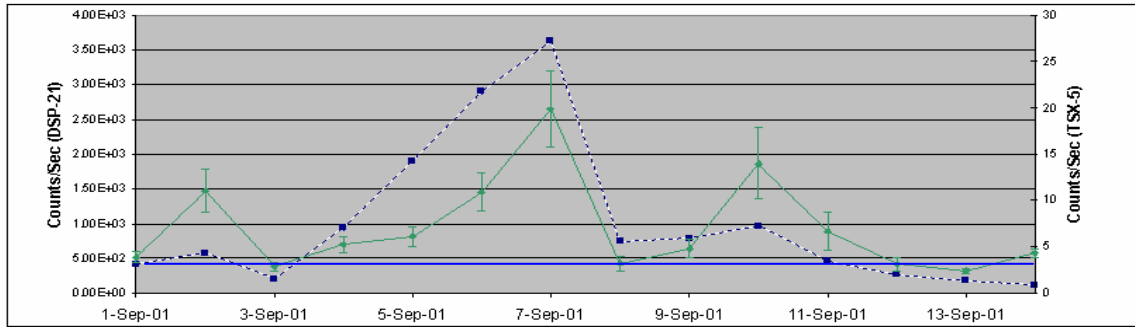


**Figure 28.** The electron event onset at GEO (dashed blue line) is determined by electron count values exceeding a quiet time threshold (solid blue horizontal line). The solid green line represents the LEO electron data of the significant hemisphere of TSX-5.

## LEO Onset Determination

As described in Chapter III, the LEO onset of an electron event was determined by the previous day showing no overlapping uncertainty for conjoining days, yet still showed promise of an electron count increase. In Figure 29, 5 Sep 01 shows no doubt of a beginning of electron count increase to a peak value on 7 Sep 01. The previous day, 4 Sep 01, has an uncertainty that overlaps with 5 Sep 01. Uncertainty in the increase of electron count values exists from 4 Sep 01 to 5 Sep 01, but there is no doubt that the electron count increased from 5 Sep 01 through 6 Sep to 7 Sep 01.

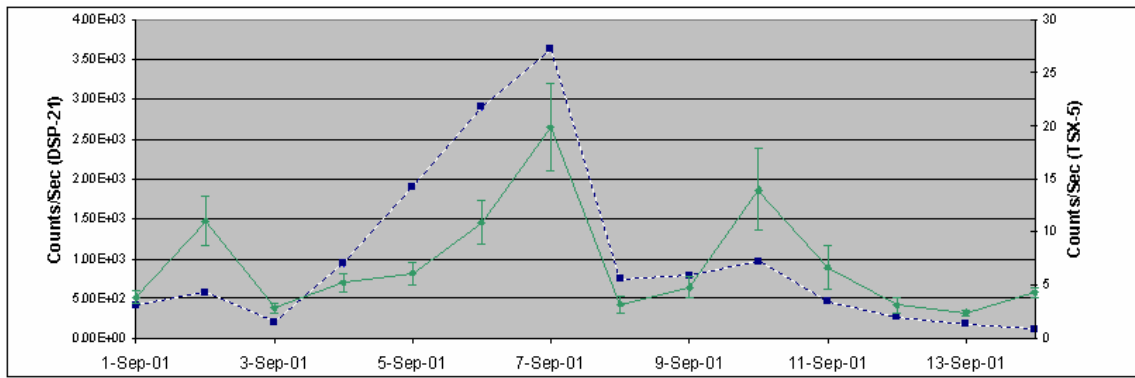


**Figure 29. The LEO onset for Event #1 is determined to be 5 Sep 01; it shows an increasing electron count value to a peak value on 7 Sep 01.**

## Electron Event Progression

The elapsed time from the onset of each electron event at GEO and LEO was calculated. As described in Chapter III, this was determined by subtracting the GEO onset date from the LEO onset date. As in the case of Event #1, the electron event onsets at GEO and LEO are 3 Sep 01 and 5 Sep 01 respectively. A two day separation exists between the onsets with an uncertainty of 0.7 days. Figure 30 below shows the time difference of electron onsets between GEO and LEO for each event with time

uncertainty. The techniques used to neglect electron flux changes on the order of less than one day and determine the electron event onsets at GEO and LEO limited the time uncertainty of electron event progression to 0.7 days for all events.

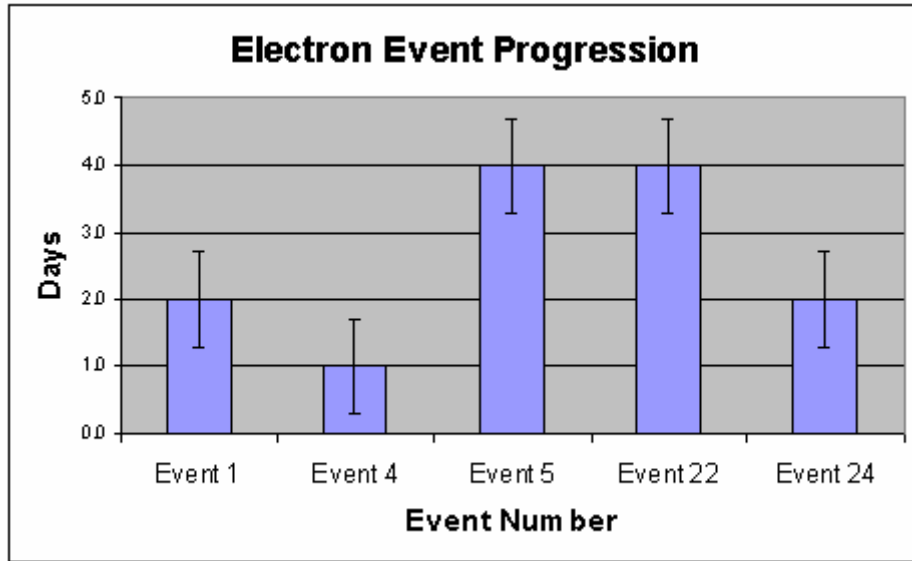


**Figure 30. Electron Event Progression Timing from GEO to LEO for Electron Events #1, #4, #22, #24. The error bars represent the same uncertainty for each event progression: 0.7 days.**

### Electron Events and Solar-Geophysical Parameters Correlation

Each electron event was compared to geomagnetic indices such as Dst and Kp to determine if the events were related to any geomagnetic activity. However, there appeared to be no relation between the indices and the electron events. Reports from the Space Environment Center (SEC) were collected for the time periods of each event. Each report was then compared to the timeline of each event to see if a correlation existed. It appeared that high speed solar wind streams, caused by coronal holes, occurred approximately the same time as the determined GEO onsets for the five electron events.

Furthering the interest of the coronal holes and high speed solar wind streams to electron events, a period of little or no electron event activity was selected: 27 Nov 01-5 Feb 02. This period was then compared to the SEC weekly reports much like the electron events as described above (Appendix E). In this time period, recurring coronal holes and high speed streams did occur without the production of electron events. This finding leads to the thought that high speed streams are necessary, not sufficient to produce an electron event.

Since characteristics of high speed solar streams are known (see Chapter II), ACE solar wind data was collected during the time period of each electron event. As Figure 31 shows, the GEO onset of Event #1 occurs near the leading edge of the high speed stream which is evident by the density increase. The LEO onset happens sometime during the trailing edge of the stream. The trailing edge of the high speed stream is evident by the decrease in solar wind speed after a significant peak. The other electron events had similar results (Appendix F).

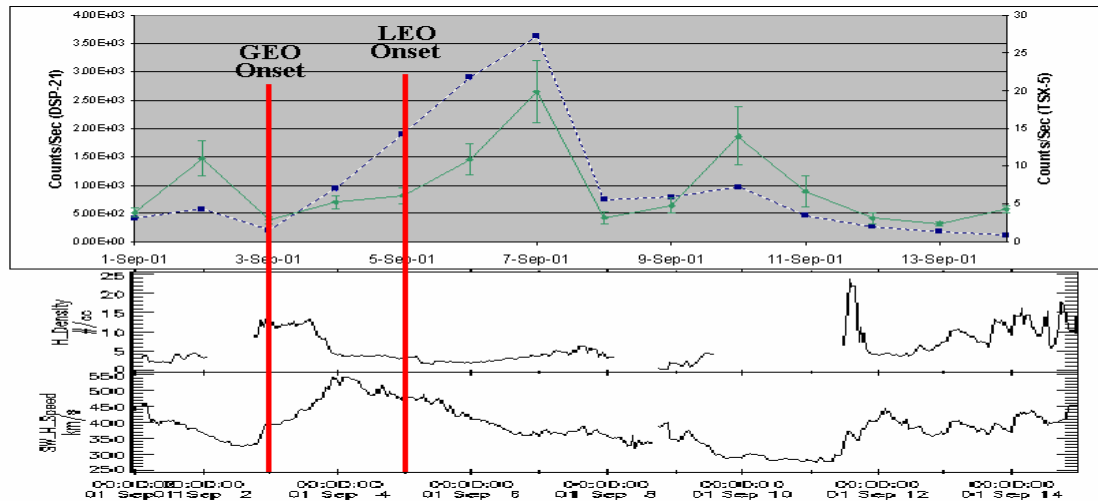


**Figure 31. Electron Event #1 with plots of solar wind data show the electron event onset at GEO occurs during the leading edge of a high speed stream and the event onset at LEO occurs during the trailing edge of the high speed stream.**

## V. Summary, Conclusions, and Recommendations

### Summary

Electron events are dramatic increases in electron fluxes. These events can start at GEO and progress to low-earth-orbit altitudes afflicting damage to mission essential DoD space systems. Charged particles are known to follow magnetic field lines in the adiabatic motion of mirroring. Electron events are thought to follow this mirroring motion but changes in pitch angle causes the electrons to experience a non-adiabatic progression along L-shells. The Compact Environment Anomaly Sensors (CEASE) onboard the DSP-21 (geosynchronous orbit) and TSX-5 (low-earth-orbit) satellites collected  $> 1.2$  MeV electron via a dosimeter. The orbits of the satellites provided the proper L-shell range (6.5-6.7) to determine electron event progression at GEO and LEO.

The onset of electron events at GEO and LEO were determined. The electron event progression time from GEO to LEO was determined to be the difference in time between the two onsets. The progression of electron events from GEO to LEO was determined to be between one and four days; this is significantly larger than a typical mirroring period. Comparing each electron event to geomagnetic indices suggests that there is little relation between the two. However, further comparison of the electron events to solar wind data suggests that high speed streams are necessary, not sufficient, for an electron event to occur.

### Conclusions

Overall, the Daily Average Database showed an increase in electron event activity toward solar minimum. As described in Chapter II, the lifespan of coronal holes increase toward solar minimum thus lasting for several solar rotations. It is suggested that the

increase in electron event activity is due to longer lasting coronal holes as the Sun approaches solar minimum.

Of the isolated electron events, hemisphere separation of TSX-5 CEASE data according to the location of the TSX-5 apogee led to a better approximation of the electron count population. The Daily Average Database provided a poor look into the TSX-5 CEASE data because the  $B/B_o$  location of the satellite varied significantly when the apogee and perigee were near high latitudes. Lower  $B/B_o$  values led to higher electron count values (as is the case of the TSX-5 apogee) and higher  $B/B_o$  values led to lower electron count values (TSWX-5 perigee).

There appears to be a slight correlation between two groups of electron event progression times. Events #1, #4, and #24 show an electron event progression time from GEO to LEO to be less than or equal to two days; Events #5 and #22 show a much larger progression time (approximately 4 days). However, such relationships may not exist due to the relatively low number of final events; five data points is not a significant sample size. Further analysis with more events would be needed to gain confidence in this relationship.

When compared to solar reports from the Space Environment Center, each electron event appeared to be the result of a high speed stream. However, it was determined that high speed streams can occur that do not lead to electron events. Therefore, it is assumed that high speed solar wind streams necessary but not sufficient to cause high energy electron events.

The GEO onset occurred before the LEO onset of each event. This may indicate that the electrons are entering geosynchronous altitudes near the magnetic equator then

progressing down to lower altitudes via the L-shells. This is quite possible for high speed streams to trigger a re-connection of the geosynchronous L-shells with the magnetotail. The electron density increases near the magnetic equator as the re-connection continues, but the particles can be accelerated via coulombic and wave-particle mechanisms [Hultqvist, 1999]. A change in pitch-angle may cause the electrons to mirror at much greater  $B/B_o$  values and reach lower altitudes. This “pitch-angle diffusion” is most effective with particles that mirror near the equator; this may be the case with energetic electron events entering from the magnetotail [Hultqvist, 1999].

### **Recommendations for Future Work**

This research began what should be continued in the future. The first step for continuing work would be to select a higher number of electron events that fit the isolated and non-proton contamination criteria. This allows for stronger correlations in differences of GEO to LEO onsets. The isolation criteria may be relaxed somewhat to allow for more initial electron events, especially during times of solar minimum. It may be possible to create a computer code to select isolated events; such automation could greatly reduce time and effort.

It is also formidable to integrate the irregular events into the final electron event progression. These events were originally disregarded but some of these events could provide more statistics toward the onset of an event at GEO and LEO. Only the onsets are desired, and, therefore, could be used for further analysis.

A higher time resolution of electron progression could be determined if the location uncertainty (say L-shell,  $B/B_o$ , and the magnetic local time) of each satellite was known. The functional relationship of electron flux versus these parameters must be

determined in order to decipher if changes in recorded electron count values are due to the actual electron event or if the recorded electron count values are actually reflections of drastic changes in time or location of the satellites [Onsager, et al, 2004, Miyoshi, et all, 2004]. It is paramount that the relationship of position, time, and dynamical changes in the electron count values are known in order to determine a better time resolution of the electron event progression.

## Appendix A: DSP-21 and TSX-5 CEASE Electron Event Plots and GOES-10 Proton Plots

This section shows the 25 isolated electron event data from DSP-21 (GEO) and TSX-5 (LEO). As described in Chapter III, the 25 events were subjected to certain criteria: basic concept theory and proton contamination. If the event did not fit the basic concept theory, it was disregarded from further analysis. If the event followed the aspects of a basic electron event, it was then compared to GOES-10 proton data.

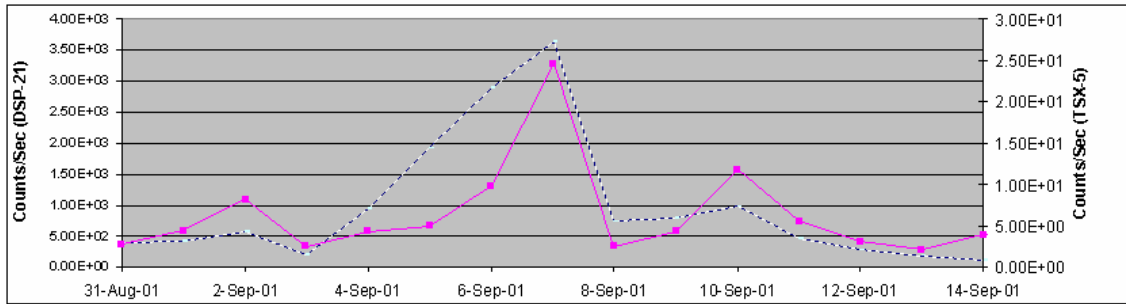


**Figure A1.** Electron Event #1 shows the characteristics of a basic electron event for both DSP-21 and TSX-5 data. This electron event was subjected to proton contamination.

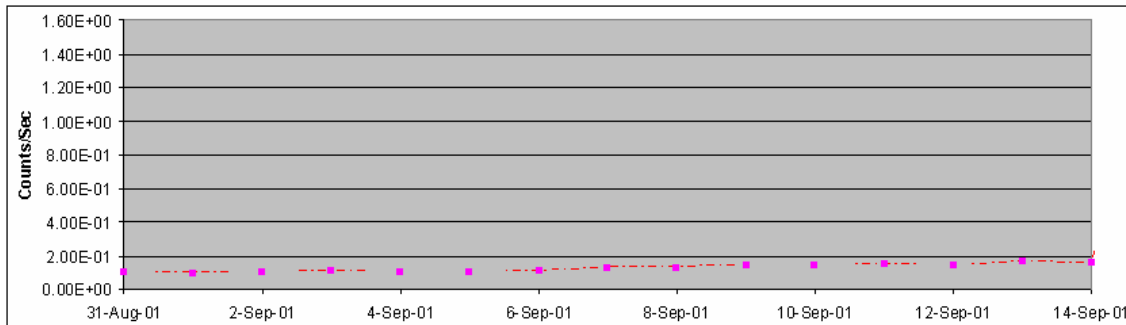


**Figure A2.** The GOES-10 proton data shows no significant increases in proton counts for the time period of Electron Event #1. Therefore, Electron Event #1 was subjected for further analysis.

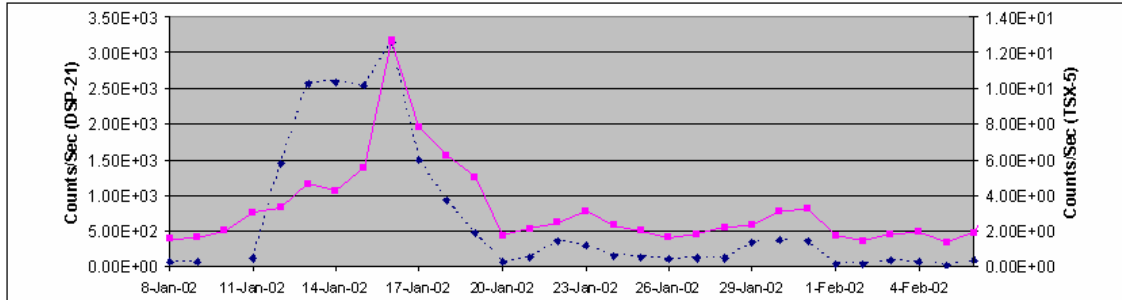


**Figure A3.** Electron Event #2 shows the characteristics of a basic electron event for both DSP-21 and TSX-5 data. This electron event was subjected to proton contamination.

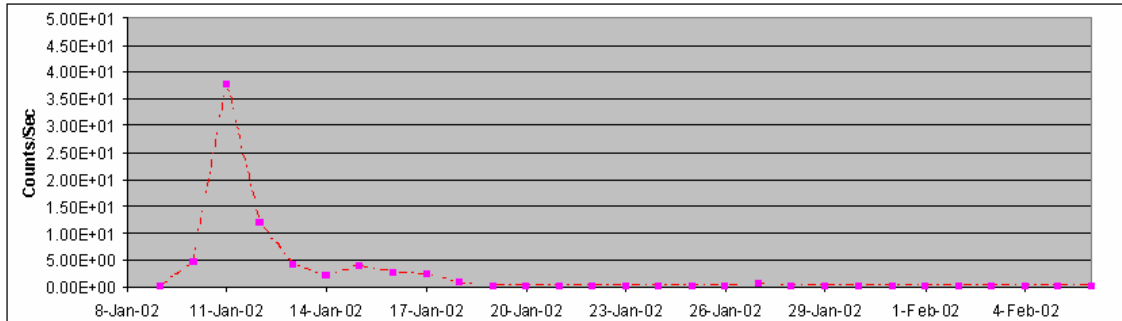


**Figure A4.** The GOES-10 proton data shows no significant increases in proton counts for the time period of Electron Event #2. Although there is a large spike in proton counts on 11 Jan 02, the DSP-21 and TSX-5 data do not show similar increases of the same levels on that day. Therefore, Electron Event #2 was subjected for further analysis.

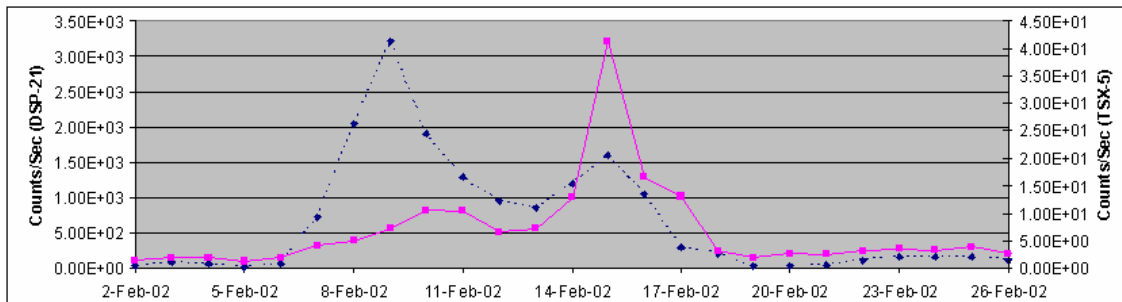


**Figure A5.** Electron Event #3 does not show the characteristics of a basic electron event for both DSP-21 and TSX-5 data. There are decreases in electron count values near 10 Feb 02 followed by significant increases. This event was determined to be an irregular event and was disregarded from further analysis.

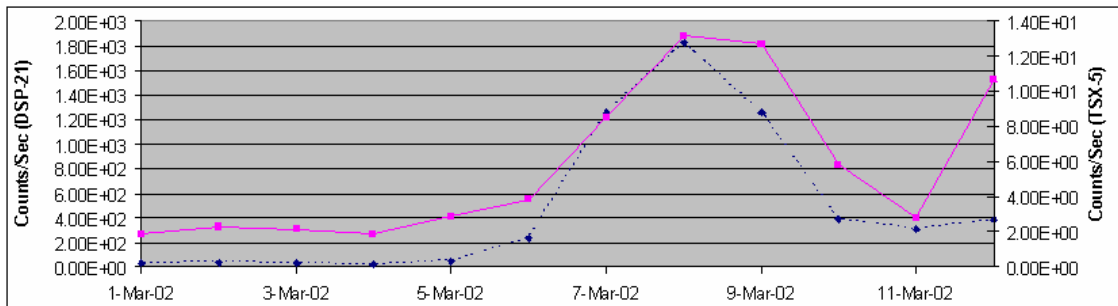


**Figure A6.** Electron Event #4 shows the characteristics of a basic electron event for both DSP-21 and TSX-5 data. This electron event was subjected to proton contamination.

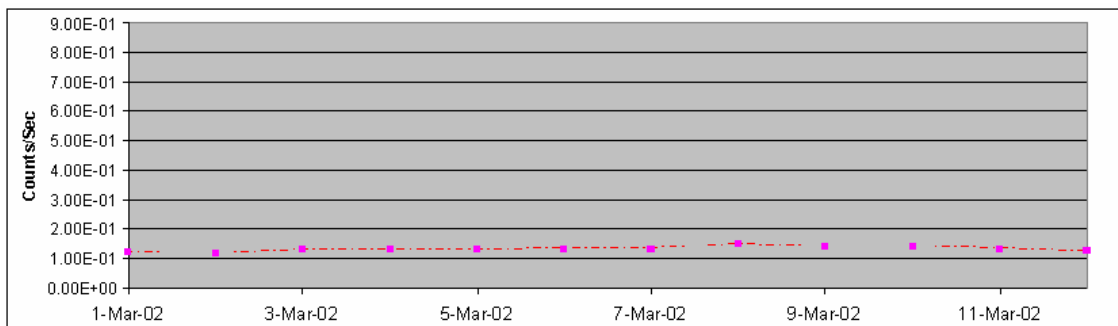


**Figure A7.** The GOES-10 proton data shows no significant increases in proton counts for the time period of Electron Event #4. Therefore, Electron Event #4 was subjected for further analysis.

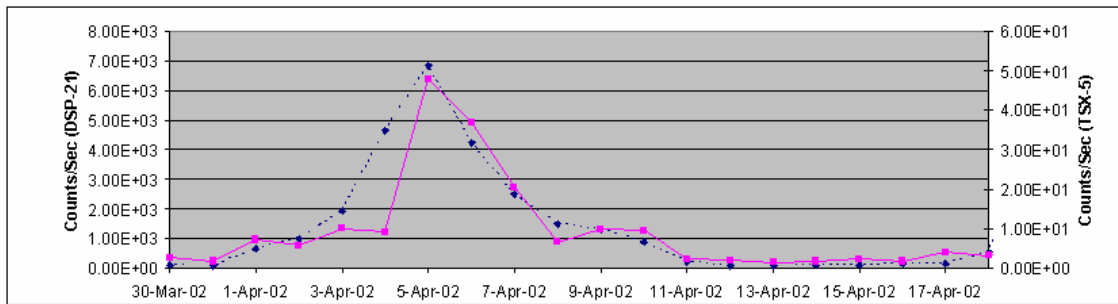


**Figure A8.** Electron Event #5 shows the characteristics of a basic electron event for both DSP-21 and TSX-5 data. This electron event was subjected to proton contamination.

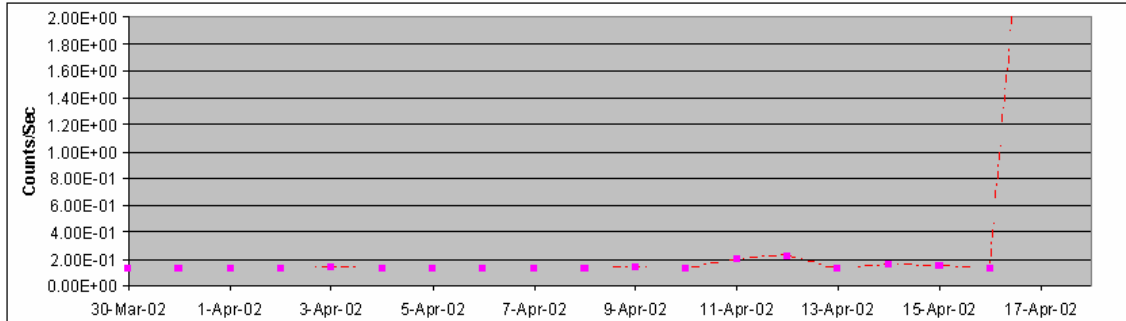


**Figure A9.** The GOES-10 proton data shows no significant increases in proton counts for the time period of Electron Event #5. Although a significant increase is apparent on 16 Apr 02, this increase in proton counts is well after Electron Event #5. Therefore, Electron Event #5 was subjected for further analysis.

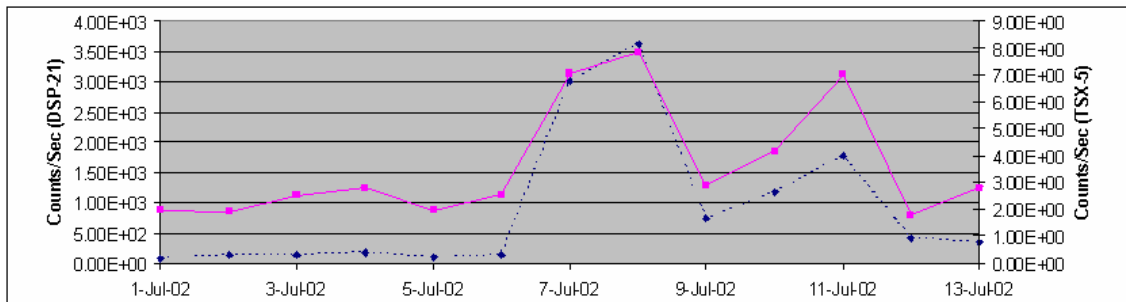


**Figure A10.** Electron Event #6 shows the characteristics of a basic electron event for both DSP-21 and TSX-5 data. This electron event was subjected to proton contamination.

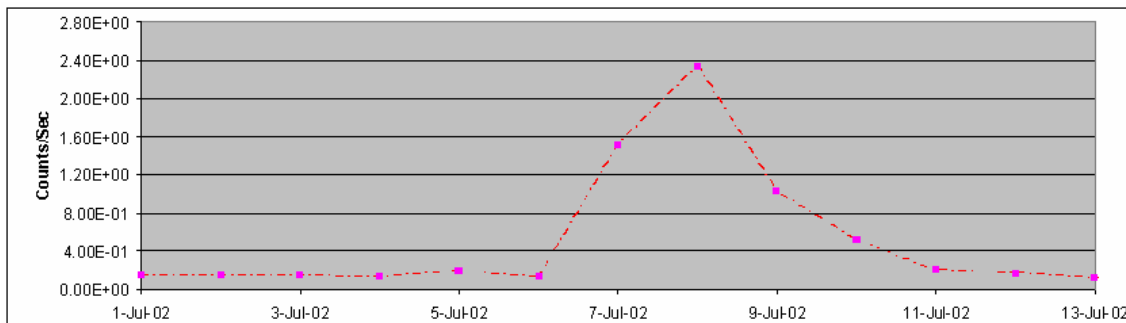


**Figure A11.** The GOES-10 proton data shows no significant increases in proton counts for the time period of Electron Event #6. A significant increase is apparent starting on 6 Jul 02 and the DSP-21 and TSX-5 data both show electron count increases on the same date. There is a high probability that the GEO and LEO data for Electron Event #6 is contaminated by protons. Therefore, this event was disregarded from further analysis.

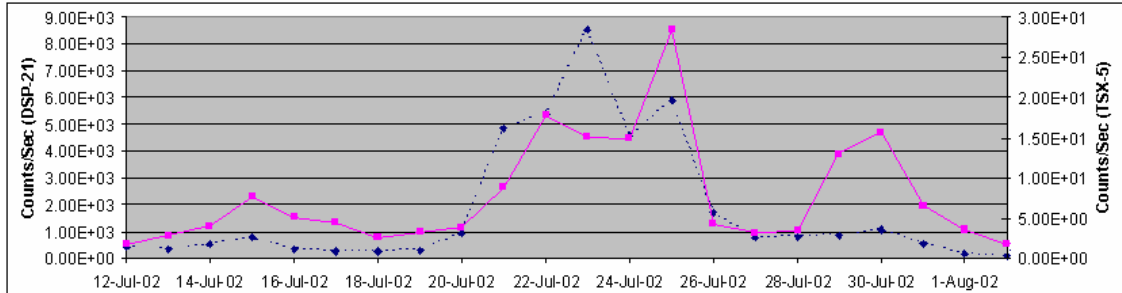


**Figure A12.** Electron Event #7 does not show the characteristics of a basic electron event for both DSP-21 and TSX-5 data. There are decreases in electron count values near 24 Jul 02 for the DSP-21 data followed by a significant increase. The TSX-5 data shows a decrease in electron count values on 22 Jul 02 followed by a very large increase in electron counts on 25 Jul 02. This event was determined to be an irregular event and was disregarded from further analysis.

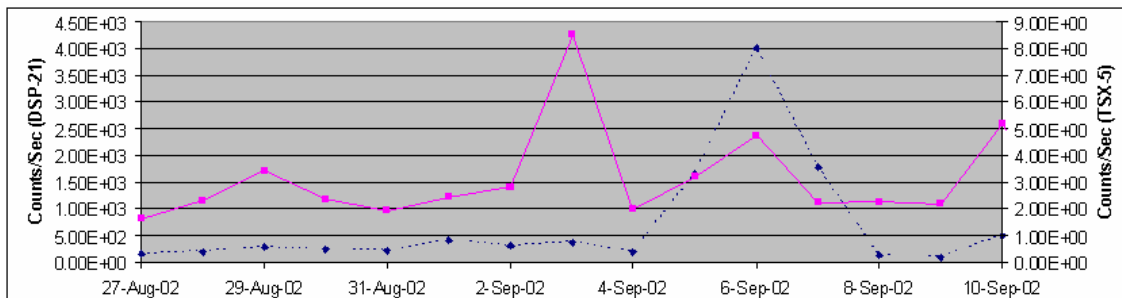


**Figure A13.** Electron Event #8 does not show the characteristics of a basic electron event for the TSX-5 data. There is a significant decrease in electron count values on 4 Sep 02 followed by a large increase the next day. This event was determined to be an irregular event and was disregarded from further analysis.

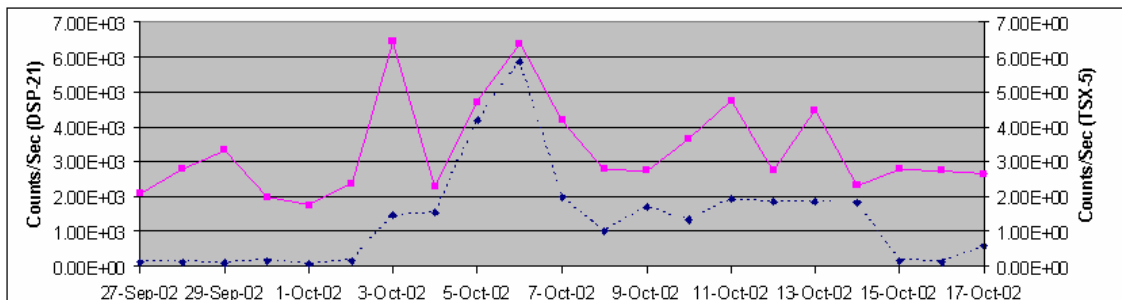


**Figure A14.** Electron Event #9 does not show the characteristics of a basic electron event for the TSX-5 data. There are many significant increases and decreases in electron count values starting on 5 Oct 02. This event was determined to be a very irregular event and was disregarded from further analysis.

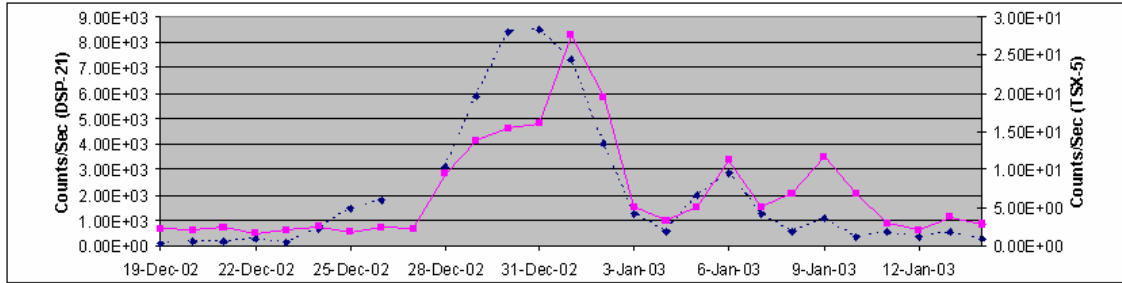


**Figure A15.** Electron Event #10 shows the characteristics of a basic electron event for both DSP-21 and TSX-5 data. This electron event was subjected to proton contamination.

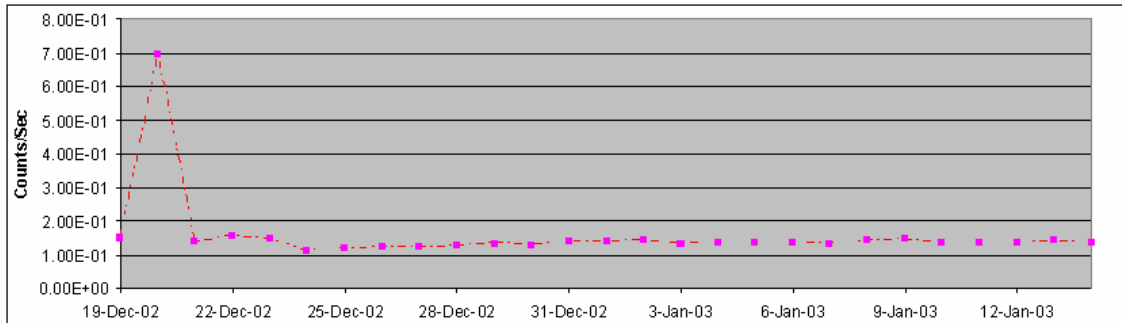


**Figure A16.** The GOES-10 proton data shows no significant increases in proton counts for the time period of Electron Event #10. Although there is a large spike in proton counts on 19 Dec 02, it appears to occur well before the electron event and does not seem to be a factor in proton contamination. Therefore, Electron Event #10 was subjected for further analysis.

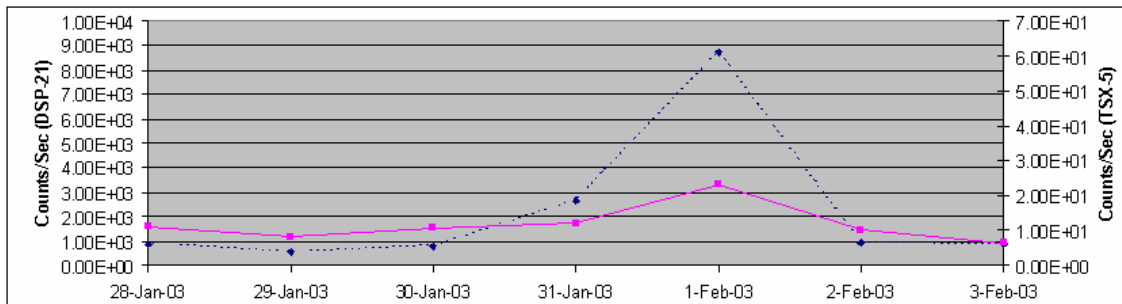


**Figure A17.** Electron Event #11 shows the characteristics of a basic electron event for both DSP-21 and TSX-5 data. This electron event was subjected to proton contamination.

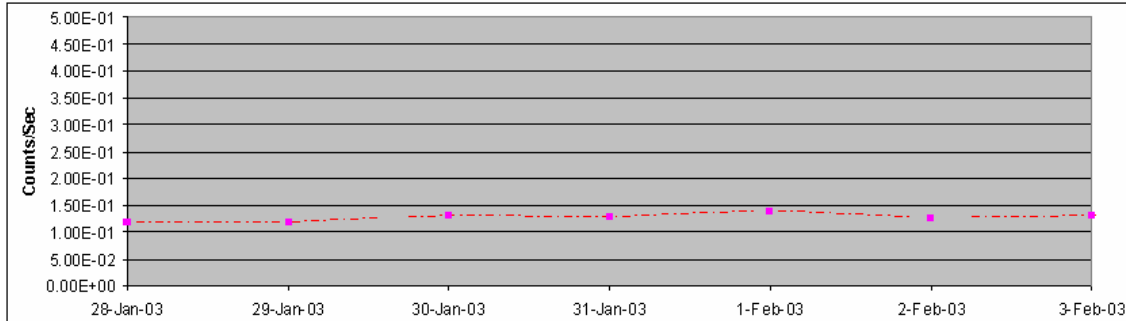


**Figure A18.** The GOES-10 proton data shows no significant increases in proton counts for the time period of Electron Event #11. Therefore, Electron Event #10 was subjected for further analysis.

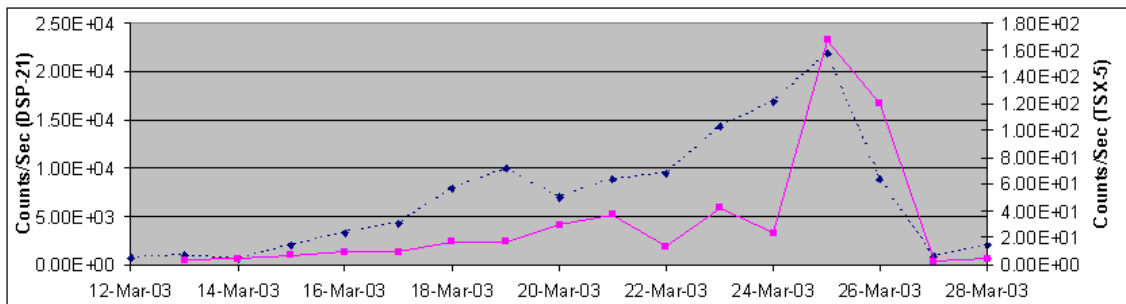


**Figure A19.** Electron Event #12 does not show the characteristics of a basic electron event for the DSP-21 and TSX-5 data. There is a significant decrease in electron count values starting on 19 Mar 03 for the DSP-21 data and several increases and decreases in the TSX-5 data starting on 22 Mar 03. Electron Event #12 was determined to be an irregular event and was disregarded from further analysis.

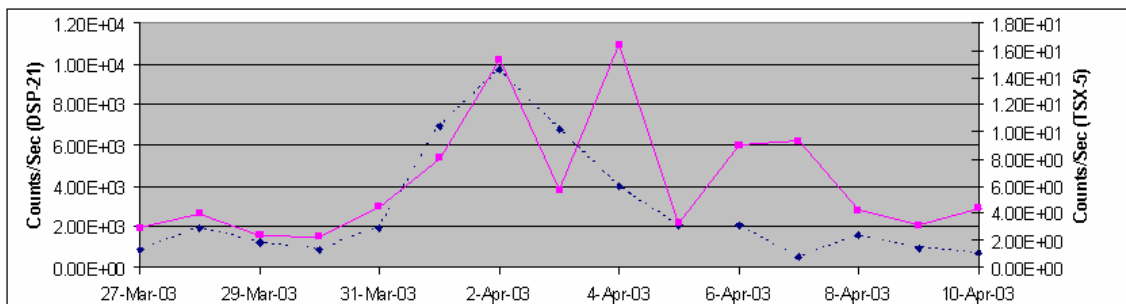


**Figure A20.** Electron Event #13 does not show the characteristics of a basic electron event for the TSX-5 data. There is a significant decrease in electron count values on 3 Apr 03 followed by an increase on 4 Apr 03 only to significantly decrease again the next day. This event exhibits the characteristics of an irregular event and was disregarded from further analysis.

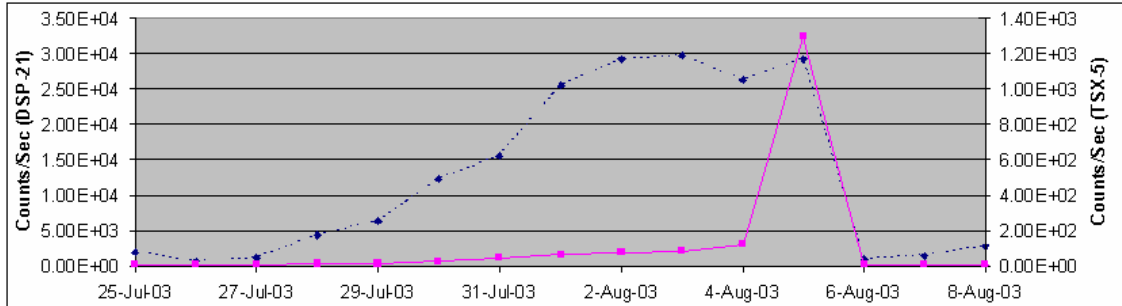


**Figure A21.** Electron Event #14 shows the characteristics of a basic electron event for both DSP-21 and TSX-5 data. This electron event was subjected to proton contamination.

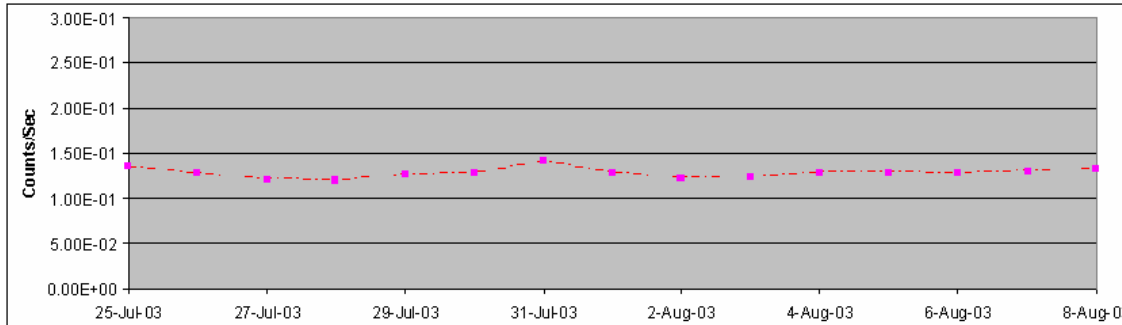


**Figure A22.** The GOES-10 proton data shows no significant increases in proton counts for the time period of Electron Event #14. Therefore, Electron Event #14 was subjected to further analysis.

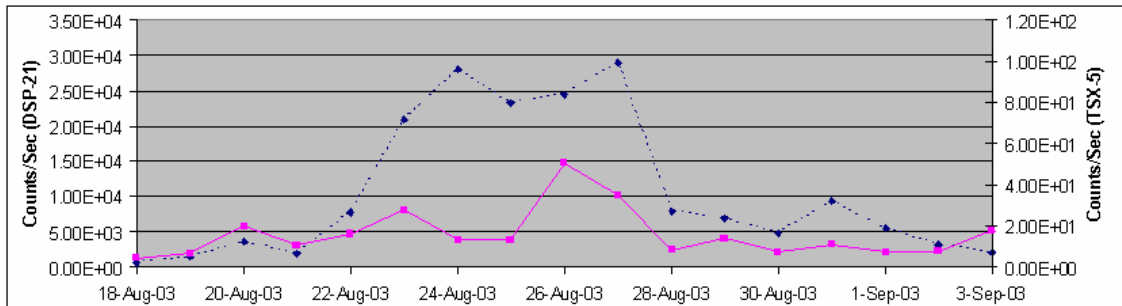


**Figure A23.** Electron Event #15 does not show the characteristics of a basic electron event. There are significant decreases in electron count values on 24 Aug 03 for the DSP-21 data and the previous day for the TSX-5 data. Each orbit shows increases in electron count values a few days later. Electron Event #15 was deemed an irregular event and was disregarded from further analysis.

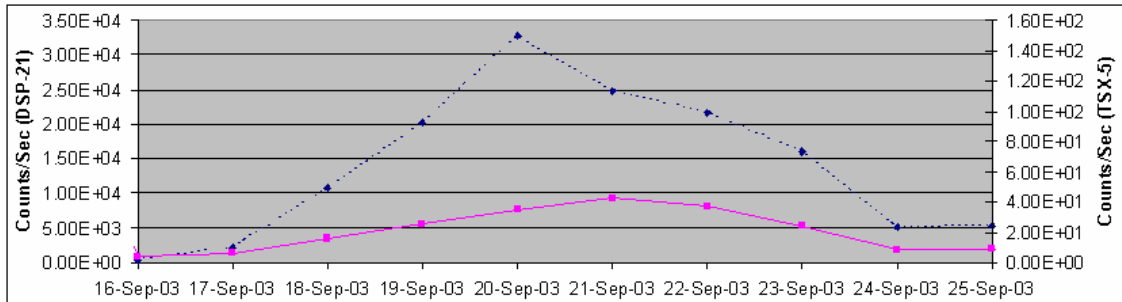


**Figure A24.** Electron Event #16 shows the characteristics of a basic electron event for both DSP-21 and TSX-5 data. This electron event was subjected to proton contamination.

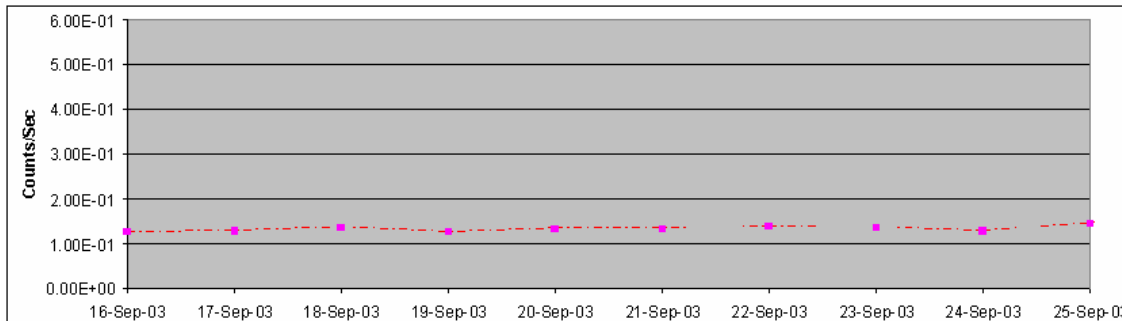


**Figure A25.** The GOES-10 proton data shows no significant increases in proton counts for the time period of Electron Event #16. Therefore, Electron Event #16 was subjected to further analysis.

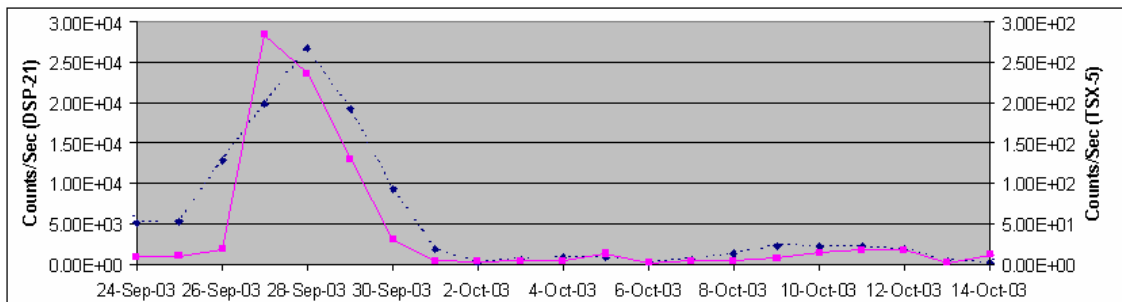


**Figure A26.** Electron Event #17 shows the characteristics of a basic electron event for both DSP-21 and TSX-5 data. This electron event was subjected to proton contamination.

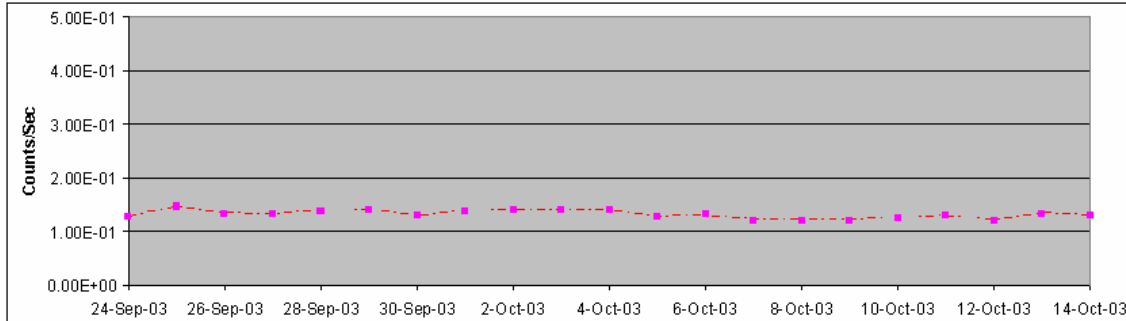


**Figure A27.** The GOES-10 proton data shows no significant increases in proton counts for the time period of Electron Event #17. Therefore, Electron Event #17 was subjected to further analysis.

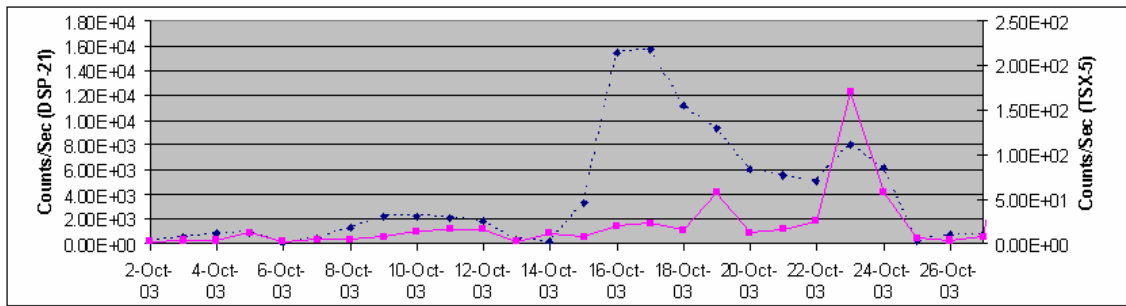


**Figure A28.** Electron Event #18 does not show the characteristics of a basic electron event. There are significant decreases in electron count values beginning on 17 Oct 03 for the DSP-21 data and on 19 Oct 03 for the TSX-5 data. Electron Event #18 was deemed an irregular event and was disregarded from further analysis.

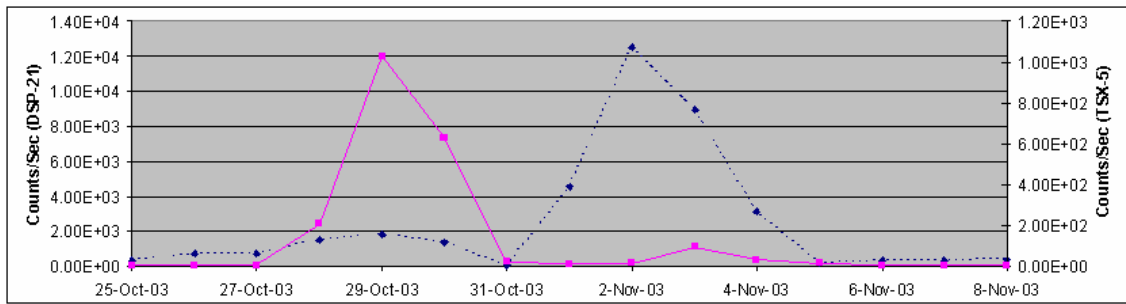


**Figure A29.** Electron Event #19 does not show the characteristics of a basic electron event. Although the plots shows monotonic increases for the GEO and LEO orbits, the fact that the LEO electron counts shows a large peak in electron counts on 29 Oct 03 when the GEO data shows a relatively small electron count peak. However, near 2 Nov 03, the orbital electron counts appear to reverse; DSP-21 data shows a larger electron count value than the previous peak date and TSX-5 shows a much smaller electron peak value than 29 Oct 03. This event was determined to be an irregular event and was stricken from further analysis.

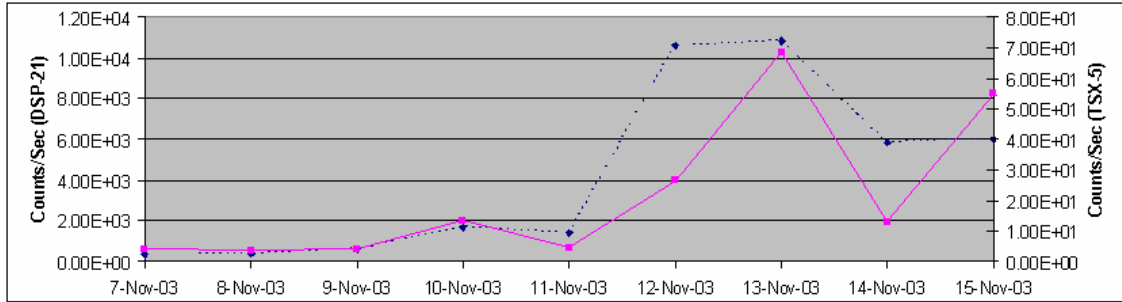


**Figure A30.** Electron Event #20 does not show the characteristics of a basic electron event. The TSX-5 data shows a large increase on 14 Oct 03 after a significant electron count decrease. Electron Event #20 was determined to be an irregular event and was not subjected for further analysis.

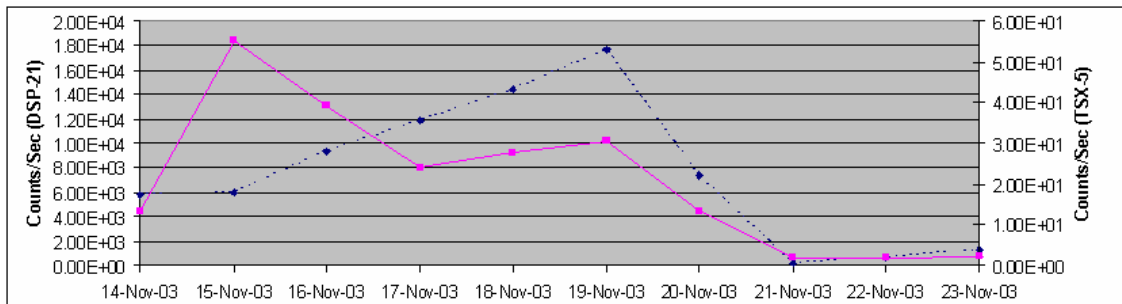


**Figure A31.** Electron Event #21 does not show the characteristics of a basic electron event. The TSX-5 data shows a large decrease of electron counts on 15 Nov 03 followed by an increase on 17 Nov 03. Electron Event #21 was determined to be an irregular event and was not subjected for further analysis.

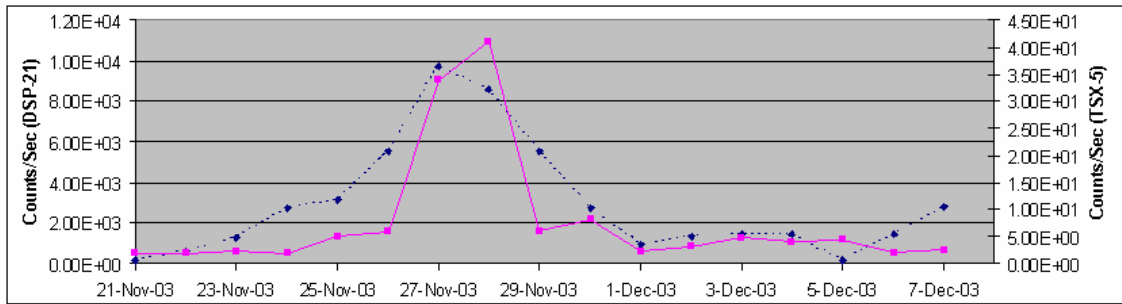


**Figure A32.** Electron Event #22 shows the characteristics of a basic electron event for both DSP-21 and TSX-5 data. This electron event was subjected to proton contamination.

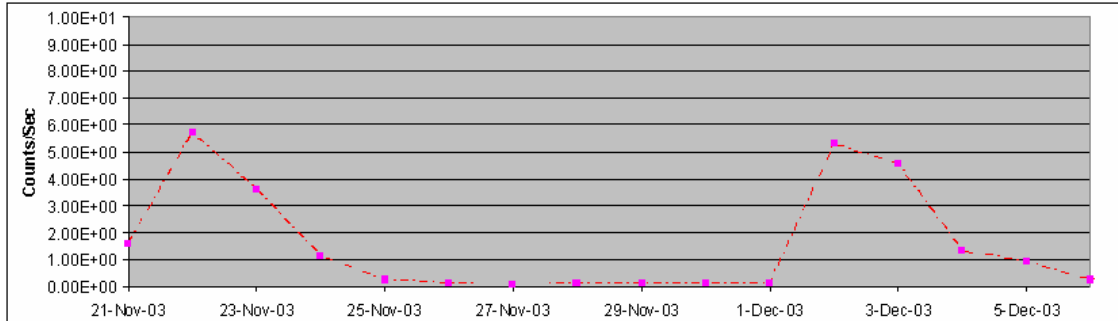


**Figure A33.** The GOES-10 proton data shows no significant increases in proton counts during the time period of Electron Event #22. There exists several spikes in proton counts, but these proton count peak occur before and after the isolated electron event. Therefore, Electron Event #22 was subjected to further analysis.

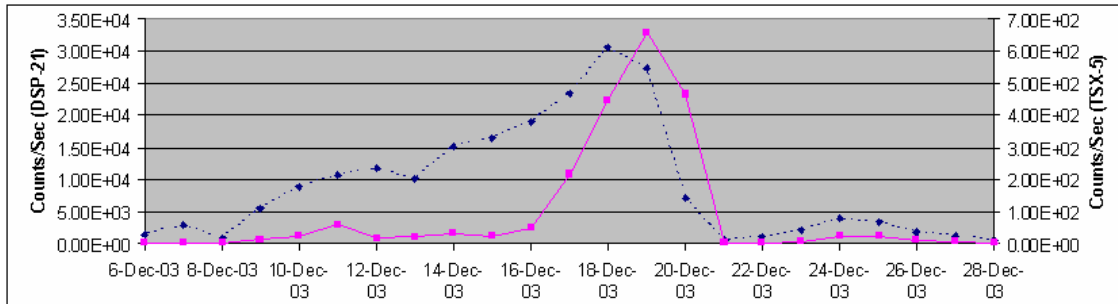


**Figure A34.** Electron Event #23 shows the characteristics of a basic electron event for both DSP-21 and TSX-5 data. This electron event was subjected to proton contamination.

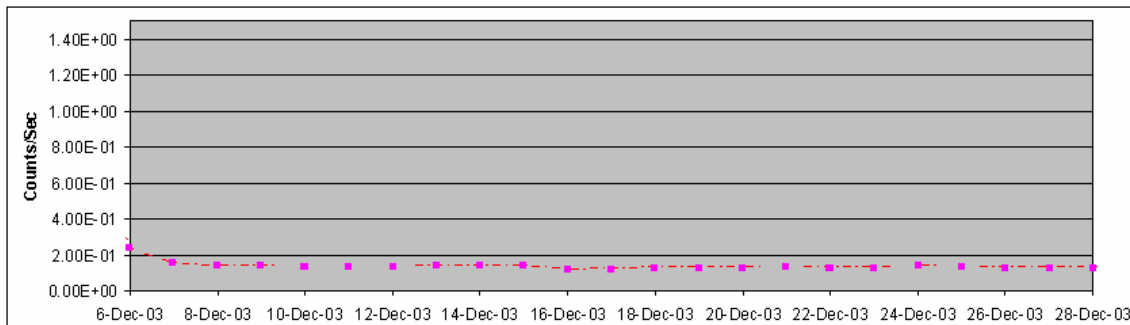


**Figure A35.** The GOES-10 proton data shows no significant increases in proton counts during the time period of Electron Event #23. Electron Event #23 was subjected to further analysis.

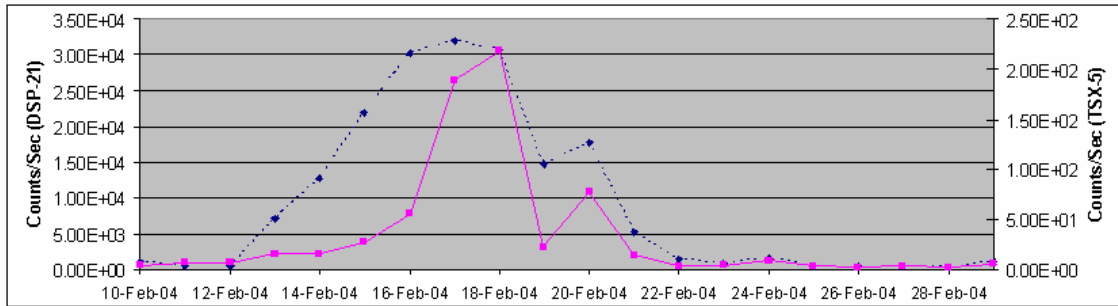


**Figure A36.** Electron Event #24 shows the characteristics of a basic electron event for both DSP-21 and TSX-5 data. This electron event was subjected to proton contamination.

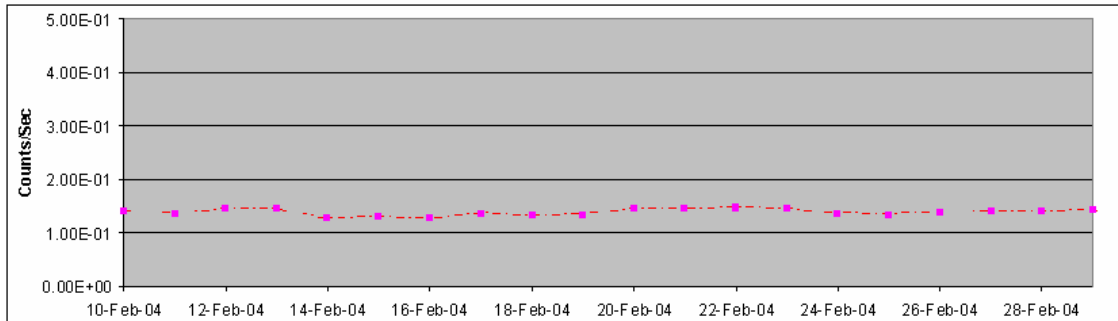


**Figure A37.** The GOES-10 proton data shows no significant increases in proton counts during the time period of Electron Event #24. Therefore, Electron Event #24 was subjected to further analysis.

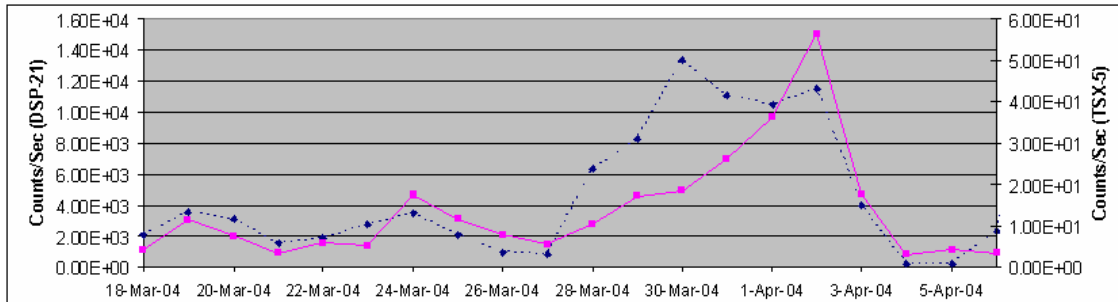


**Figure A38.** Electron Event #25 does not show the characteristics of a basic electron event. The TSX-5 data shows a significant decrease of electron counts on 24 Mar 04 followed by an increase on 27 Mar 04. The DSP-21 data shows a decrease on 30 Mar 04 with an increase on 2 Apr 04. This was determined to be an irregular event and was not subjected for further analysis.

## Appendix B: TSX-5 CEASE Data Hemisphere Separation and GEO and LEO Onsets

This section gives the plots of the electron count values when the TSX-5 apogee was located near the high latitude limits of the TSX-5 orbit along with the DSP-21 electron counts. Each plot is on a 24-hour time resolution. This section also includes the GEO and LEO thresholds for each event; the calculation and results of the thresholds are evident in tables below the electron event plots.

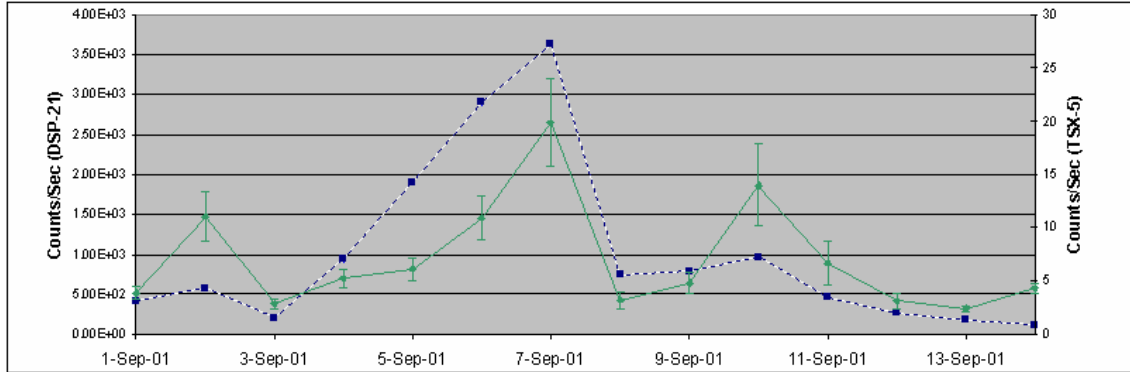


**Figure B1. Plot of DSP-21 and TSX-5 electron count values for Event #1. The TSX-5 data represents the hemisphere that holds the TSX-5 apogee near the high latitude limits of the orbit. The error bars represent the standard error for the electron count values for each day.**

**Table B1. The time periods for the GEO threshold and calculations are shown for Event #1. This table also includes the LEO threshold day for the same event.**

GEO Threshold (Counts/Sec)		LEO Threshold	
DSP-21 CEASE Data			
Time Period	19 Oct 01-29 Oct 01		
Average Count/Sec	1.67E+02		
Standard Error	1.86E+01		
GEO Threshold	2.04E+02		
GEO Onset	3-Sep-01	LEO Onset	5-Sep-01

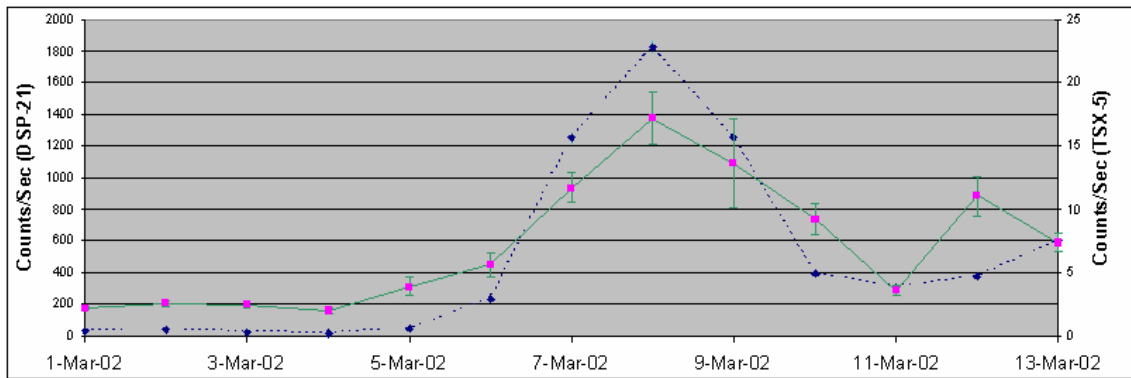


**Figure B2. Plot of DSP-21 and TSX-5 electron count values for Event #4. The TSX-5 data represents the hemisphere that holds the TSX-5 apogee near the high latitude limits of the orbit. The error bars represent the standard error for the electron count values for each day.**

**Table B2. The time periods for the GEO threshold and calculations are shown for Event #4. This table also includes the LEO threshold day for the same event.**

GEO Threshold (Counts/Sec)		LEO Threshold	
DSP-21 CEASE Data			
Time Period	19 Feb 02-5 Mar 02		
Average Count/Sec	8.32E+01		
Standard Error	1.40E+01		
GEO Threshold	2.88E+02		
GEO Onset	5-Mar-02	LEO Onset	6-Mar-02

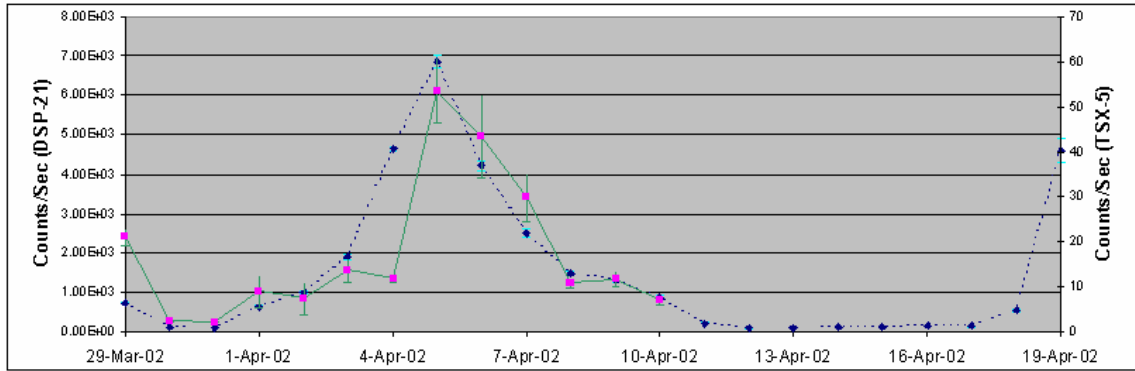


**Figure B3. Plot of DSP-21 and TSX-5 electron count values for Event #5. The TSX-5 data represents the hemisphere that holds the TSX-5 apogee near the high latitude limits of the orbit. The error bars represent the standard error for the electron count values for each day.**

**Table B3. The time periods for the GEO threshold and calculations are shown for Event #5. This table also includes the LEO threshold day for the same event.**

GEO Threshold (Counts/Sec)		LEO Threshold	
DSP-21 CEASE Data			
Time Period	19 Feb 02-5 Mar 02		
Average Count/Sec	8.32E+01		
Standard Error	1.40E+01		
GEO Threshold	1.11E+02		
GEO Onset	31-Mar-02	LEO Onset	4-Mar-02

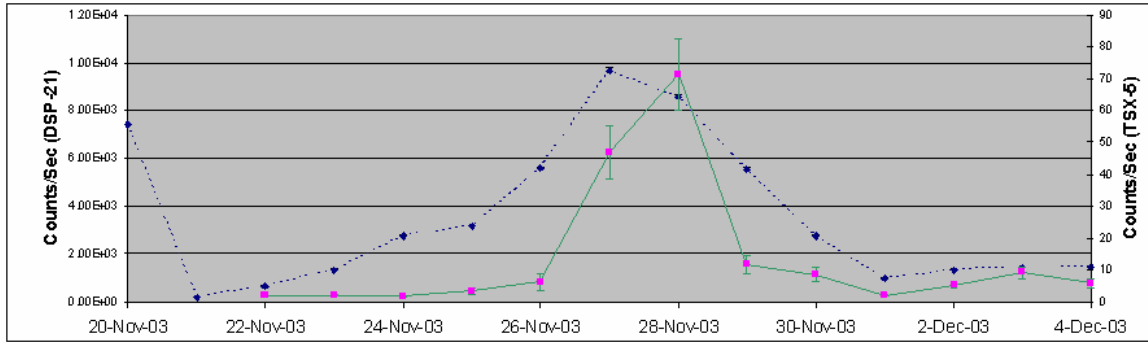


**Figure B4.** Plot of DSP-21 and TSX-5 electron count values for Event #22. The TSX-5 data represents the hemisphere that holds the TSX-5 apogee near the high latitude limits of the orbit. The error bars represent the standard error for the electron count values for each day.

**Table B4.** The time periods for the GEO threshold and calculations are shown for Event #22. This table also includes the LEO threshold day for the same event.

GEO Threshold (Counts/Sec)		LEO Threshold	
DSP-21 CEASE Data			
Time Period	23 Feb 04-29 Feb 04		
Average Count/Sec	7.20E+02		
Standard Error	1.05E+02		
GEO Threshold	9.30E+02		
GEO Onset	22-Nov-04	LEO Onset	26-Nov-04

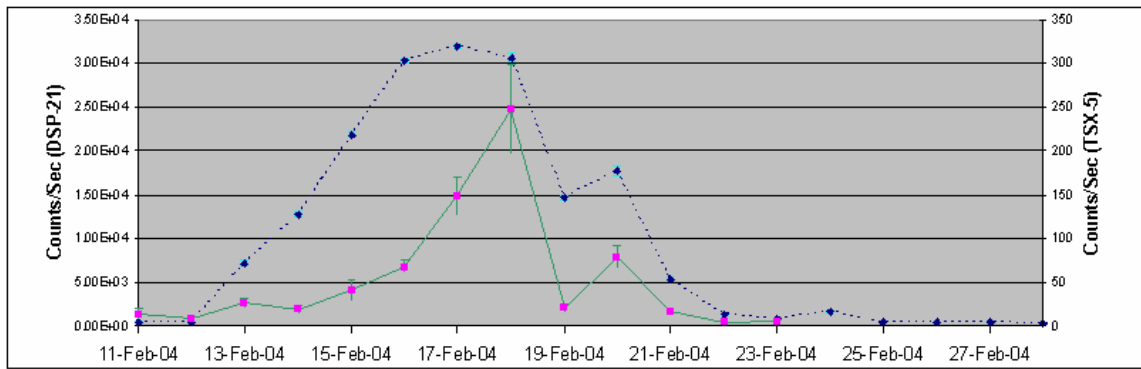


**Figure B5.** Plot of DSP-21 and TSX-5 electron count values for Event #24. The TSX-5 data represents the hemisphere that holds the TSX-5 apogee near the high latitude limits of the orbit. The error bars represent the standard error for the electron count values for each day.

**Table B5.** The time periods for the GEO threshold and calculations are shown for Event #24. This table also includes the LEO threshold day for the same event.

GEO Threshold (Counts/Sec)			LEO Threshold		
DSP-21 CEASE Data					
Time Period	23 Feb 04-29 Feb 04				
Average Count/Sec	7.20E+02				
Standard Error	1.05E+02				
GEO Threshold	9.30E+02				
GEO Onset	12-Feb-04		LEO Onset	14-Feb-04	

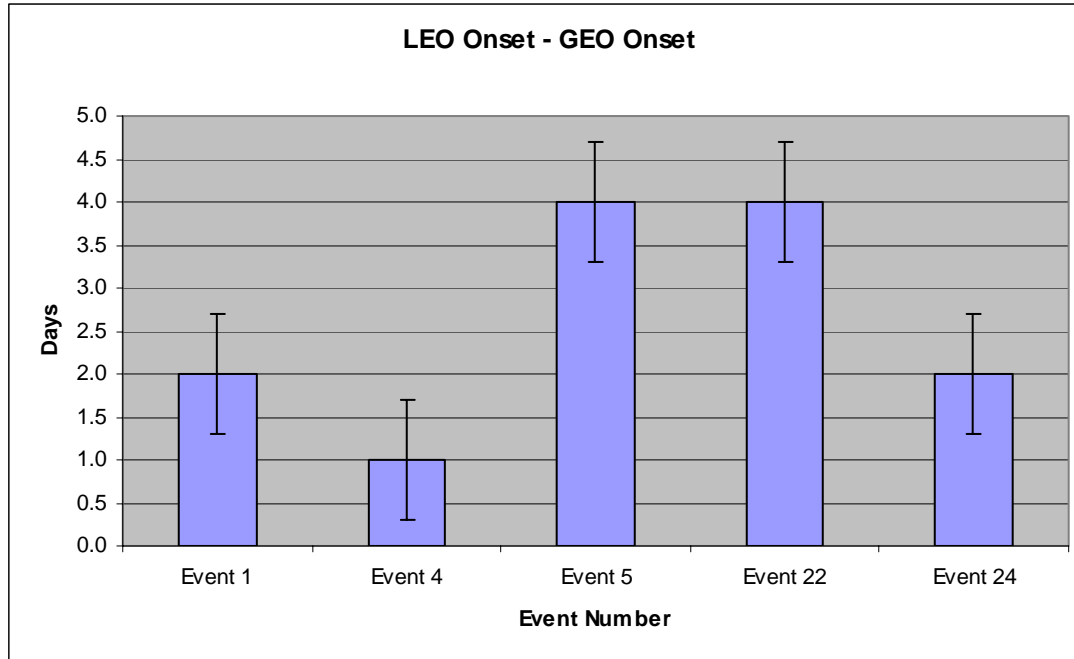
## Appendix C: Electron Event Progression

This section presents the electron event progression from GEO to LEO. The table below shows the results of each event progression and the uncertainty.

**Table C1. Progression times of electron events. The uncertainty is the same for each event due to the methods and techniques used in the electron event onset determination.**

Event	LEO Onset-GEO Onset	Error
Event 1	2.0	0.71
Event 4	1.0	0.71
Event 5	4.0	0.71
Event 22	4.0	0.71
Event 24	2.0	0.71

**Figure C1. A graphed version the progression times of each electron event from GEO to LEO.**



## **Appendix D: Space Environment Center Weekly Reports**

This section presents the Space Environment Center Weekly Reports comparison to each electron event. By the timeframe of the electron events, segments were extracted from the weekly reports from the Space Environment Center's website. Periods associated in time with electron count increases for the electron events are highlighted.

### **Event #1:**

**03 September - 09 September 2001** Solar Wind data were available from the Advanced Composition Explorer (ACE) spacecraft for most of the period. A high-speed stream associated with a coronal hole was observed during 03 - 04 September. Velocities peaked at around 570 km/sec late on 03 September into the early hours of 04 September, then gradually decreased. There were no significant disturbances observed during the remainder of the period.

### **Event #2:**

**07 - 13 January 2002** Solar wind data were available from the NASA Advanced Composition Explorer (ACE) spacecraft for most of the period. A high-speed stream associated with a coronal hole was observed during 10 – 13 January. Solar wind velocities peaked early on 11 January with “gusts” as high as 700 km/sec, then gradually decreased. There were no significant disturbances observed during the rest of the period.

### **Event #4:**

**04 - 10 March 2002** Solar wind data were available from NASA Advanced Composition Explorer (ACE) spacecraft for most of the summary period. A high-speed solar wind stream was observed during 04 – 07 March. This stream was likely associated with a recurrent positive-polarity coronal hole. Solar wind velocities gradually increased during 04 - 05 March and reached a peak wind speed of around 740 km/sec early on 05 March. The high-speed stream subsided early on 08 March. There were some periods of sustained southward IMF Bz detected on 10 March (roughly 10/0900 – 1300 UTC) with peak southward deflections to minus 06 nT (GSM).

### **Event #5:**

**01 - 07 April 2002** Solar wind data were available from NASA Advanced Composition Explorer (ACE) spacecraft for most of the summary period. A recurrent high-speed stream was in progress as the period began, then subsided early on 04 April. The source for this high-speed stream was a recurrent coronal hole. Solar wind velocities were elevated during 30 March – (early) 04 April. The highest velocities occurred during 31 March – 01 April with “gusts” in the 750 to 830 km/sec range. Another (weak) high-speed

stream, also due to a coronal hole, commenced on 07 April associated with a relatively minor increase in velocities (peaks to 470 km/sec).

### **Event #10:**

**23 - 29 December 2002** Solar wind data were available from the NASA Advanced Composition Explorer (ACE) spacecraft for most of the summary period. Solar wind velocity was elevated for much of the period, due to transient effects and a recurrent coronal hole. A six-hour period of sustained southward Bz values, and solar wind velocities near 600 km/s, were observed on 23 December. A transient shock passage occurred at approximately 1300 UTC on 24 December, in likely association with an M-class event and CME, which was observed three days earlier. In response to a recurrent coronal hole, solar wind velocity began to increase late on 26 December and reached a peak value near 750 km/s on 28 December.

### **Event #11:**

**26 January - 02 February 2003** Solar wind data were available from the NASA Advanced Composition Explorer (ACE) spacecraft for most of the summary period. The period began in a diminishing high-speed coronal hole stream. Solar wind speed was elevated between 500 – 600 km/s early, but had declined to more nominal speeds of 400 – 450 km/s by the 28th. Occasional sustained periods of southward Bz in the interplanetary magnetic field occurred on the 28-29th. Solar wind speed increased on the 30th with the onset of another coronal hole. Speed gradually increased to over 600 km/s on the 31st before the effects of the coronal hole started to wane. A dramatic increase in solar wind speed to over 800 km/s was observed to begin at around 1300 UTC on the 1st as the CME observed on 30 January impacted the ACE spacecraft. A marked increase in density, temperature and total magnetic field also occurred with this transient passage. The Bz component of the interplanetary magnetic field was initially northward as the CME passed ACE, but periods of southward Bz were observed late on the 1st through the 2nd. Speed had returned to near 450 km/s by the end of the period.

### **Event #14:**

**21 - 27 July 2003** A waning high speed solar wind stream was in effect early in the period. Speeds near 600 km/s declined to 450 km/s by late on the 21st. Near nominal solar wind conditions persisted through the 22nd. A weak transient impact was observed at ACE on the 23rd; solar wind speed increased to over 500 km/s and periods of sustained southward Bz occurred. Solar wind speed gradually declined to very low levels just above 300 km/s by the 25th. A strong co-rotating interaction region (CIR) on 26 July, heralded the onset of a large recurrent southern coronal hole stream. Total field measurements in the CIR were over 35 nT, and the Bz component experienced sustained southward periods near -30 nT. The solar wind speed

associated with this high speed stream was approximately 800 km/s, and generally ranged between 550 - 800 km/s for the remainder of the period.

#### **28 July - 03 August 2003**

Solar wind data were available from the NASA Advanced Composition Explorer (ACE) spacecraft for most of the summary period. A large coronal hole high speed stream began on 28 July and dominated the period. Solar wind speeds increased late on the 28th and were elevated near 750 - 900 km/s for most of the period. Wind speed began a steady decline late on 01 August and reached 550 km/s at the close of the period. The Bz component of the interplanetary magnetic field oscillated between +/- 10 nT early in the period but was between +/- 6 nT for most of the period.

#### **Event #16:**

**15 - 21 September 2003** Solar wind data were available from the NASA Advanced Composition Explorer (ACE) spacecraft for most of the summary period. Early on 16 September a slow transient was observed passing the ACE spacecraft. Total IMF measurements (Bt) reached 12 nT and Bz values were -5 to -10 nT. By late on 16 September, a large coronal hole high speed stream rotated into a geoeffective position with solar wind speeds increasing from 450 to over 800 km/s by 17 September. The Bz component of the IMF reached -10 to -15 nT at the onset of the coronal hole and from 18 – 21 September Bz was oscillating between +/- 7 nT. Solar wind speed was near 800 km/s on 18 September before beginning a slow decline. By the close of the period solar wind speed was down to 550 km/s.

#### **Event #17:**

**22 - 28 September 2003** Solar wind data were available from the NASA Advanced Composition Explorer (ACE) spacecraft for most of the summary period. The period began with solar wind speed near 600 km/s due to a coronal hole high speed flow. On 23 September, the high speed flow was in decline as yet another coronal hole high speed flow rotated into a geoeffective position. Wind speed increased on 24 September and reached a peak near 775 km/s on 25 September. The second high speed flow was in steady decline from 26-28 September and solar wind speed at the close of the period was near 375 km/s. The Bz component of the interplanetary magnetic field fluctuated mostly between +/- 6 nT during the two high speed flows. Peak fluctuations reached -9 nT on 24 September.

#### **Event #22:**

**17 – 23 November 2003** Solar wind data were available from the NASA Advanced Composition Explorer (ACE) spacecraft during most of the summary period. A coronal hole high speed stream was in progress at the beginning of the period with wind speed near 825 km/s. On 19 November, wind speed dropped off to around 450 km/s as the coronal hole rotated beyond a geoeffective position. A shock from the CME on 18 November was observed passing the L1 point at 0740 UTC on 20 November. The MTOF/PM

instrument on the SOHO spacecraft recorded a 350 km/s increase in solar wind speed to over 800 km/s. The NASA/ACE satellite data were not available during the shock however, post shock data indicated total IMF measured close to 60 nT and the Bz component decreased to around -60 nT. Towards the end of the period, 22 –23 November, a second coronal hole high speed stream rotated into a geoeffective position producing elevated solar wind speed at around 575 km/s.

### **Event #23:**

**08 - 14 December 2003** Solar wind data were available from the NASA Advanced Composition Explorer (ACE) spacecraft during most of the summary period. Early on 08 December, solar wind speeds increased to nearly 650 km/sec in response to a large, recurrent, mid-disk coronal hole. The Bz component of the IMF, after an initial northward direction, turned southward, and then began a north-south oscillation. This signature was consistent to that of a co-rotating interactive region that normally precedes the onset of a high-speed stream. Solar wind speeds remained steady at 650 to 700 km/sec until midway on the 10th when speeds further increased to 850 km/sec as the large coronal hole moved into a more favorable position. Solar wind speed dropped back in the range of 700 – 800 km/s on 12 December and remained there through the end of the period on 14 December.

**15 – 21 December 2003** Solar wind data were available from the NASA Advanced Composition Explorer (ACE) spacecraft during most of the summary period. Solar wind speeds were near 800 km/s at the beginning of the period due to a large trans equatorial coronal hole. On 16 December, as the coronal hole rotated beyond a geoeffective position, wind speed began a steady decline to near 325 km/s by 19 December. Another, smaller elongated coronal hole rotated into a geoeffective position on 20 – 21 December with wind speeds reaching 625 km/s; however, Bz remained predominantly northward.

### **Event #24:**

**09 – 16 February 2004** Solar wind data were available from the NASA Advanced Composition Explorer (ACE) spacecraft during most of the summary period. Late on 11 February, IMF total field increased to 15 nT and Bz decreased to -12 nT marking the beginning of a co-rotating interaction region (CIR). The CIR gave way to a coronal hole high speed stream on 12 February as solar wind speed increased to near 700 km/s. Solar wind decreased to near 630 km/s and remained there through 14 February. An increase in wind speed to near 800 km/s was observed on 15 February, before a steady decline began. The period ended with solar wind speed at 600 km/s and decreasing.

## Appendix E: Two-Month Quiet Period Comparison with SEC Weekly Reports

This section shows the correlation of the 2-Month Quiet Time period from 27 Nov 01 through 5 Feb 02.

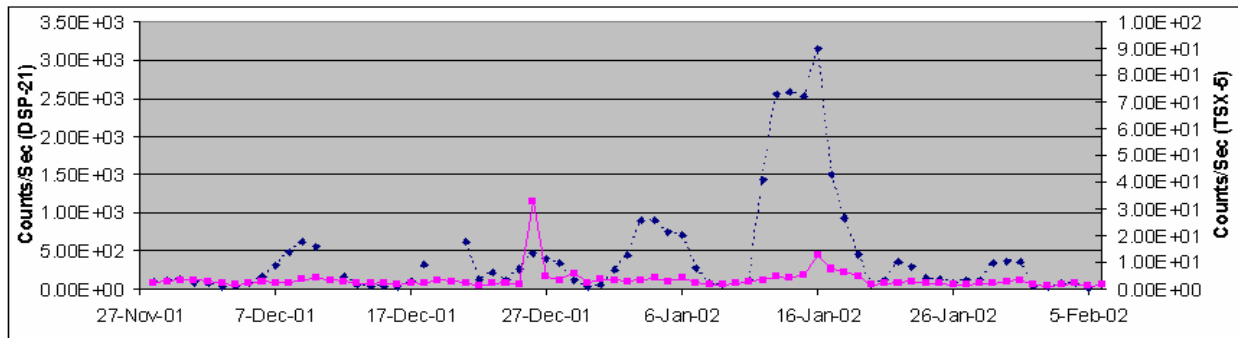


**Figure E1. The 2-Month Quiet Time Period shows relatively little particle activity with one exception: 12-20 Jan 02. This time period refers to an isolated Electron Event #2. Smaller increases in electron counts to appear in this period but are relatively small compared to the isolated electron events.**

### SEC Weekly Reports for Two-Month Period:

**26 November - 02 December 2001** Wind speeds were high (peaks to 800 km/sec) at the start of the period following CME passage that commenced early on 24 November. CME effects subsided during 25 November. There were no significant disturbances observed during the remainder of the period. The greater than 10 MeV event that began at 22/2320 UTC ended at 27/2100 UTC. The peak for this event was 18,900 pfu at 24/0555 UTC. There were no proton events during the rest of the period.

**03 - 09 December 2001** Solar wind velocities and proton temperatures were elevated during 03 – 07 December suggesting a weak high-speed stream associated with a negative-polarity coronal hole. Solar wind velocities occasionally exceeded 500 km/sec during this time. There were no significant disturbances during the remainder of the period. There were no proton events detected at geosynchronous orbit.

**10 - 16 December 2001** A relatively weak high-speed stream associated with a positive-polarity coronal hole was observed during the last two days of the period. Velocities and temperatures were elevated during this time with intermittent “gusts” in the 500 to 600 km/sec range. There were no significant disturbances observed during the rest of the period. There were no proton events detected at geo-synchronous orbit.

**17 December – 23 December 2001** A high-speed stream associated with a coronal hole was observed during 17 – 18 December with velocities as high as 570 km/sec and

elevated proton temperatures. These effects subsided late on 18 December. There was a period of increased velocities and temperatures during the latter half of 21 December. IMF Bz was southward most of 21 December, but was more strongly so during the latter half of the day with maximum deflections to minus 12 nT (GSM). There were no significant disturbances noted during the rest of the period. There were no proton events detected at geo-synchronous orbit. Note: greater than 100 MeV and greater than 10 MeV proton events began on 26 December following a major flare from Region 9742. Details will be provided in next week's report.

**24 - 30 December 2001** However, ACE SWEPAM data was unreliable during approximately 26/0630 – 1400 UTC due to solar proton contamination. A high-speed stream was observed during 24 – 25 December, associated with a negative-polarity coronal hole. Solar wind velocities increased to as high as 600 km/sec during this time. A coronal mass ejection passed the spacecraft at approximately 29/0440 UTC accompanied by abrupt increases in total IMF field intensity, temperature, density, and velocity; and (initially) a fairly strong northward turn of IMF Bz with peak deflections to plus 15 nT (GSM). The source for this CME passage may have been the long-duration M7/1b flare on 26 December. Another CME passage began at approximately 30/1932 UTC accompanied by increased proton temperatures and densities, as well as increased IMF total field intensity. IMF Bz became highly variable following the passage with a range of plus 26 to minus 20 nT (GSM). Three proton events occurred at geosynchronous orbit during the period. Proton events at greater than 100 MeV and 10 MeV occurred in the wake of the M7/1b flare on 26 December. The greater than 100 MeV event began at 26/0555 UTC, reached a peak of 50 PFU at 26/0720 UTC, then ended at 26/1940 UTC. The greater than 10 MeV event began at 26/0605 UTC, reached a peak of 779 PFU at 26/1115 UTC, then ended at 28/1040 UTC. Another greater than 10 MeV proton event began at 29/0510 UTC, reached a peak of 76 PFU at 29/0815 UTC, then ended at 29/2205 UTC. This event may have been due to the east limb X3 flare on 28 December. Another greater than 10 MeV proton event began at 30/0240 UTC and was in progress as the period ended (the preliminary peak for this event was 108 PFU at 31/1620 UTC).

**31 December 2001 - 06 January 2002** A coronal mass ejection (CME) passage was in progress at the start of the period with wind velocities as high as 670 km/sec early on 31 December. However, CME effects subsided by late on 31 December as velocities gradually decreased. There were no significant disturbances observed during the rest of the period. A greater than 10 MeV proton event was in progress at the start of the period. It began at 30/0240 UTC, reached a peak of 108 PFU at 31/1620 UTC, and ended at 04/2355 UTC following a very gradual decay.

**07 - 13 January 2002** A high-speed stream associated with a coronal hole was observed during 10 – 13 January. Solar wind velocities peaked early on 11 January with “gusts” as high as 700 km/sec, then gradually decreased. There were no significant disturbances observed during the rest of the period. A greater than 10 MeV proton event began at 10/2045 UTC, reached a maximum of 91 PFU at 11/0530 UTC, and ended at 13/1425 UTC. The prominence eruption of 09 January may have been the source for this proton event. Note: a greater than 10 MeV proton event began on the day of this report. Details will be provided in next week's issue.

**14 - 20 January 2002** No significant disturbances were observed during 14 – 18 January. A high-speed stream associated with a coronal hole commenced on 19 January and was in progress as the period came to a close. Solar wind velocities increased to as high as 570 km/sec during the course of this stream (which subsided on 21 January). A greater than 10 MeV proton event occurred during 15 – 16 January. It began at 15/1435 UTC, reached a maximum of 15 PFU at 15/2000 UTC, and ended at 16/1205 UTC. The source for this event may have been the long-duration M4 X-ray flare on 14 January.

**21 - 27 January 2002** Solar wind velocities were elevated during 21 January, possibly due to a high-speed stream associated with a coronal hole. Velocities peaked at around 550 km/sec during this period. There were no significant disturbances observed during the rest of the period. There were no proton events detected at geosynchronous orbit. However, a greater than 10 MeV proton flux enhancement (peak flux 9.0 PFU) occurred during the latter half of 27 January following an event from beyond the northwest limb of the Sun.

**28 January - 03 February 2002** A weak CME shock front passed the spacecraft late on 31 January associated with relatively minor increases in solar wind velocity, temperature, density, and interplanetary field intensity. This passage may have been associated with a partial-halo CME observed near the west limb on 27 January. A second CME passage occurred on 02 February associated with modest increases in velocity and temperature as well as a sustained period of southward IMF B<sub>z</sub> with maximum deflections to minus 13 nT. This passage may have been associated with the filament disappearance mentioned above. There were no disturbances during the rest of the period. There were no proton events at geosynchronous orbit during the period.

**04 - 10 February 2002** A high-speed solar wind stream associated with a coronal hole occurred during 05 – 08 February with “gusts” as high as 750 km/sec detected on 06 February. Another high-speed coronal hole wind stream commenced early on 10 February and was in progress as the period ended. Solar wind velocities increased from 400 km/sec to around 620 km/sec during this time. There were no proton events at geosynchronous orbit during the period.

## Appendix F: Electron Event Comparison to Solar Wind Data

This section presents Electron Events #1, #4, #5, #22, and #24 with corresponding solar wind data plots taken from the ACE website. The purpose of this is to show when the GEO and LEO electron event onsets occur in relation to solar wind characteristics. The solar wind plots can be credited to J.D. McComas, Southwestern Research Institute.

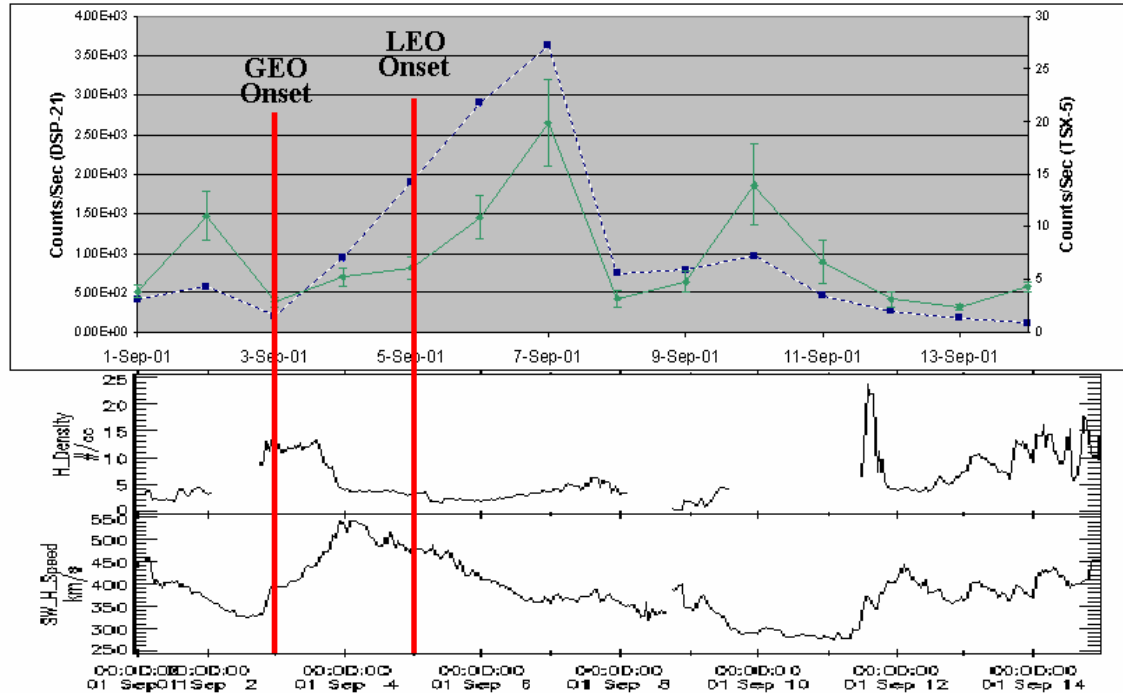


**Figure F1. Event #1 with solar wind data. The GEO onset appears to occur during the solar wind speed increase suggesting the GEO onset occurs during the leading edge of a high speed stream. The LEO onset occurs during the solar wind speed decrease; this suggests the LEO onset occurs during the trailing edge of the high speed solar wind stream.**

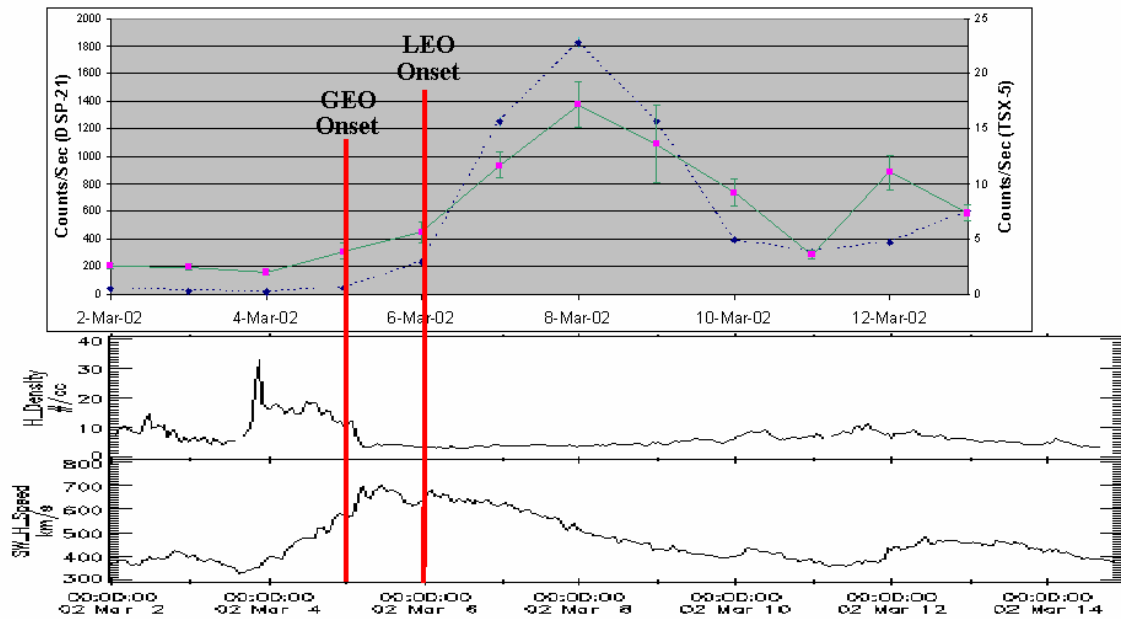


**Figure F2.** Event #4 with solar wind data. The GEO onset appears to occur during the solar wind speed increase suggesting the GEO onset occurs during the leading edge of a high speed stream. The LEO onset occurs during the solar wind speed decrease; this suggests the LEO onset occurs during the trailing edge of the high speed solar wind stream.

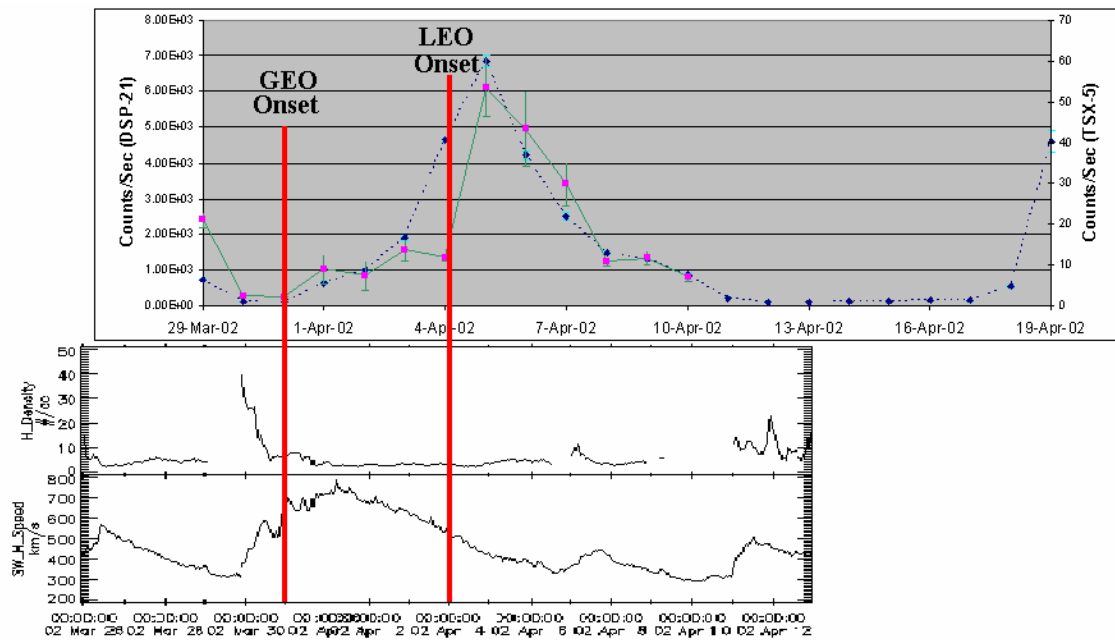


**Figure F3. Event #5 with solar wind data. The GEO onset appears to occur during the solar wind speed increase suggesting the GEO onset occurs during the leading edge of a high speed stream. The LEO onset occurs during the solar wind speed decrease; this suggests the LEO onset occurs during the trailing edge of the high speed solar wind stream.**

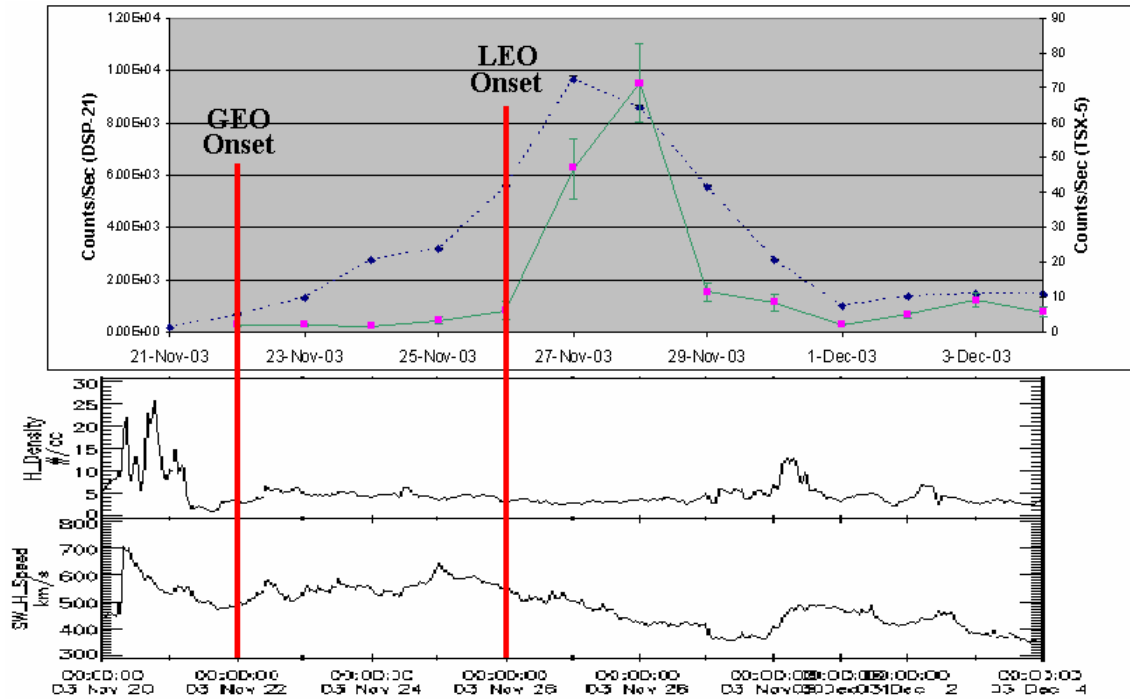


**Figure F4.** Event #22 with solar wind data. Although the speed increase is not as evident as other high speed streams, the GEO onset occurs after the particle density spike. It is still possible for this event to be the result of a high speed stream. The LEO onset occurs during a more pronounced solar speed decrease; this suggests the LEO onset occurs during the trailing edge of the high speed solar wind stream.

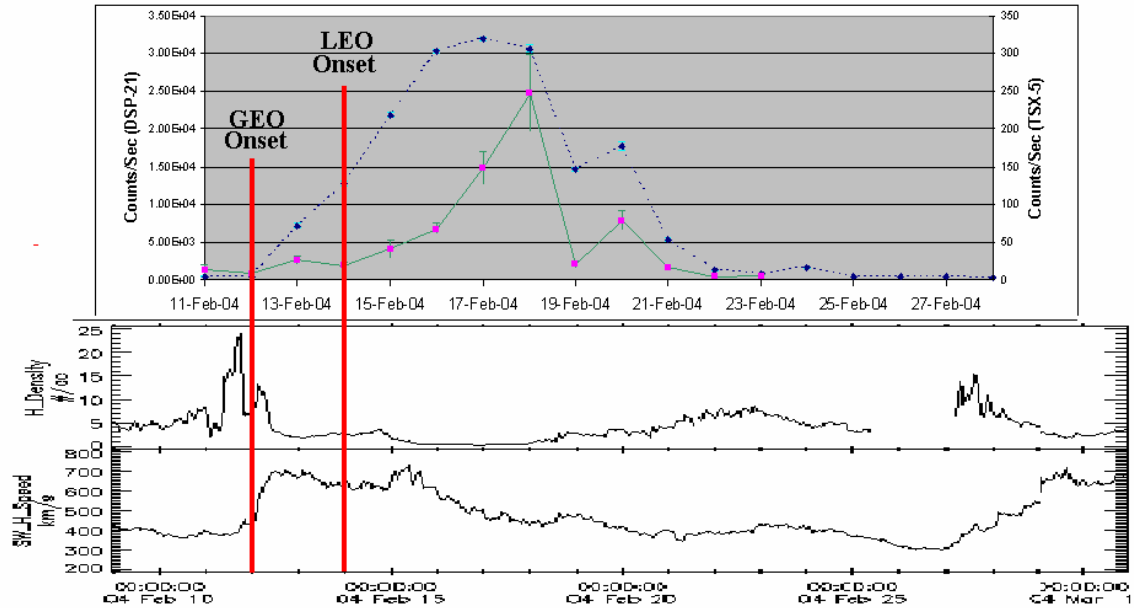


**Figure F5. Event #24 with solar wind data.** The GEO onset appears to occur during the solar wind speed increase suggesting the GEO onset occurs during the leading edge of a high speed stream. Although a second increase in solar wind speed happens on 15 Feb 04, the LEO onset appears to occur during a solar wind speed decrease. This suggests the LEO onset occurs during the trailing edge of the high speed solar wind stream.

## Bibliography

Amherst Astronomy Association (AAA). Picture altered from website. Dec 2004.  
<http://www.amastro.org>.

Brautigam, D. H and others. “Solar Cycle Variation of Outer Belt Electron Dose at Low Earth Orbit.” *IEEE Transactions of Nuclear Science*. Dec 01: 2010-2015.

Cairns, Iver. “Co-rotating Interaction Regions: Interactions between Fast and Slow Streams.” University of Sydney, Australia. Picture taken from lecture. 1 Sep 1999. <http://www.physics.usyd.edu.au/~cairns/teaching/lecture11/>.

Cosmic and Heliospheric Learning Center (CHLC). The National Aeronautics and Space Administration (NASA). “The Earth’s Magnetosphere.” Picture in article. 8 Dec 2004. <http://helios.gsfc.nasa.gov/magnet.html>

Dichter, B. K and others. “Compact Environmental Anomaly Sensor (CEASE): A Novel Spacecraft Instrument for *In Situ* Measurements of Environmental Conditions.” *IEEE Transactions of Nuclear Science*. Dec 98: 2758-2764.

Fitzpatrick, Richard. “Introduction to Plasma Physics.” Excerpt from a lecture. No page. 1998. <http://farside.ph.utexas.edu/teaching/plasma//lectures>.

Green, James L. “The Magnetosphere.” Excerpts from a lecture. No page. 19 Apr 04. <http://ssdoo.gsfc.nasa.gov/education/lectures/magnetosphere/index.html>

Heber, B. and others. “Corotating Interaction Regions.” *Advance Space Research*. Vol. 23, No. 3. 1999: 567-579.

Hultqvist, Bengt and others. *Magnetosphere Plasma Sources and Losses*. Boston: Kluwer Academic, 1999.

Li, Xinlin and Michael A. Temerin. "The Electron Radiation Belt." Kluwer Academic Publishers. Netherlands: 2000. <http://lasp.colorado.edu/~lix/papers.html>.

Mazur, J. E. "An Overview of the Space Radiation Environment." Crosslink. 2003. <http://www.aero.org/publications/crosslink/summer2003/02.html>.

Miyoshi, Y.S. and others. "Solar Cycle Variation of the Electron Radiation Belts: Observations and Radial Diffusion Simulation." *Space Weather*. Vol 2, S10202, 2004.

McComas, D.J. Southwestern Research Institute. ACE data plots from the CDS website. [http://cdaweb.gsfc.nasa.gov/cdaweb/sp\\_phys](http://cdaweb.gsfc.nasa.gov/cdaweb/sp_phys).

National Oceanic and Atmospheric Administration (NOAA). "Today's Space Weather." *Space Environment Center*. Nov 2004. <http://www.sec.noaa.gov/today.html>.

National Oceanic and Atmospheric Administration (NOAA). "Solar Cycle Progression." *Space Environment Center*. Plots taken from website. Dec 2004. [www.sec.noaa.gov/SolarCycle](http://www.sec.noaa.gov/SolarCycle)

NOAASIS. "NOAA's Geostationary and Polar-Orbiting Weather Satellites." 21 Nov 2003. <http://noaasis.noaa.gov/NOAASIS/ml/genlsatl.html>.

Onsager, T.G. and others. "The Radial Gradient of Relativistic Electrons at Geosynchronous Orbit." *Journal of Geophysical Research*. Vol 109, A05221, 2004.

Parks, George K. *Physics of Space Plasma*. Massachusetts: Perseus Books, 2004.

Smithro, Christopher G. Excerpts taken from Physics 519 lecture. 2003.

Space and Missile Systems Center. "Fact Sheet, United Stated Air Force: Defense Support Program" May 2000.

[www.losangeles.af.mil/SMPA/PA/Fact\\_Sheets/dsp\\_fs.htm](http://www.losangeles.af.mil/SMPA/PA/Fact_Sheets/dsp_fs.htm)

Tascione, Thomas F. *Introduction to the Space Environment*. Florida: Krieger Publishing, 1994.

Taylor, John R. *An Introduction to Error Analysis: The Study of Uncertainties in Physical Measurements*. Second Edition. Sausalito, CA: University Science Books, 1997.

Williams, D. J. and others. "Observations of Trapped Electrons at Low and High Altitudes." *Journal of Geophysical Research, Space Physics*. 1 Sep 69: 5673-5696.

<b>REPORT DOCUMENTATION PAGE</b>				<i>Form Approved OMB No. 074-0188</i>
<p>The public reporting burden for this collection of information is estimated to average 1 hour per response, including the time for reviewing instructions, searching existing data sources, gathering and maintaining the data needed, and completing and reviewing the collection of information. Send comments regarding this burden estimate or any other aspect of the collection of information, including suggestions for reducing this burden to Department of Defense, Washington Headquarters Services, Directorate for Information Operations and Reports (0704-0188), 1215 Jefferson Davis Highway, Suite 1204, Arlington, VA 22202-4302. Respondents should be aware that notwithstanding any other provision of law, no person shall be subject to an penalty for failing to comply with a collection of information if it does not display a currently valid OMB control number.</p> <p><b>PLEASE DO NOT RETURN YOUR FORM TO THE ABOVE ADDRESS.</b></p>				
<b>1. REPORT DATE (DD-MM-YYYY)</b> 03-05-2005	<b>2. REPORT TYPE</b> Master's Thesis	<b>3. DATES COVERED (From – To)</b> Sep 2003 – Mar 2005		
<b>4. TITLE AND SUBTITLE</b>  Timing of Increasing Electron Counts from Geosynchronous Orbit to Low Earth Orbit			<b>5a. CONTRACT NUMBER</b>	<b>5b. GRANT NUMBER</b>
			<b>5c. PROGRAM ELEMENT NUMBER</b>	
<b>6. AUTHOR(S)</b>  Olson, Kirk, M., Captain, USAF			<b>5d. PROJECT NUMBER</b>	<b>5e. TASK NUMBER</b>
			<b>5f. WORK UNIT NUMBER</b>	
<b>7. PERFORMING ORGANIZATION NAMES(S) AND ADDRESS(S)</b>  Air Force Institute of Technology Graduate School of Engineering and Management (AFIT/EN) 2950 Hobson Way WPAFB OH 45433-7765			<b>8. PERFORMING ORGANIZATION REPORT NUMBER</b>  AFIT/GAP/ENP/05-06	
<b>9. SPONSORING/MONITORING AGENCY NAME(S) AND ADDRESS(ES)</b>  Attn: Dr. Donald Brautigam AFRL/VSBXR 29 Randolph Rd Hanscom AFB, MA 01731 Phone: (781) 377-3890			<b>10. SPONSOR/MONITOR'S ACRONYM(S)</b>	<b>11. SPONSOR/MONITOR'S REPORT NUMBER(S)</b>
<b>12. DISTRIBUTION/AVAILABILITY STATEMENT</b> APPROVED FOR PUBLIC RELEASE; DISTRIBUTION UNLIMITED.				
<b>13. SUPPLEMENTARY NOTES</b>				
<b>14. ABSTRACT</b>  Under certain conditions, high energy electron fluxes can increase over short periods of time in the outer radiation belt and diffuse to low altitudes. Sudden increases of high energy electron densities at low altitudes can drastically damage unsuspecting low-earth-orbit satellites. The progression of electron flux increases from a geosynchronous orbit to low-earth orbit during an electron event is somewhat unknown. If the beginning of electron flux increases at low-earth-orbits could be anticipated, warnings could be issued to space system operators allowing time to take proper measures to protect and minimize satellite damage extending satellite lifetimes and space mission operations.  The Compact Environment Anomaly Sensors (CEASE) onboard the DSP-21 and TSX-5 satellites collected dosimeter data of electrons > 1.2 MeV and protons > 25 MeV. The orbits of the satellites and the particle detection of CEASE provided an opportunity to sample the high energy electron population fluxes at GEO and LEO during electron events. The high energy electron CEASE data was extracted from DSP-21 and TSX-5 when each satellite crossed an approximate geosynchronous L-Shell range (L=6.5-6.7). Onsets of electron events at each orbit were determined from the data. Onset comparison showed the progression of elevated electron fluxes from GEO to LEO to be between one and four days. Further comparison of the electron events to solar wind data suggests that high speed streams are necessary, not sufficient, for an electron event to occur.				
<b>15. SUBJECT TERMS</b> Electron Belt, Van Allen Belt, Event, Magnetosphere, TSX-5, DSP-21, Geosynchronous, Low-earth Orbit, Outer Radiation Belt, Progression, Electron Flux, L-Shell, High Speed, Solar Wind, Magnetic Field Lines.				
<b>16. SECURITY CLASSIFICATION OF:</b> REPORT U		<b>17. LIMITATION OF ABSTRACT</b> UU	<b>18. NUMBER OF PAGES</b> 98	<b>19a. NAME OF RESPONSIBLE PERSON</b> Devin Della-Rose, Major, USAF (ENP)  <b>19b. TELEPHONE NUMBER (Include area code)</b> (937) 255-3636, ext 4514; e-mail: Devin.Della-Rose@afit.edu